ISSN: 2224-2007
E-ISSN: 2707-7365

MIJST

MIST International Journal of Science and Technology

A Peer Reviewed Online Open Access Journal

Victory Day Issue

Volume 08
December 2020

Military Institute of Science and Technology (MIST)
https://mijst.mist.ac.bd/mijst
Previously known as:
MIST Journal of Science and Technology

MIJST

MIST International Journal of Science and Technology

EDITORIAL BOARD

PROOF/LANGUAGE SUPPORT GROUP

Maj Md. Manwarul Haq, PhD, AEC
Associate Professor
Science & Humanities, Military Institute of Science and Technology
Dhaka, Bangladesh

Selin Yasmin
Associate Professor
Science & Humanities, Military Institute of Science and Technology
Dhaka, Bangladesh

Md Moslem Uddin
Librarian, Military Institute of Science and Technology
Dhaka, Bangladesh

RESEARCH COORDINATOR

Lt Col Muhammad Sanaullah, psc, Engrs
GSO-1, R&D Wing,
Military Institute of Science and Technology
Dhaka, Bangladesh

WEB CONSULTANT

Dr. M. Akhtaruzzaman
Assistant Professor, CSE,
Military Institute of Science and Technology
Dhaka, Bangladesh

EDITORIAL BOARD MEMBERS (EXTERNAL)

Dr. Md Hadiuzzaman
Professor,
Bangladesh University of Engineering & Technology (BUET),
Bangladesh

Dr. M. Kaykobad
Professor,
Bangladesh University of Engineering & Technology (BUET),
Bangladesh

Dr. A.B.M. Harun-ur Rashid
Professor,
Bangladesh University of Engineering & Technology (BUET),
Bangladesh

Dr. Abdul Hasib Chowdhury
Professor,
Bangladesh University of Engineering & Technology (BUET),
Bangladesh

Dr. Mohammad Ali
Professor,
Bangladesh University of Engineering & Technology (BUET),
Bangladesh

Dr. Nikhil Ranjan Dhar
Professor,
Bangladesh University of Engineering & Technology (BUET),
Bangladesh

Dr. Shahjada Tarafder
Professor,
Bangladesh University of Engineering & Technology (BUET),
Bangladesh

Dr. Tanvir Ahmed
Professor,
Bangladesh University of Engineering & Technology (BUET),
Bangladesh

Dr. Khandaker Shabbir Ahmed
Professor,
Bangladesh University of Engineering & Technology (BUET),
Bangladesh

Dr. Nahrizul Adib Bin Kadri
Assoc. Professor,
University of Malaya,
Malaysia

Dr. Sunil S. Chirayath
Assoc. Professor,
Texas A&M University,
USA

Dr. A.K.M. Masud
Professor,
Bangladesh University of Engineering & Technology (BUET),
Bangladesh

Dr. ASM Woobaidullah
Professor,
Dhaka University,
Bangladesh

Dr. Abdul Basith
Professor,
Bangladesh University of Engineering & Technology (BUET),
Bangladesh

Dr. Md Abdul Jabbar
Professor,
Dhaka University,
Bangladesh

DISCLAIMER

The analysis, opinions, and conclusions expressed or implied in this Journal are those of the authors and do not necessarily represent the views of the MIST, Bangladesh Armed Forces, or any other agencies of Bangladesh Government. Statements of fact or opinion appearing in MIJST Journal are solely those of the authors and do not imply endorsement by the editors or publisher.

ISSN: 2224-2007
E-ISSN: 2707-7365

QUERIES ON SUBMISSION

For any query on submission the author(s) should contact: MIST, Mirpur Cantonment, Dhaka-1216, Bangladesh; Tel: 88 02 8034194, FAX: 88 02 9011311, email: *mijst@mist.ac.bd*. For detailed information on submission of articles, the author(s) should refer to the Call for Papers and About MIJST at the back cover of the MIJST Journal. Authors must browse MIJST website through the journal link (*https://mijst.mist.ac.bd/mijst*) for electronic submission of their manuscripts.

PUBLISHER

Military Institute of Science and Technology (MIST), Dhaka, Bangladesh

DESIGN AND PRINTING

Research and Development Wing
Military Institute of Science and Technology (MIST)
Dhaka, Bangladesh

MESSAGE

CHIEF OF ARMY STAFF

بسم الله الرحمن الرحيم

ARMY HEADQUARTERS
DHAKA CANTONMENT

Military Institute of Science and Technology (MIST) has taken a praiseworthy effort towards transforming its previous Journal – 'MIST Journal of Science and Technology' into an international journal founded on an Open Journal platform. The objective of the new Journal is to add value to the field of science and engineering. I appreciate timely initiative in upgrading MIST's Flagship Journal to 'Online Peer Reviewed Open Access.' The contents of 'MIST International Journal of Science and Technology (MIJST)' aptly reflect MIST's reputation and quality.

I am pleased that the launching of the December 2020 Issue of MIJST has been synchronized with the Victory Day of Bangladesh. Henceforth, it shall be published as the 'Victory Day Issue' to pay tribute to all the Martyrs and the Freedom Fighters of the Liberation War of Bangladesh. On this occasion, I also express my solemn respect and homage to the Father of the Nation, Bangabandhu Sheikh Mujibur Rahman on his centennial birth anniversary.

I wish MIJST's success in its noble mission of achieving the reputation of an international journal through meaningful research and dissemination of outputs in the field of cutting-edge Science and Technology!

AZIZ AHMED
General
Chief of Army Staff
Bangladesh Army

FOREWORD

Bismillahir Rahmanir Rahim

The Military Institute of Science and Technology (MIST) being a dynamic academic institution with a vision of achieving excellence in teaching and cutting-edge research in the areas of science, engineering, and technology plays an active role in the dissemination of quality research outputs of the institution and those of the national and international community through its flagship journal - 'MIST International Journal of Science and Technology (MIJST)'.

The Journal team worked hard to be able to publish the December issue of MIJST on the Victory Day of Bangladesh which so special to us. We pay our solemn respect to the 30 million Bengalis who laid their precious lives to free our motherland from the occupation of the Pakistani Army. We also pay our homage and deep respect to our Father of the Nation, the Architect of Bangladesh - 'Bangabandhu Sheikh Mujibur Rahman' on His 100th Birth Anniversary.

I would like to take this opportunity to thank the MIJST team for their hard work and express my deep appreciation to the Authors of the issue, and the associated personnel for their tireless efforts and contributions to the December Issue 2020 of MIJST. Sincere appreciation to all the reviewers for providing invaluable peer review to the articles published in this issue to ensure high quality. Very special thanks to the National and the International Advisory Boards for their invaluable suggestions and guidance in maintaining the quality of the Journal.

I wish continued success of MIJST.

Major General Md Wahid-Uz-Zaman, ndc, aowc, psc, te
Commandant, MIST, Bangladesh
Chief Patron, MIJST, Bangladesh

EDITORIAL

Despite the difficulties posed by global COVID-19 pandemic; the second (December 2020) issue of MIST International Journal of Science and Technology (MIJST) has been published well within the schedule. I am pleased to note that this was possible thanks to the hard work and consolidated efforts undertaken by the authors, the reviewers, and the editorial & production teams whose commitment, synergy, love, and vision for the Journal are unwavering. The journal remains fully committed to publishing contemporary and innovative theoretical and applied research outputs in the fields of science, engineering, and technology, which makes MIJST a true interdisciplinary journal.

The MIJST is a bi-annual and Open Access Journal. The Open Access policy enables the journal to be accessed by all readers and makes it more visible and globally accessible facilitating diffusion of new knowledge and innovations. Furthermore, authors and readers do not need to incur any cost for the publication and getting access to the journal. Inclusion of the Journal in several Indexing Databases, such as, 'Google Scholar', 'DOI Crossref', 'Microsoft Academic Search', 'Semantic Scholar', 'Publons', 'Creative Common' and 'Open Journal System' has increased its visibility worldwide. The Journal Team has the roadmap for getting MIJST indexed under more renowned global citation databases including Directory of Open Access Journals (DOAJ), Emerging Source Citation Indexing (ESCI), SCOPUS and Web of Science (WoS). Our readers will be highly pleased to hear that the MIJST now has a Digital Object Identifier (DOI) registration for the journal and all the individual articles. This DOI provides an International standardization of scholarly articles along with the journal itself. It gives all readers/authors/researchers confidence in the citation of the paper as the paper has unique worldwide identification permanently.

Researchers, professionals, and industry practitioners are urged to submit their unpublished, original, and innovative contributions from any branch of science, engineering, technology, and related areas. As per the Journal's strict policy, all submitted contributions go through a double-blind peer-review process with effective feedback. We are committed to publishing high quality original, innovative, and latest findings as original articles and review articles (by invitation).

This December issue includes five original research articles covering materials structural strength, safety systems of nuclear reactors, corrosive behaviour of heat exchanger, road vehicle drifting, modelling, and controlling of a robotic chair-arm for non-contact COVID-19 application. These articles are innovative and have significant implication(s) in science, engineering, and technology fields. The research findings of each article deal with real-world problems.

I cordially invite distinguished experts from around the world to submit review articles summarising the latest development, state of knowledge and applications in contemporary science, engineering, and technology fields with special emphasis on economic viability, safety, efficiency, and environmental sustainability.

Finally and above all, I express my sincere appreciation and gratitude to the Chief Patron, Executive Editor, Associate Editors, Section Editors, Reviewers, other Editors and Proof Readers, Editorial/Advisory Board members (national and international), and web production consultant for their hard work, unwavering support, commitment, and enthusiasm especially during COVID-19 pandemic time. Without their hard work and commitment, the publication could not be materialized on time. I am

taking this opportunity to request all authors, reviewers, readers, and patrons for the promotion of the MIST International Journal of Science and Technology (MIJST) to their colleagues and library databases in their organizations and across the globe.

As always, I warmly welcome your feedback, suggestion, and advice for the advancement of the MIST International Journal of Science and Technology (MIJST). You are highly encouraged to contact me at firoz.alam@rmit.edu.au or mijst@mist.ac.bd with any suggestions, queries, or ideas.

Sincerely,

Prof. Dr. Firoz Alam
Editor in Chief

INDEX

MIJST
MIST International Journal of Science and Technology

Tensile Strength Study of Stainless-Steel using Weibull Distribution

Md Shahnewaz Bhuiyan[1*], Tanzida Anzum[2], Forhad-Ul-Hasan[3] and M. Azizur Rahman[4]

[1] Department of MPE, Ahsanullah University of Science and Technology, Dhaka, Bangladesh
[2] Cumilla Cantonment, Cumilla, Bangladesh
[3] Bogra Cantonment, Bogra, Bangladesh
[4] Department of MPE, Ahsanullah University of Science and Technology, Dhaka, Bangladesh

emails: *[*1] newaz.mpe@aust.edu; [2] tanzidaanzum@gmail.com, [3] forhad15eb@gmail.com; and [4] azizur777@gmail.com*

ARTICLE INFO

Article History:

Received: 03rd June 2020
Revsed: 11th August 2020
Accepted: 18th August 2020
Published: 16th December 2020

Keywords:

Weibull Distribution
Tensile Strength
Stainless Steel
Reliability

ABSTRACT

In the present study, the distribution pattern of the ultimate tensile strength of 304-grade stainless steel was investigated using a two-parameter Weibull distribution function. During tensile testing, it was observed that the ultimate tensile strength varied from specimen to specimen (ranges from 878 to 1006 MPa). The results have revealed that the distribution pattern of the tensile strength can be described by the two-parameter Weibull distribution equation. Moreover, the fracture statistics of the stainless steel were examined by plotting the survival probability of the specimen against the applied stress to the specimen. It has been observed that the relationship between the survival probability and the applied stresses can be described by the Weibull model. It also provides design engineers with a tool that will help them to present the necessary mechanical properties with confidence.

1. INTRODUCTION

Bangladesh enjoyed GDP growth of 8.1% in 2019 and is set to continue at a fast pace in the near future (United Nations, 2020). The dramatic rise in GDP has resulted in the rapid development of infrastructures and the construction industry has seen stellar growth with a rate of 16.25% (Islam *et al.*, 2016). It has been reported that Bangladesh will need to construct approximately 4 million new houses annually over the next twenty years to meet the future demand for housing (Bony & Rahman, 2014). It is noteworthy that most of the construction practice in Bangladesh is concentrated on reinforced concrete (RCC), which affects the environment directly such as global warming, the depletion of natural resources, waste generation and pollution etc. According to the Department of Environment (DoE) and the World Bank, traditional brick-making industries account for 56% of air pollution in Dhaka city (Islam, 2015). Hence to reduce air pollution, the Bangladesh government has decided to phase out conventional bricks by 2025 from all construction works (Rahman, 2019). From this point of view, sustainability construction concepts get more importance nowadays, where stainless steel is used as a building material due to durable, recyclable, and reusable characteristics (Aksel & Eren, 2015). In this context, the demand for steel in load-bearing structural applications has been gradually increasing in Bangladesh, mainly owing to their favourable properties such as high strength, better strength to weight ratio, attractive appearance, high fire and corrosion resistance, ability to retain its strength even at high temperatures, fabricability, weldability and so on (Monrrabal *et al.*, 2019; Wang *et al.*, 2019; Monteiro *et al.*, 2017; Feng *et al.*, 2019; Khatak *et al.*, 1996). In recent times, the steel is found to use for a range of structural applications in Bangladesh including:

1. Cladding and roofing applications in the transport sector for a load-bearing member, for example for bus frames (Chakma, 2019).
2. Prefabricated steel structures for different purposes such as setting up factories, multi-storied buildings, power plants and bridges, readymade garment factories, textile mills, pharmaceuticals industry (Nur, 2016).
3. Concrete filled stainless steel tube (CFSST) where a rectangular or circular cross-section steel tube is filled with concrete used in various constructions (Sanaullah *et al.*, 2019).

Therefore, mechanical properties such as strength is very important for the structural and architectural application of steel. Generally, conventional macro tensile tests are commonly used to evaluate mechanical properties such as yield strength, ultimate tensile strength, and ductility. To allow for effective comparison on macroscopic tensile test results, specific details (such as (i) shapes and sizes of the specimen, (ii) straining rates, (iii) methods of measurements, and (iv) data analysis, etc.) of the standard tensile test have been formulated. ASTM-E8/E8M (ASTM E8/E8M-16ae1, 2013) provides full descriptions of testing methods. Based on the macroscopic viewpoint, the mechanical properties of metallic materials are considered homogeneous. However, in the real material, a considerable amount of scattering is observed. The scatter in mechanical properties results from various uncertainties of different origins: (i) the variations in physical or chemical features during manufacturing processes (Azeez *et al.*, 2019), (ii) microstructure stochasticity due to thermo-mechanical processing (such as rolling and extrusion) and heat treatments (Birbilis *et al.*, 2006; Király *et al.*, 2018), (iii) machining and preparation method of the specimen resulting in the variation of residual stresses (SungHo *et al.*, 2010), (iv) variation of bulk defects (Azeez *et al.*, 2019). As a result, the mechanical properties vary from specimen to specimen, even though nominally identical specimens were tested under the same loading conditions (such as loading mode, speed). This indicates that the tensile testing data are not deterministic rather statistical. Hence, the inherent scatter behaviour of tensile properties needs to be assessed probabilistically.

In recent years, the Weibull distribution function has been extensively used for assessing the mechanical properties (both static and dynamic) of metallic materials (Hallinan *et al.*, 1993; Bedi *et al.*, 2009). One of the main reasons is that the probability density function of the Weibull distribution has a wide variety of shapes. For example, when the shape parameter is equal to 1, it becomes the two-parameter exponential function, whereas when the shape parameter is equal to 3, the function can approximate a normal distribution. Thus, the Weibull distribution has been proven to be useful to describe the statistical behaviour of tensile strength of many materials, such as ceramic (Glaeser *et al.*, 1997), metal matrix composites (Fukui *et al.*, 1997), fatigue properties of metallic materials (Evans *et al.*, 1983; Mohd *et al.*, 2015; Wang *et al.*, 2001; Bhuiyan *et al.* 2016). In the context of engineering design and reliability of structures, a good understanding of the scattering behaviour of the ultimate tensile strength of stainless steel may shed light on their safe utilization in design and manufacturing. Therefore, in the present study, the variation of the tensile strength of 304 stainless steel has been analysed using the Weibull distribution function. Finally, the reliability of the material in terms of ultimate tensile strength was presented in graphical form.

2. Experimental Procedure

A. Material and Specimen Preparation

The material used in the present study was a 304 Grade stainless steel plate (with composition (mas%) 0.0243~0.0268C, 0.334~0.352Si, 7.86~7.90Ni, 1.41~1.42Mn, 0.0242~0.0252P, 0.0056-0.0057S, 18.23~18.25Cr, 0.154~0.152Mo, 0.0804~0.0821Co, 0.144~0.145Cu, 0.0035~0.0036Ti, 0.0973~0.0976V) from STEELTECH company and was kindly supplied by the Civil Engineering Department of the Military Institute of Science and Technology (MIST).

From the supplied rectangular 304 stainless steel pipe, tensile test specimens with dimensions 136 mm (total length, L), 6 mm (gauge width, W), and 2 mm (thickness, T) were machined using a CNC milling machine, following the ASTM-E8 standard (ASTM E8/E8M-16ae1, 2013). The specimen geometry is shown in Figure 1.

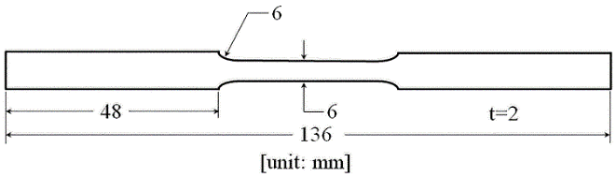

Figure 1: Geometries of mechanical test specimens

B. Tensile Testing Procedure

In total 10 specimens were prepared for tensile testing. Prior to tensile testing, the width and thickness of each specimen were measured at three locations in the gauge section, and an average cross-section area is calculated. Each specimen was then broken in a universal tensile testing machine with a crosshead speed of 1 mm/min.

For metallographic examination, samples were polished with 280 to 1500 grit emery papers in laboratory air. In the final polishing step, a 3-micron diamond paste was used. The freshly polished specimen was then etched using a solution containing 20 mL nitric acid and 60 mL hydrochloric acid following ASTM 407-07 (ASTM standard 407-07, 2005). The specimens were then observed under an optical microscope.

C. Theoretical Background

Based on the weakest-link hypothesis, Weibull proposed a simple distribution function for strength, σ. Its two-parameter form takes the form (Weibull, 1951):

$$F(\sigma_i;\sigma_0,m) = 1 - exp\left[\left(-\frac{\sigma_i}{\sigma_0}\right)^m\right] \sigma_0 > 0, m > 0 \qquad (1)$$

where $F(\sigma_i;\sigma_0,m)$ is the probability of failure, σ_0 is the characteristic tensile strength (alternatively referred to as scale parameter) where 63.2% of samples fail (36.8% survival probability for samples stressed at loading equal to σ_0), σ_i is the variable (ultimate tensile strength in the present study), and m is the slope of the curve known as shape parameter (alternatively referred to as Weibull modulus) and is a measure of data scattering and the scale parameter σ_0.

The Weibull modulus, m, is estimated using one of the three methods: (i) linear regression, (ii) maximum likelihood, and (iii) moments. However, the commonly used method is linear regression because of its simplicity and relative ease in use (Tiryakioğlu, Hudak, & Ökten, 2009).

By taking the natural logarithm of both sides of Equation (1) twice yields:

$$ln\left[ln\left(\frac{1}{1-F(\sigma_i;\sigma_o,m)}\right)\right] = mln(\sigma_i) - mln(\sigma_o) = mx + c \quad (2)$$

In Weibull statistics, the following four probability estimators are commonly used (Bergman, 1984; Datsiou *et al.*, 2018):

$$F(\sigma_i;\sigma_0,m) = \frac{i}{n+1} \quad (3a)$$

$$F(\sigma_i;\sigma_0,m) = \frac{i-0.5}{n} \quad (3b)$$

$$F(\sigma_i;\sigma_0,m) = \frac{i-0.3}{n+0.4} \quad (3c)$$

$$F(\sigma_i;\sigma_0,m) = \frac{i-0.375}{n+0.25} \quad (3d)$$

where i is the index of the ascending, n is the sample size (10 in the present study).

Bergman (1984) reported that probability estimators given by Equation (3d) should be used for a small sample size ($n < 20$). Therefore, in the present study, probability estimators defined by Equation (3d) is used to assign a probability of failure to each ultimate tensile strength data point.

The Weibull modulus, m, and the characteristic tensile strength, σ_0, can be obtained by plotting $ln\left[ln\left(\frac{1}{1-F(\sigma_i;\sigma_o,m)}\right)\right]$ against $ln(\sigma_i)$. After taking a linear regression of the data point, the slope of the regressed line is the Weibull modulus, m, and the intercept is $mln(\sigma_o)$.

By fitting a straight line or applying the least square method to $ln\left[ln\left(\frac{1}{1-F(\sigma_i;\sigma_o,m)}\right)\right]$ as a function of $ln(\sigma_i)$, the Weibull modulus m is the slope and the scaling parameter or characteristic tensile strength can be determined from the intercept.

3. RESULTS AND DISCUSSION

A. General Mechanical Properties

Figure 2 shows the optical microstructure for the material used in this study. A typical step structure is observed. C. A. Della-Rovere *et al.* (2013) and A Bahrami *et. al.* (2019) also reported similar microstructures of 304-grade stainless steel. As reported earlier that in total ten tensile tests were performed and corresponding ten stress-strain curves were recorded for each material. A typical stress-strain curve is shown in Figure 3. It is found that the tensile strength ranges from 878 MPa to 1006 MPa, inferring that the ultimate tensile strength appears to vary from specimen to specimen. Table 1 and Table 2 lists the basic statistical properties of ultimate tensile strength and yield strength of the material used in this study. Note that the coefficient of variation (COV = Standard Deviation (σ)/Mean (μ)×100) is about 4.3% for ultimate tensile strength, and 7.6% for yield strength. Kweon *et al.* (2020) reported that the ultimate tensile strength of 304 stainless steel is in the range of 579 to 750 MPa. But our investigated material showed about 1.75-1.90 times higher value of ultimate tensile strength that was reported by Kweon *et al.* (2020). The observed difference might have resulted due to random experimental errors such as variation in width and thickness in the gauge section, machining of specimen resulting in the variation of residual stresses, microstructural heterogeneity in the gauge section. Since the specimens were prepared using a CNC milling machine, hence all the specimens used in this study were identical in shape and size. Therefore, it is reasonable to assume that the variation of width and thickness in the specimen's gauge section does not influence the observed high value of ultimate tensile. It is well established that during machining because of tool-material interactions, the generated surface is affected through roughness, hardness, residual stress distribution and thereby, influence the mechanical properties of the manufactured parts (Kumar *et al.*, 2017; Ben Fredj *et al.*, 2006; Gürbüz *et al.*, 2017; Ma *et al.*, 2018). H. Sutanto (2007) investigated the characteristics of residual stresses during CNC milling machining and observed that very high compressive residual stress (-375 MPa) was induced at the surface of the work material. H. H. Zeng *et al.* (2017) investigated the residual stresses in micro-end milling considering sequential cuts effect and found compressive residual stresses were induced by milling operations. Therefore, based on the above discussion, it is speculated that compressive residual stresses were also induced during the CNC milling machining. However, the surface residual stress is not measured in the present study. Hence, it can be inferred that both microstructural heterogeneity and the milling machining induced high compressive residual stresses resulted in higher ultimate tensile strength (about 1.75-1.90 times) in the studied material. Furthermore, for precise and accurate characterization of tensile properties, it is instructive to use a more advanced technique such as electro-discharge machining (EDM) for specimen preparation.

Table 1
Statistical Properties of the Ultimate Tensile Strength

Mean value (MPa)	Standard deviation (MPa)	Coefficient of variation (CV)
941	40.4	4.3%

Table 2
Statistical Properties of The Yield Strength

Mean value (MPa)	Standard deviation (MPa)	Coefficient of variation (CV)
577	44	7.6%

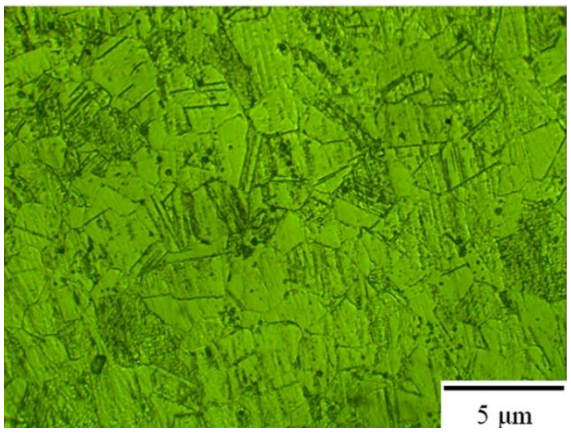

Figure 2: Optical microstructure of 304 stainless steel

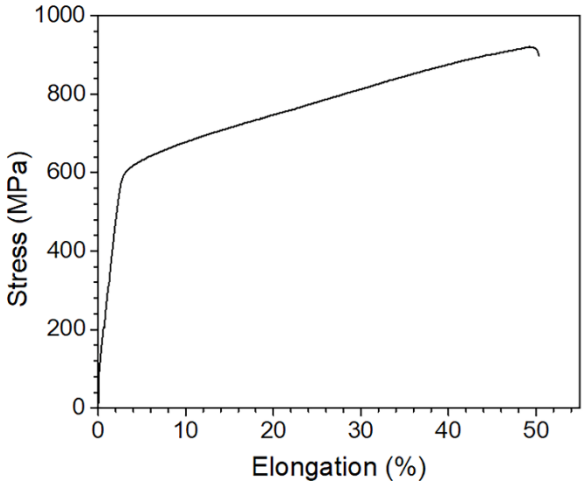

Figure 3: Typical stress-strain curves obtained in the room temperature tensile test

B. Statistical Analysis of Tensile Data

Figure 4 shows the two-parameter Weibull plot of ultimate tensile strength data. The linear regression model with the regression line is also shown in Figure 4. It can be noted that a good linear relationship was observed which suggested that the distribution pattern of the ultimate tensile strength can be reasonably approximated by the Weibull distribution equation.

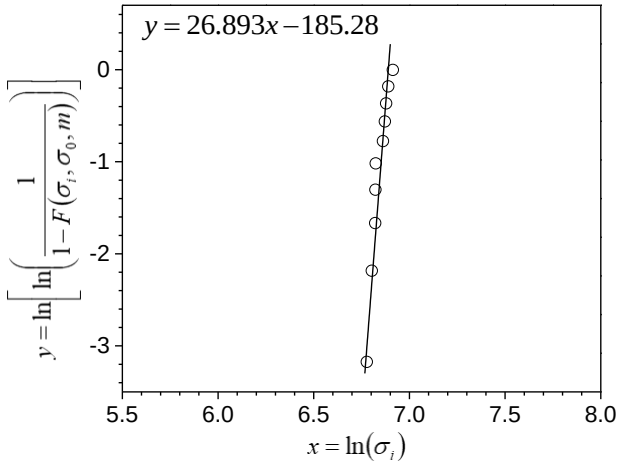

Figure 4: Two-parameter Weibull plot for ultimate tensile strength data

The obtained Weibull distribution parameters such as the Weibull modulus, m, the characteristics tensile strength, σ_o, are listed in Table 2. The slope of the line is 26.893, which is the value of the Weibull modulus. Generally, the shape parameter (or Weibull modulus), $m < 1.0$ indicates that the material has a decreasing failure rate, $m = 0$ indicates a constant failure rate, and $m > 1.0$ indicates an increasing failure rate. Our obtained value m =26.893 clearly indicates that the material tends to fracture with a higher probability for every unit increase in applied tensile load. As mentioned earlier that the parameter σ_0 is the characteristics tensile strength and as a theoretical property $F(\sigma_i; \sigma_0, m) = 0.368$. Based on Table 2, the value of σ_0 is about 982. Therefore, using the value of $\sigma_i = \sigma_o = 982$ and $m = 26.893$, $R(\sigma_i; \sigma_0, m) = R(982; 982, 26.893 = exp\left[\left(-\frac{\sigma_i}{\sigma_0}\right)^m\right] =$ 0.368, indicating that 36.8% of the tensile tested specimens have a fracture strength of at least 982 MPa.

Table 2
Parameters of two-parameter Weibull distribution

Parameter	Symbol	Values
Shape parameter	m	26.893
Constant term	c	185.28
Scale parameter	$\sigma_0 = e^{\frac{c}{\beta}}$	982

The Weibull reliability distribution curve for tensile strength is shown in Figure 5. It is observed that the tensile strength values of less than 750 MPa are highly reliable. For a more certain assessment, let us consider 0.95 and 0.9 reliability levels. Using these values in Equation (2), the equation is solved for σ_i and the fracture strength values obtained were 879 MPa and 903 MPa, respectively. More specifically, the material will fracture with 0.90 probability for tensile stress of 903 MPa and similarly will fracture with 0.95 probability for tensile stress of 879 MPa.

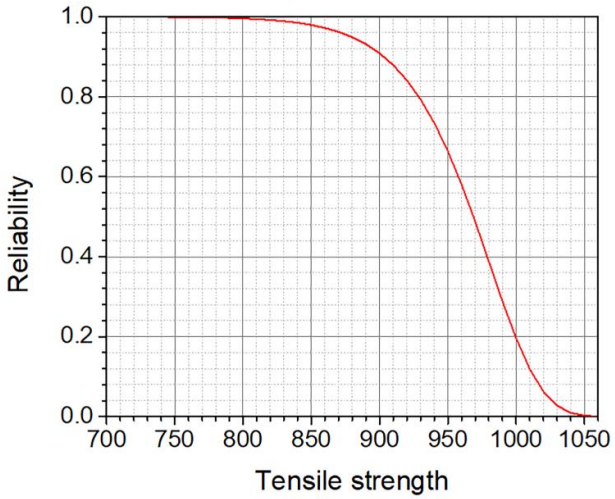

Figure 5: Weibull reliability distribution for tensile strength

4. CONCLUSIONS

In the present study, the distribution pattern of the ultimate tensile strength of 304-grade stainless steel was investigated. The main conclusions obtained are summarized as follows:

1. The ultimate tensile strength of 304 stainless steel appears to vary from specimen to specimen. The tensile strength ranges from 878 MPa to 1006 MPa
2. The distribution pattern of the ultimate tensile strength can be reasonably described by the two-parameter Weibull distribution equation.
3. The characteristic tensile strength, σ_o, obtained is about 982 MPa. Furthermore, the Weibull

modulus (m) for the investigated material is found to be 26.893 inferring that the materials tend to fracture with a higher probability for every unit increase in applied tensile load.

4. The fracture statistics of the stainless steel were examined by plotting the survival probability of the specimen against the stress applied to the specimen. It has been observed that the relationship between the survival probability and the applied stresses can be described by the Weibull model. It also provides design engineers with a tool that will help them to present the necessary mechanical properties with confidence. For example, with a 0.90 reliability level, it was observed that the tensile strength of the present material will be 903 MPa.
5. The varying tensile strengths of stainless steel are due to their inherent internal structures, inferring that there is no specific strength value to represent mechanical behaviour. This study undoubtedly raises questions of assuming the tensile strength as an average of the experimental results. Therefore, the distribution and reliability of mechanical properties especially tensile strength must be described by the probability of function for their safe utilization in design and manufacturing.

ACKNOWLEDGEMENTS

The authors would like to thank the Civil Engineering Department, Military Institute of Science and Technology (MIST) and STEELTECH Company for supplying the 304-grade stainless steel material. The expert assistance by the technical staff in the Civil Engineering department for conducting the tensile test and the Mechanical Engineering department for preparing the specimen at MIST is also sincerely appreciated.

REFERENCES

Aksel, H., & Eren, O. (2015). A Discussion on the Advantages of Steel Structures in the Context of Sustainable Construction. *New Arch-International Journal of Contemporary Architecture*, *2*(3), 46–53. https://doi.org/10.14621/tna.20150405

ASTM standard 407-07. (2005). ASTM 407-07, Standard Practice for Microetching Metals and Alloys, *ASTM International*, West Conshohocken, PA, 2007, 1–21. https://doi.org/10.1520/E0407-07.2

ASTM E8/E8M-16ae1. (2013). Standard Test Methods for Tension Testing of Metallic Materials. *ASTM International*, 1–27. (Extracted on Dec. 02, 2020). Source: http://www.astm.org/Standards/E8.htm

Azeez, S., Mashinini, M., & Akinlabi, E. (2019). Road map to sustainability of friction stir welded Al-Si-Mg joints using bivariate weibull analysis. *Procedia Manufacturing*, *33*, 35–42. https://doi.org/10.1016/j.promfg.2019.04.006

Bahrami, A., & Taheri, P. (2019). A Study on the Failure of AISI 304 Stainless Steel, 1–7.

Bedi, R., & Chandra, R. (2009). Fatigue-life distributions and failure probability for glass-fiber reinforced polymeric composites. *Special Issue on the 12th European Conference on Composite Materials, ECCM 2006*, *69*(9), 1381–1387. https://doi.org/10.1016/j.compscitech.2008.09.016

Ben Fredj, N., Sidhom, H., & Braham, C. (2006). Ground surface improvement of the austenitic stainless steel AISI 304 using cryogenic cooling. *Surface and Coatings Technology*, *200*(16–17), 4846–4860. https://doi.org/10.1016/j.surfcoat.2005.04.050

Bergman, B. (1984). On the estimation of the Weibull modulus. *Journal of Materials Science Letters*, *3*(8), 689–692. https://doi.org/10.1007/BF00719924

Birbilis, N., Cavanaugh, M. K., & Buchheit, R. G. (2006). Electrochemical behavior and localized corrosion associated with Al7Cu2Fe particles in aluminum alloy 7075-T651. *Corrosion Science*, *48*(12), 4202–4215. https://doi.org/10.1016/j.corsci.2006.02.007

Bony, S. Z., & Rahman, S. (2014). Practice of Real Estate Business in Bangladesh: Prospects & Problems of High-rise building. *IOSR Journal of Business and Management*, *16*(7), 01–07. https://doi.org/10.9790/487x-16740107

Chakma, J. (2019). *Steel industry booming on mega projects*. (Extracted on Dec. 02, 2020). Source: https://www.thedailystar.net/business/news/steel-industry-booming-mega-projects-1735855

Datsiou, K. C., & Overend, M. (2018). Weibull parameter estimation and goodness-of-fit for glass strength data. *Structural Safety*, *73*, 29–41. https://doi.org/10.1016/j.strusafe.2018.02.002

Della-Rovere, C. A., Castro-Rebello, M., & Kuri, S. E. (2013). Corrosion behavior analysis of an austenitic stainless steel exposed to fire. *Engineering Failure Analysis*, *31*, 40–47. https://doi.org/10.1016/j.engfailanal.2013.01.044

Evans, A. G. (1983). Statistical aspects of cleavage fracture in steel. *Metallurgical Transactions A*, *14*(7), 1349–1355. https://doi.org/10.1007/BF02664818

Feng, Q. B., Li, Y. B., Carlson, B. E., & Lai, X. M. (2019). Study of resistance spot weldability of a new stainless steel. *Science and Technology of Welding and Joining*, *24*(2), 101–111. https://doi.org/10.1080/13621718.2018.1491378

Fukui, Y., Yamanaka, N., & Enokida, Y. (1997). Bending strength of an Al-Al3Ni functionally graded material. *Composites Part B: Engineering*, *28*(1–2), 37–43. https://doi.org/10.1016/s1359-8368(96)00018-2

Glaeser, A. M. (1997). The use of transient FGM interlayers for joining advanced ceramics. *Composites Part B: Engineering*, *28*(1–2), 71–84. https://doi.org/10.1016/s1359-8368(97)00039-5

Gürbüz, H., Şeker, U., & Kafkas, F. (2017). Investigation of effects of cutting insert rake face forms on surface integrity. *International Journal of Advanced Manufacturing Technology*, *90*(9–12), 3507–3522. https://doi.org/10.1007/s00170-016-9652-7

Hallinan, A. J. (1993). A Review of the Weibull Distribution. *Journal of Quality Technology*, *25*(2), 85–93. https://doi.org/10.1080/00224065.1993.11979431

Islam, F. A. S., Alam, M. M.. I., & Barua, S. (2016). Investigation on the uses of steel as a sustainable construction material in Bangladesh., *International Journal of Scientific Engineering and Applied Science (IJSEAS)*, 2(1), 41–52..

Islam, M. A. (2015). Corrosion behaviours of high strength TMT steel bars for reinforcing cement concrete structures. *Procedia Engineering*, *125*, 623–630. https://doi.org/10.1016/j.proeng.2015.11.084

Khatak, H. S., Gnanamoorthy, J. B., & Rodriguez, P. (1996). Studies on the influence of metallurgical variables on the stress corrosion behavior of AISI 304 stainless steel in sodium

chloride solution using the fracture mechanics approach. *Metallurgical and Materials Transactions A: Physical Metallurgy and Materials Science*, *27*(5), 1313–1325. https://doi.org/10.1007/BF02649868

Király, M., Antók, D. M., Horváth, L., & Hózer, Z. (2018). Evaluation of axial and tangential ultimate tensile strength of zirconium cladding tubes. *Nuclear Engineering and Technology*, *50*(3), 425–431. https://doi.org/10.1016/j.net.2018.01.002

Kumar, P. S., Acharyya, S. G., Rao, S. V. R., & Kapoor, K. (2017). Distinguishing effect of buffing vs. grinding, milling and turning operations on the chloride induced SCC susceptibility of 304L austenitic stainless steel. *Materials Science and Engineering A*, *687*, 193–199. https://doi.org/10.1016/j.msea.2017.01.079

Kweon, H. D, Kim, J. W., Song, O., & Oh, D. (2020). Determination of true stress-strain curve of type 304 and 316 stainless steels using a typical tensile test and finite element analysis. *Nuclear Engineering and Technology*, (in press). https://doi.org/10.1016/j.net.2020.07.014

Ma, Y., Zhang, J., Feng, P., Yu, D., & Xu, C. (2018). Study on the evolution of residual stress in successive machining process. *International Journal of Advanced Manufacturing Technology*, *96*, 1025–1034. https://doi.org/10.1007/s00170-017-1542-0

Mohd, S., Bhuiyan, M. S., Nie, D., Otsuka, Y., & Mutoh, Y. (2015). Fatigue strength scatter characteristics of JIS SUS630 stainless steel with duplex S-N curve. *International Journal of Fatigue*, 82, 371–378. https://doi.org/10.1016/j.ijfatigue.2015.08.006

Monrrabal, G., Bautista, A., Guzman, S., Gutierrez, C., & Velasco, F. (2019). Influence of the cold working induced martensite on the electrochemical behavior of AISI 304 stainless steel surfaces. *Journal of Materials Research and Technology*, *8*(1), 1335–1346. https://doi.org/10.1016/j.jmrt.2018.10.004

Monteiro, S. N., Nascimento, L. F. C., Lima, É. P., Luz, F. S. da, Lima, E. S., & Braga, F. de O. (2017). Strengthening of stainless steel weldment by high temperature precipitation. *Journal of Materials Research and Technology*, *6*(4), 385–389. https://doi.org/10.1016/j.jmrt.2017.09.001

Nur, S. A. (2016). Steel structures gaining popularity in cities. (Extracted on Dec. 02, 2020). Source: https://dailyasianage.com/news/28068/steel-structures-gaining-popularity-in-cities

Rahman, M. (2019). Curbing air pollution. *The Finincia Express*. (Extracted on Dec. 02, 2020). Source: https://thefinancialexpress.com.bd/views/views/curbing-air-pollution-1577111648

Sanaullah, M., Rahman, J., Ibrahim, I., & Rahman, M. S. (2019). Behavior of Concrete Filled Stainless Steel Tubular Column Under Axial Loads, *MIST Journal of Science and Technology*, *7*(1), 9–18.

Sungho, P., Noseok, P., & Jaehoon, K. (2010). A statistical study on tensile characteristics of stainless steel at elevated temperatures. *Journal of Physics: Conference Series*, *240*. https://doi.org/10.1088/1742-6596/240/1/012083

Sutanto, H. (2007). Residual stresses on high-speed milling of hardened steel using CBN cutting tool. *Journal Tecknolgi of Media Teknika*, *7*(2), 1-7.

Tiryakioğlu, M., Hudak, D., & Ökten, G. (2009). On evaluating Weibull fits to mechanical testing data. *Materials Science and Engineering A*, 527, 397–399. https://doi.org/10.1016/j.msea.2009.08.014

United Nations (2020). *World Economic Situation and Prospects 2020*. (Extracted on Dec. 02, 2020). Source: https://www.un.org/development/desa/dpad/publication/world-economic-situation-and-prospects-2020

Wang, H., Shi, Z., Yaer, X., Tong, Z., & Du, Z. (2019). High mechanical performance of AISI304 stainless steel plate by surface nanocrystallization and microstructural evolution during the explosive impact treatment. *Journal of Materials Research and Technology*, *8*(1), 609–614. https://doi.org/10.1016/j.jmrt.2018.05.010

Wang, Q. G., Apelian, D., & Lados, D. A. (2001). Fatigue behavior of A356-T6 aluminum cast alloys. Part I. Effect of casting defects. *Journal of Light Metals*, *1*(1), 73–84. https://doi.org/10.1016/S1471-5317(00)00008-0

Weibull, W. (1951). A Statistical Distribution Function of Wide Applicability. *Journal of Applied Mechanics*, 18, 293–297.

Zeng, H. H., Yan, R., Peng, F. Y., Zhou, L., & Deng, B. (2017). An investigation of residual stresses in micro-end-milling considering sequential cuts effect. *International Journal of Advanced Manufacturing Technology*, 91, 3619–3634. https://doi.org/10.1007/s00170-017-0088-5

MIJST
MIST International Journal of Science and Technology

Experimental Analysis on Safety System of a Simulated Small Scale Pressurized Water Reactor System with Intelligent Control

Md. Shakerul Islam, Altab Hossain*, Khalid Mursed, and Rafi Alam Chowdhury

Department of Nuclear Science and Engineering, Military Institute of Science and Technology (MIST), Dhaka, Bangladesh

emails: *shakerul@nse.mist.ac.bd; *altab76@gmail.com; murshedy2k@gmail.com; and arrafialam@gmail.com*

ARTICLE INFO

Article History:

Received: 14th April 2020
Revised: 17th June 2020
Accepted: 05th August 2020
Published: 16th December 2020

Keywords:

Water-based reactor
Intelligent control
Thermal hydraulic
Heat transfer
Safety

ABSTRACT

Reactors are widely used in the nuclear power plant due to the rapid demand for electricity by reducing the greenhouse effect. However, the effectiveness of the nuclear reactor depends on an adequate safety system. Hence, temperature and heat transfer are two critical parameters for any reactor in operation for which intelligent temperature control with an integrated safety system is essential. Therefore, the present study has emphasized the development of a simulated small-scale water-based reactor with intelligent control and safety system and examined through the analysis of thermal-hydraulic parameters. Radial heat transfer of an electric rod used as fuel in the primary circuit has been analyzed by taking sensor reading in various positions of the core. The developed system is self-controlled with all possible active and passive safety systems. Consecutively, the prototype has also been designed including manual adjustment to ensure a fail-safe environment. The system is capable to operate at temperatures between 80°C and 120°C, although the design can withstand up to 200°C. The data of the experiment are taken under the pressure of 200 kPa at 120°C temperature. Results show that heat output of 2116.09 kJ has been obtained from the system against heat input of 2514.80 kJ, which gives an efficiency around 16% of the developed system.

1. INTRODUCTION

Fossil fuels used in conventional thermal power plants cause many environmental problems. But nuclear energy does not emit greenhouse gases unlike coal and natural gas and hence, they do not contribute to climate change. Since the world tries to reduce global warming, nuclear power plant (NPP) is contributing to the energy mix by generating a significant amount of electricity. In an increasingly carbon-constrained future, nuclear power is becoming recognized as an integral part of the world's low-carbon energy solution (Ho *et al*., 2019). Nuclear power has grown quickly in the 1970s and 1980s, reaching a global installed capacity of 396 GWe today (IAEA, 2019). It is found that the annual load factor of nuclear power in China is about 90%, which is much higher than those of coal-fired power, wind power, and solar power (Zhen, 2016). It is noted that two types of light water reactors namely Pressurized Water Reactor (PWR) and Boiling Water Reactor (BWR), are commonly used in the world's nuclear power plants. However, one of the main differences between PWR and BWR is in the steam generation process. In general, PWR consisting of primary and secondary water circuit produces steam indirectly, whereas BWR consisting of a single water circuit produces steam directly. More precisely, in a PWR, the coolant being heat at high temperature using heat from the reactor core is forced to maintain its liquid form under high temperature due to high pressure. Subsequently, the heat produced from the primary water circuit is further transferred to the secondary circuit which turns into steam and rotates the turbine, thereby, producing electricity. On the other hand, in a BWR, steam produced directly by the boiling of water coolant is detached using steam separators placed above the reactor core, and thereby, rotating the turbine. Research shows that about 80% of operated nuclear power plants are of PWR and BWR typed light water reactor (Breeze *et al*., 2014). Ordinary water is used as coolant and moderator in BWR typed reactor in which, water is being boiled at the boiling point of 285°C at a pressure of 7.5 MPa, and the steam generated is used

directly to operate a steam turbine. However, the accident at Three Mile Island (TMI) has led to an essential improvement in the safety of nuclear plants throughout the world. The investigation shows that the human element had not been adequately included in previous safety considerations, and this observation prompted numerous advances in design and operating practices at nuclear plants. Other notable changes in both hardware and practices were research stimulated by accident (Kojima *et al*., 2007). Nuclear power generated through a controlled chain reaction is controlled through the four-factor formula (P´al & P´azsit, 2009). If the reaction cannot be controlled, then there is a possible chance of occurring major anomaly. After the Chernobyl accident in 1986, the importance of containment for severer accidents became highlighted (Balonov, 2013). The reactor core was partially melted down, thereby, many radioisotopes was released as the consequence of the accident and many people were evacuated from the exclusion zone (Miller, 1994). Again, the nuclear accident that occurred in Fukushima Daiichi in Japan was mainly caused by a massive tsunami which made the station completely blackout (Khan *et al*., 2018). Accident management was practiced both at Three Mile Island and Chernobyl, with significant consequences in both cases. The investigation of the TMI and Chernobyl accident has shown the failure of the management processes which are supposed to have an adequate safety culture. In both cases, there were weaknesses in design, operating practices, training, and feedback of operating information, and there was no organized mechanism to ensure that weaknesses were recognized and corrected. The rate of civil nuclear accidents over time since 1952 has been decreased significantly from the 1970s, reaching to be a stable level of around 0.003 events per plant per year (Wheatley *et al*., 2016). After Fukushima nuclear accident in Japan, the elements such as transparency, acceptability and communication capacity of nuclear safety information have emerged as an important part of key elements for nuclear safety regulation since 2010 (Kim *et al*., 2019). The Chernobyl accident has led the International Safety Advisory Group (INSAG) to accelerate the preparation of INSAG-3. From all the accidents, one of the most important lessons has been learned that the control system of any reactor must be robust, efficient, and reliable at the same time. Several studies have been performed on nuclear reactor to ensure adequate safety, temperature control with an integrated safety system (Gharib *et al*., 2011; Hossain *et al*., 2019; IAEA, 2002; Khan & Islam, 2019; Sunday *et al*., 2013; Vojackova *et al*., 2017; Nain *et al*., 2019). The literature shows that the thermal-hydraulic models through hot channel fuel centreline temperature play a significant role to safety-related parameters within the design limit (Rahman *et al*, 2014). However, the investigation was performed using computer code and the data were far to compromise the safety of the reactor. Hence, experimental, and theoretical studies on heat transfer, intelligent control and safety system are very important for any nuclear reactor. Moreover, it is found that experimental studies are important for making a relationship between the flow rate and electrical power of the motor driving the pumps which must be addressed in a nuclear reactor. Therefore, this study has been performed with the development of a simulated small-scale water based PWR reactor. Furthermore, the analysis has been carried out to evaluate the heat transfer, safety, and control system of a working reactor model.

2. MATERIALS AND METHODS

A simulated small-scale water based PWR reactor shown in Figure 1 is developed considering three parts: (i) thermal hydraulics, (ii) safety system, and (iii) intelligent control system in the Nuclear Laboratory of MIST.

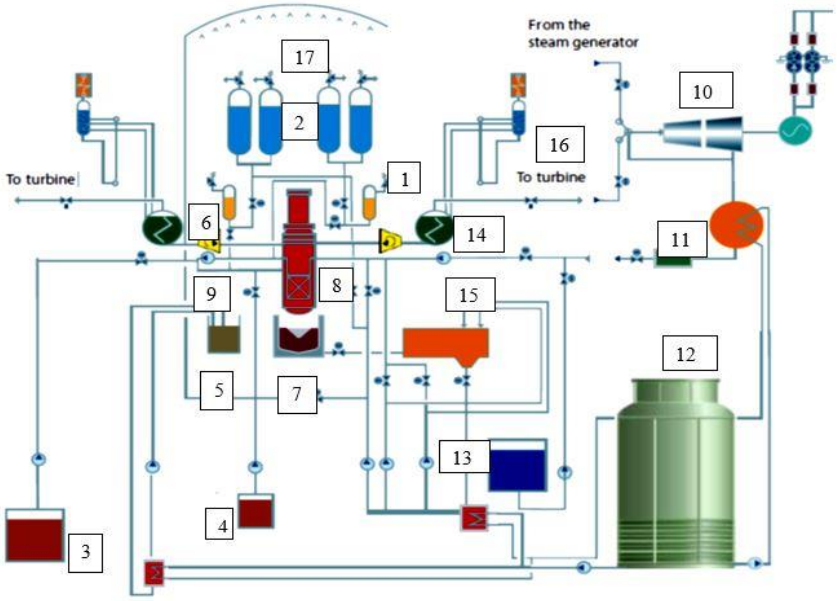

Figure 1: Schematic diagram of simulated small scale water-based reactor; (1) Hydro accumulator-1, (2) Hydro accumulator-2, (3) Emergency high-pressure boron injection system, (4) Emergency low-pressure boron injection system,(5) Spent fuel pool, (6) Cyclone, (7) Core catcher, (8) Reactor core, (9) Core coolant circulating pump, (10) Turbine, (11) Heat exchanger, (12) Cooling tower, (13) Demineralized water, (14) Pressure vessel for making saturated steam into superheated, (15) Main circulating pump, (16) Passive core containment cooling system, (17) Sprinkler system

Table 1
Key Output Parameters

Parameter	Symbol	Value	Unit
Heat input	qin	2514.80	kJ/kg
Heat output	qout	2116.09	kJ/kg
Net work	Wnet	398.71	kJ/kg
Thermal Efficiency	η	0.16	16%
The mass flow rate of steam	ṁ	0.00376	kg/s
Rate of Heat Rejection in Cooling Water	^{0}Qout	7.96	kJ/s
The mass flow rate of cooling water from the cooling tower	ṁcooling water	0.33	kg/s
Temperature difference at the cooling water inlet and outlet	ΔTcooling water	5.68	°C

The heat is first generated in the core and then it heats the water, which goes to the steam generator and generates steam. The produced steam is then transferred to the turbine to rotate and thereby, producing electricity through a generator. After rotating the turbine shaft, the waste heat goes to a heat exchanger by cooling down with the help of the cooling tower. Consecutively, with the help of the distillation again the cooled water goes back to the core.

A. Design Parameter Optimization

A thermal-hydraulic study has been performed in this work by considering temperature, amount of heat generation, amount of heat release, and flow measurement. Heat transfer used in this study using conduction and convection laws of the heating rod to cladding surface followed by coolant are shown in Equations (1) and (2).

$$\frac{Q}{t} = \frac{kA(T_2 - T_1)}{d} \tag{1}$$

where, Q is the heat transfer, t is the time, k is the thermal conductivity of the material, T_2 and T_1 are the temperatures of corresponding material at the inner and outer surface, and d is the thickness of the material.

$$q = h_c A(T_s - T_a) \tag{2}$$

where, q is heat transfer per unit time, A is heat transfer area, h_c is convective heat transfer coefficient T_s is surface temperature and T_a is coolant temperature. However, one of the important factors of the NPP life cycle is the condition of the reactor pressure vessel (RPV) and its fatigue life. The stainless steel used in this study has been investigated with DPA effect at 823 K temperature to a neutron fluence of 1×10^{25}n/m^2 (Ioka *et. al*, 2000). DPA generally is defined as displacement per atom is employed to normalize the radiation damage across the reactor containment. Equation (3) is used in this study to determine the thickness of the reactor containment material made of stainless steel.

$$t = \frac{P_i D_i}{2SE - 0.2P_i} \tag{3}$$

where, P_i is the internal pressure of the containment, D_i is the internal diameter of the containment, S is allowable stress, E is the joint efficiency and t is the material thickness. An ellipsoidal head is chosen with a thickness of 4.053 mm by using Eq. (3) which is the same as the hoop stress thickness of

the reactor pressure vessel. Since the minimum thickness of the wall chosen is 7 mm, the head thickness of 7 mm is adequate in this work. Table 1 represents the optimized parameters for developing the small-scale water-based reactor.

B. Development of Physical Model

The reactor core is divided into two parts- the lower half and the upper half along with an instrumentation channel. The instrumentation channel holds all the thermocouples. The body of the reactor core is constructed with stainless steel consisting of alloy composition of 17-20% Cr, 8-12% Ni, and 2% Mo to mitigate the corrosion. The upper half of the reactor core is made with glass to observe the thermal-hydraulic properties as well as steam separators. Three flow sensors have been used to measure the flow rate at the inlet and outlet. Basically, they send signals based on the amount of coolant flow. Then the recorded signals are multiplied with the necessary co-efficient to get the exact result. Two pressure sensors have also been used. Two types of safety systems have been utilized in the model: (i) active safety systems, and (ii) passive safety systems. Most of them are worked by a pulse feedback method here. Emergency Core Cooling System (ECCS) with high-pressure injection and low power injection module is included in the model. Both have a self-start-up algorithm means that they can work without any human interference. The sprinkler system of the containment is also included in the model which has a total of three stages. Each of the stages contains two sets of the sprinkler system. The whole containment is covered with a total number of six sprinklers. For station blackout, a gravity-driven water supply system is included in the model. It is basically worked by an electromagnet. When station blackout occurs, the electromagnet is demagnetized letting the water flow in the reactor core. Furthermore, an online passive air-cooling system is also integrated into the model. If all electrical components are failed, then the water from the hydro-accumulator is automatically processed to flood the core.

Each container is filled with 5 liters of water with a flowing rate of 0.3 liters per minute. The heat exchanger used in this study is shell and core type and consisted of sixteen 'U' loops. A four-stage water filtration system and two-stage containment air filtration systems have also been used in this model.

C. Development of Control System

An intelligent control system has been developed by using Microsoft visual basic for controlling the whole system. The code has been developed in the .Net platform. Figure 2 shows the power control flow chart of the overall system. From the figure, it is revealed that the thermocouple starts to measure the temperature after the initiation of the system. Based on the temperature obtained from the experiments, the thermocouple sends a signal to the microcontroller. The microcontroller compares the signal as per set temperature. If the reading matches well then it sends a signal to the controller unit so that the controller unit can readjust the power to maintain the stabilization of the system. Besides the code, all the microcontrollers are programmed with a self-maintained algorithm, from which most of them are PID based. With the help of an electromagnetic relay and using a variable resistor, the power can be controlled from the developed software by using a microcontroller.

Figure 3 shows the power control circuit of the overall system. With the help of a thermocouple, water level sensor, and pressure sensor, the condition of the reactor core is maintained by the microcontroller. Arduino Mega (Mega 2560, 16 MHz) is used for the experiment. This microcontroller is well known for its reliability along with 54 digital output, 15 analog input and 15 analog output. The microcontroller used in this study has two pulses with a time duration of 3 seconds. If any transient situation occurs, the sensors send the values which are not the same as setpoint values. If only a single pulse comes, the microcontroller considers it as a false count. If the second abnormal pulse is found, then the microcontroller starts the ECCS to maintain the setpoint values, which is programmed using the PID algorithm. If the reactor core pressure rises from a certain level, the high-pressure injection system starts automatically. In this study, K-type (MAX6675) thermocouple is used in the model to achieve the temperature of the heat source. Out of a total of 16 sensors, only 8 sensors are used to take the reading from the reactor core. The readings obtained using sensors are the axial and radial temperature of the core. The thermocouples are calibrated with a mechanical thermometer to get accurate results. Besides, the readings from the thermocouples are directly obtained at a computer monitor where I2C LED (32 bit) monitors are used for getting the same result for the redundancy. An advanced code is developed along with an advanced algorithm based on If-Else (Patnaikuni, 2017). Initially, thermocouples take data from the reactor core and then signals are sent to the microcontroller. Microcontroller analyzes these data, whether they are true or false. If the data are true, then they are displayed on the monitor. If false, then the microcontroller sends back the signal to the source. Besides the core, another 8 thermocouples are used to measure the temperature at the inlet, outlet, turbine, condenser, and cooling tower. Two pressure meters are used to take the pressure data from the core. Furthermore, an air quality sensor is used to analyze the quality of air. Also, several types of active and passive safety systems are included in the study. Most of them are worked by a pulse feedback method.

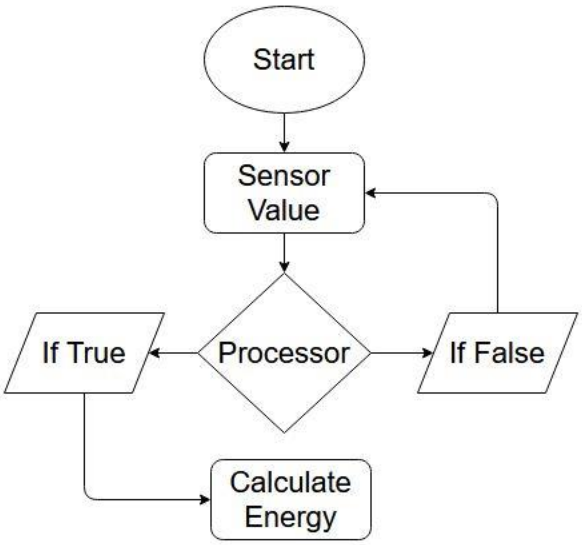

Figure 2: Power control flow chart of the overall system

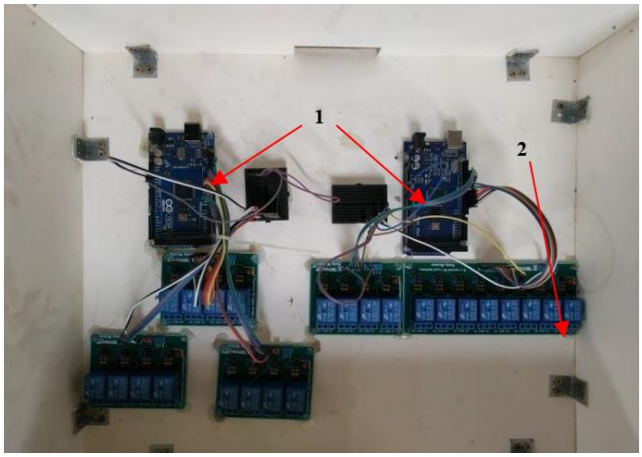

Figure 3: Circuit of control system; (1) Microcontroller, (2) Relay Module

Figure 4 shows the arrangement of thermocouples and heat generation source. Another three of them remain disconnected as back up. Three rows of thermocouples (80 mm distance) are installed in the core for taking axial and radial temperature distribution. Each row contains three thermocouples of which two are used to take radial temperature, and one is used to take the axial temperature. The mass flow rate of steam is considered as 0.00376 kg/s in this study. Since the mass flow rate of steam is very small, the turbine is made as very light weighted. YF-S201 (hall-effect, 15ma-5v) flow sensor is used in this study. Similarly, the network is calculated as 398.70 kJ/kg and thereby producing thermal power of 1500 W.

Figure 5 shows the lower half of the core with the instrumentation channel. The instrumentation channel holds all the thermocouple. The body of the core is constructed with stainless still to mitigate the corrosion. Figure 6 shows the upper half of the core, which is made with glass to observe the thermal-hydraulic properties as well as steam separator. Three flow sensors have been used to measure the flow rate of inlet and outlet for sending analog signals based on the amount of coolant flow. Two pressure sensors have been used to measure the flow rate of inlet and outlet for sending analog signals based on the amount of coolant flow. Six coils are installed for heat generation. Each of them has a 500W capacity. Three of them are in the operational phase for fulfilling the energy supply for the whole system. Figure 7 shows the setup of the developed model. High-pressure injection and low-pressure injection systems work in the same procedure. The only difference from ECCS is that they also take pressure into consideration. Besides, the ECCS and containment spray system and online air filtration system are also included in the model project. The main circulations pump works based on the core temperature. The speed of the pump varies with increasing or decreasing core temperature. The microcontroller takes the temperature data from the core. Then based on the temperature data, it sets the speed of the motor which, is executed by the PWM signal sent to the pump control driver.

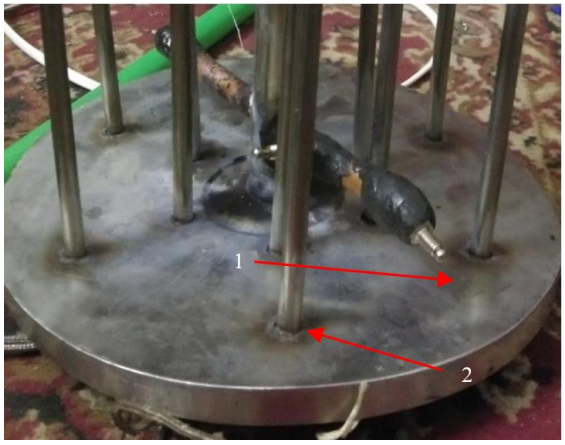

Figure 4: Thermocouple and heat source in the core; (1) Thermocouple, (2) Heat source

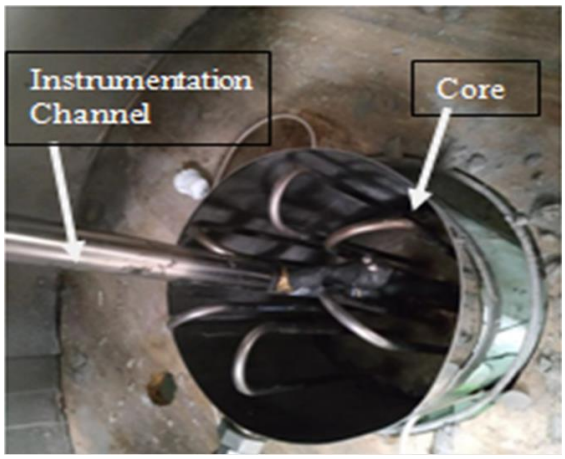

Figure 5: Instrumentation channel and core

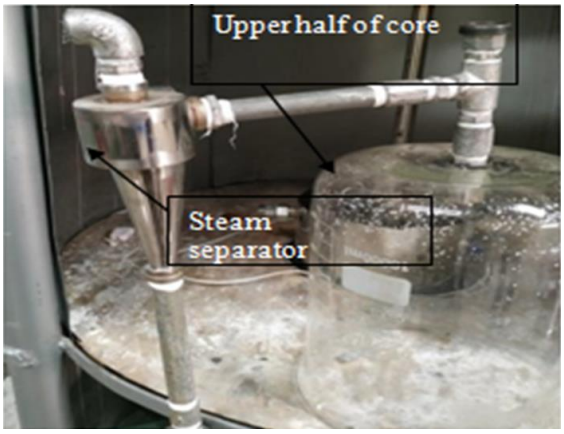

Figure 6: Final setup of the developed model

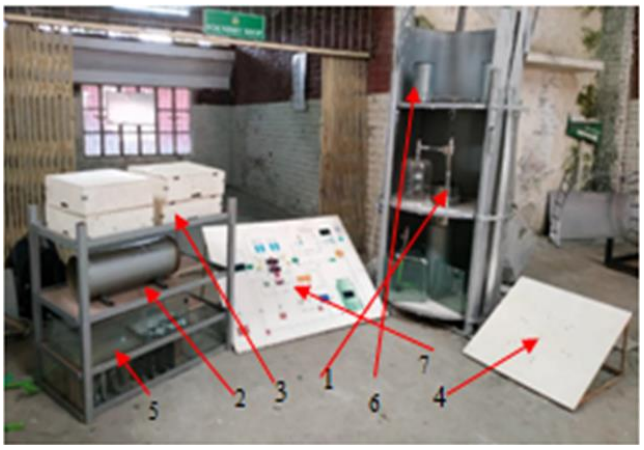

Figure 7: Final setup of the developed model; (1) Core, (2) Heat exchanger, (3) Control system, (4) Heating rod indicator, (5) Distillation and water purification, (6) Hydro accumulator, (7) Display board

3. RESULTS AND DISCUSSION

The results obtained from the experimental setup are recorded and plotted in a graphical system. Figure 8 shows the axial and radial temperature distribution over time. The x-axis is denoted as time in s while the y-axis is represented as the temperature in ℃. The blue line represents the axial temperature with thirty seconds time duration while the green line represents the radial temperature distribution. Figure 8 reveals that the axial and radial temperatures begin to decrease after the creation of an anomaly situation. Figure 9 shows the steam flow rate and water inlet flow rate in kg/s in comparison with time in s. A thirty-second time interval is considered for recording data. The blue line indicates the steam flow rate, and the red line indicates the water inlet flow rate. The x-axis is denoted as time, and the y-axis is denoted as a flow rate. Besides, all the safety system works well while operating the system. However, to evaluate the safety system of the model, an anomaly of small break LOCA has been made manually.

Figure 10 represents the relationship between the flow rate of ECCS and the reduction of core temperature with time. It is noticed that the activation of ECCS starts automatically after crossing the core temperature of 97°C at atmospheric pressure. According to Westinghouse Technology, the ECCS charging rate is 150 gpm. The ECCS is designed by scaling in such a way that it can

supply a maximum of 5 L of water per minute, i.e., 0.087 kg/s to the core. The transient situation has been made after the functional operation of the reactor with a period of 210 seconds. From Figure 10, it has been observed that the ECCS flow rate is stable during 0 to 210 seconds and no transient situation occurred. However, a transient situation occurred after 210 seconds where the temperature of the core increases suddenly and thereby, starting ECCS. ECCS has been deactivated after 420 seconds as the temperature is decreased and reached under a margin of safety. Similarly, the reduction of decay heat based on the temperature in comparison with time plays an important role. It is noticed that the temperature has increased quickly and reached a peak during the transient period of 210 s to 420 s. At this stage, the safety system has been started to work and hence the temperature is decreased which represents the reduction of decay heat.

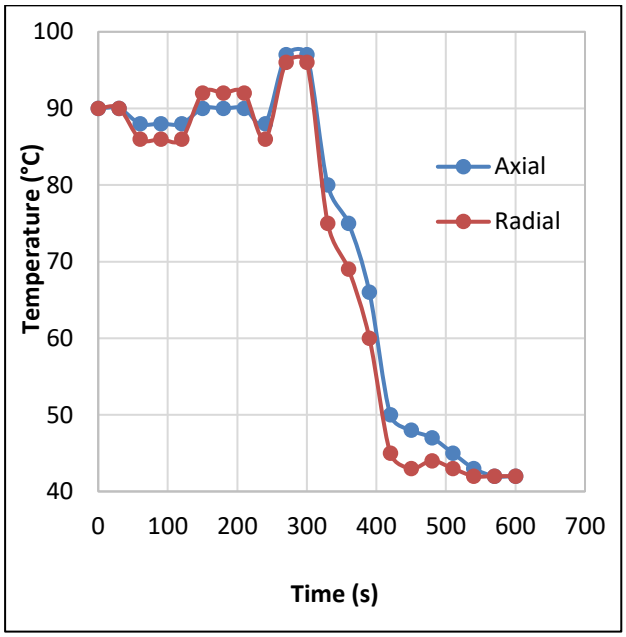

Figure 8: Temperature distribution versus time

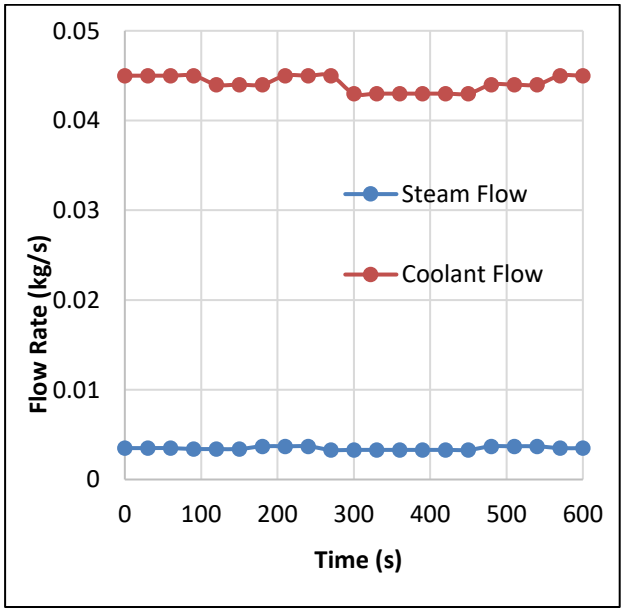

Figure 9: Flow rate of steam and water inlet versus time

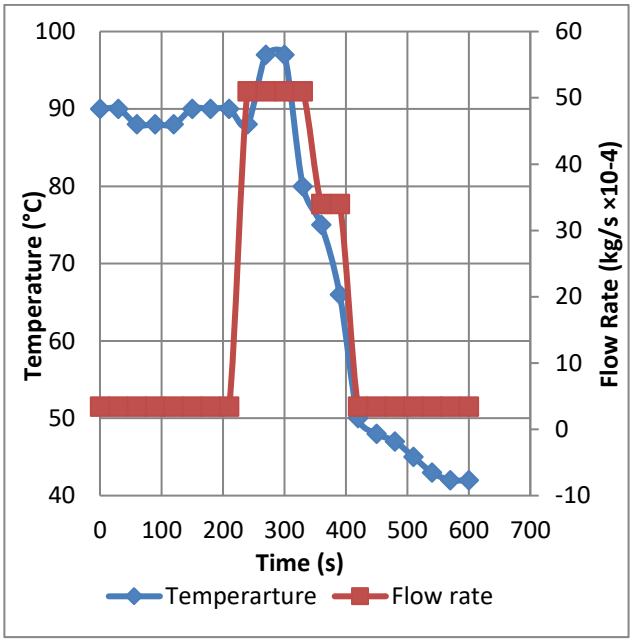

Figure 10: Graphical relationship between the flow rate of ECCS and reduction of core temperature with time

Figure 11 represents the reduction of power load based on the temperature in comparison with time. Surprisingly, the reactor has tripped with the decrease of temperature drastically as the result of transient which results in the reduction of net power. Subsequently, the power is reached to the minimum value, i.e., 0 after 600 s and thereby, reducing power. From Figure 11 it is seen that power decreases gradually from 210 to 600 seconds

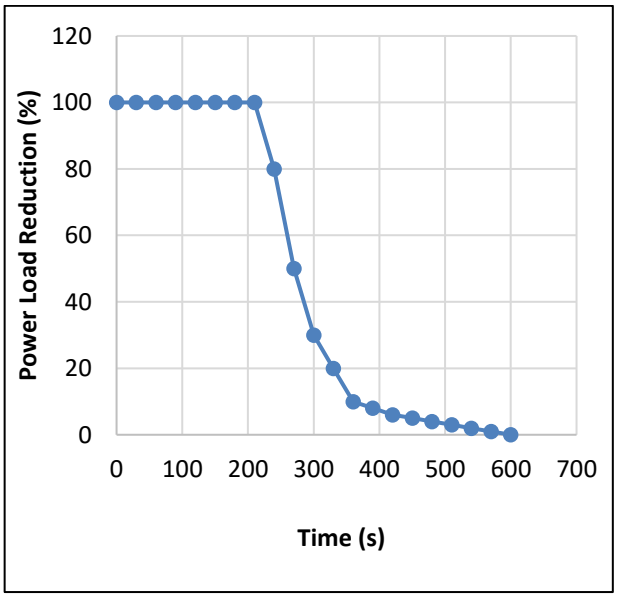

Figure 11: Graphical representation of the power load reduction versus time

after the reactor trip. On the other hand, humidity has been found at a satisfactory level. The reason behind this is that the online water purification and containment air-purification systems work very swiftly. Not only this but also a high-pressure injection system and a low-pressure injection system work perfectly. The gravity-driven hydro accumulator for station blackout also works perfectly

supplying 2 L water during station blackout. The passive heat removal system has been found as working perfectly.

4. CONCLUSIONS

The analysis has been performed to evaluate the thermal-hydraulic properties of a working reactor model. Theoretical calculations have been performed to construct the reactor model and examine the effect of heat transfer. Temperatures, flow rates, and pressures have been considered as main thermal-hydraulic properties. It is revealed that the system is capable to operate at temperatures between $80°C$ and $120°C$, although the design can withstand up to $200°C$. Similarly, the system can withstand pressure up to $600\ kPa$ though the working pressure is not more than $500\ kPa$. The data of the experiment are taken under the pressure of $200\ kPa$ at $120°C$ temperature. However, error analysis has not been done but data has been repeated six times for which almost similar data has been obtained and found no significant variation. The results show that a heat output of $2116.09\ kJ$ has been obtained from the system against a heat input of $2514.80\ kJ$, which gives a network of $398.71\ kJ$. Furthermore, the efficiency is found as 16% proving the effective performance of the developed system. However, specific conclusions can be drawn from the study are as follows:

1. The average axial and radial temperatures have been found as 93℃ and 90℃ with $0.021\ kg/s$ steam outlet and $0.045\ kg/s$ water inlet.
2. $0.45 - watt$ power has been obtained against the energy insertion of 400 joules at a pressure of $1.5\ atm$.
3. The developed intelligent control system is highly stable.

ACKNOWLEDGEMENTS

The authors would like to thank the Military Institute of Science and Technology (MIST) for providing financial support and laboratory facilities.

REFERENCES

Balonov, M. (2013). The Chernobyl Accident as a Source of New Radiological Knowledge: Implications for Fukushima Rehabilitation and Research Programmes. *Journal of Radiological Protection*, 33, 27-40.

Breeze, P. (2014). *Nuclear power Generation Technologies*, Newnes Publication. 3rd Edition, Elsevier Ltd.

Gharib, M., Yaghooti, A. & Buygi, M. O. (2011). Efficiency Upgrade in PWRs, *Energy and Power Engineering*, 3, 533-536.

Ho, M., Obbard, E., Burr, P. A. & Yeoh, G. (2019). A Review on the Development of Nuclear Power Reactors, *Energy Procedia*, 160, 459-466.

Hossain, A., Islam, S., Hossain, T, Salahuddin, A. Z. M & Sarkar, A. R. (2019). An Intelligent Approach for Thermal-Hydraulic Studies on Safety and Efficiency of Nuclear Power Plant. *Energy Procedia*, 160, 436-442.

IAEA (2002). Accident Analysis for Nuclear Power Plants. *IAEA Safety Reports Series* No. 23, IAEA, Vienna.

IAEA (2019). Energy, Electricity and Nuclear Power Estimates for the Period up to 2050. *IAEA Reference Data Series No. 1*. 2019 Edition, IAEA, Vienna.

Ioka, I., Yonekawa, M., Miwa, Y., Mimura, H., Tsuji, H. & Hoshiya, T. (2000). Effect of Helium to dpa Ratio on Fatigue Behavior of Austenitic Stainless Steel Irradiated to 2 dpa, *Journal of Nuclear Materials*, 283-287, 440-445.

Khan, A. H., & Islam, M. S. (2019). Prediction of thermal efficiency loss in nuclear power plants due to weather conditions in tropical region, *Energy Procedia*, 160, 84-91.

Khan, A. H., Hasan, S. & Sarkar, M. A. R. (2018). Analysis of Possible Causes of Fukushima Disaster, *International Journal of Nuclear and Quantum Engineering*, 12(2), 53-58.

Kim, J. S., Park, S. Y. & Lee, D. H. (2019). Changes and Prospects of Safety Regulation Activities in Korean Nuclear Safety Research, *International Journal of Innovative Technology and Exploring Engineering*, 8(852), 777-783.

Kojima, T. & Sato, Y. (2007). Variations of a Passive Safety Containment for a BWR with Active and Passive Safety Systems, *Journal of Nuclear Engineering and Design*, 237, 74-86.

Miller, K. L. (1994). The Nuclear Reactor Accident at Three Mile Island, Radiographics, 14(1), 215-224.

Nain, H. M. Z., Islam, M. S. & Khan, A. H. (2019). A Study on Thermal-Hydraulics Characteristics for Designing a Shell and Tube Condenser for a 1200 MWe Nuclear Power Plant. *J. Bangladesh Acad. Sci.* 43(2), 181-189.

P´al, L. & P´azsit, I. (2009). The Fast Fission Factor Revisited. Nuclear Science and Engineering, 161(1), 111-118.

Patnaikuni, D. R. P. (2017). A Comparative Study of Arduino Raspberry Pi and ESP8266 as IoT Development Board. *International Journal of Advanced Research in Computer Science*, 8(5), 2350-2352.

Rahman, M. M., Akond, M. A. R., Basher, M. K., & Huda, M. Q. (2014). Steady-State Thermal-Hydraulic Analysis of TRIGA Research Reactor, *World Journal of Nuclear Science and Technology*, 4, 81-87.

Sunday, J. I., Daniel, R. E., & Okibe, A. E. (2013). Simulation of Safety and Transient Analysis of a Pressurized Water Reactor using the Personal Computer Transient Analyzer, *Leonardo Electronic Journal of Practices and Technology*, 22, 93-105.

Vojackova, J., Novotny, F. & Katovsky, K. (2017). Safety Analyses of Reactor VVER 1000, *Energy Procedia*, 127, 352-359.

Wheatley, S. Sovacool, B. K. & Sornette, D. (2016). Reassessing the Safety of Nuclear Power. *Energy Research & Social Science*, 206, 1-5.

Zhen, Y. Q. (2016). Safety and Effective Developing Nuclear Power to Realize Green and Low-carbon Development. *Advances in Climate Change Research*, 7(1–2), 10-16.

MIJST
MIST International Journal of Science and Technology

Corrosion Behavior of Copper Based Heat Exchanger Tube in Waters of Bangladesh Region at Varied Temperature and Flow Velocity

M. Muzibur Rahman[1*] and S. Reaz Ahmed[2]

[1] Department of Naval Architecture & Marine Engineering, Military Institute of Science and Technology, Dhaka, Bangladesh
[2] Department of Mechanical Engineering, Bangladesh University of Engineering and Technology, Dhaka, Bangladesh

emails: [1*]*muzib1061@name.mist.ac.bd*; [2]*srahmed@me.buet.ac.bd*

ARTICLE INFO

Article History:

Received: 30th April 2020
Revised: 06th June 2020
Accepted: 04th August 2020
Published: 16th December 2020

Keywords:

Corrosion
Copper tube
Heat exchanger
River vs sea water
Life span estimation

ABSTRACT

Heat exchangers used in the ships are mostly of water-cooled shell and tube type, whose tube stacks are made of copper-based materials due to the requirement of high corrosion resistance and high thermal conductivity. Even though, the copper made heat exchanger tubes do fail on board ships because of corrosion. More point of contention arises when it is manufactured by companies that have limited supporting data and documentations. In this context, the present paper investigates the corrosion behavior of copper tubes of heat exchanger to assess the life span of the tube stack for on-board applications. A series of experiments have been undertaken to investigate the corrosion rates of copper tubes in sea water and river water with flow velocity of 1.0 m/s, 1.5 m/s and 2.0 m/s for the tube side entry temperature of 20°C. The same experiments have been repeated for the shell side temperatures of 20°C, 40°C, 60°C and 80°C. The investigations have revealed that the corrosion in sea water is about three times higher than that of river water. The increases in temperature and flow velocity have increased the rate of corrosion to a significant level contributing to shorten the life span.

1. INTRODUCTION

Copper is chosen for the tube stacks of heat exchanger due to its superior thermo-mechanical properties such as thermal conductivity, resistance to corrosion, strength, and formability (Collini, 2012). It may be mentioned that copper is located in the periodic table in line of noble metals, and thus copper is considered as immune from corrosion. The corrosion immunity of copper is also based on a postulation on the existence of native copper in the earth's crust (Davis, 2001). In the atmosphere, a very thin layer of brownish-green or greenish blue in color known as patina is formed (Graedel *et al*., 1987; Leygraf *et al*., 2019). Established patina becomes stable and remains as a permanent part of the copper object in the atmosphere. Examples of the corrosion resistance of copper materials are artifacts that have been found in nearly pristine condition after having been buried in the earth for thousands of years, and copper roofing in rural atmosphere has been found to corrode at rates of less than 0.4 mm in 200 years (Cramer & Covino, 2005, pp. 125). But, in water, copper corrodes due to number of factors as considered differently by different researchers (Hedin *et al*., 2018; Hultquist *et al*., 2009, 2011 & 2015; Hultquist, 2015; Simpson & Schenk, 1987; Szakálos *et al*., 2007). According to a group of researchers (Hultquist *et al*. 2015), the oxygen is consumed through hydrogen-oxygen reaction and the hydrogen is coming out from the reaction of copper with water. It is considered that the hydrogen-oxygen reaction is faster than the formation rate of the initially atomic hydrogen from the corrosion reaction itself on copper (Hultquist *et al*., 2015) and it is not possible to detect the hydrogen released from copper if the supply rate of oxygen to the surface exceeds the rate of hydrogen generation; and copper is considered erroneously as corrosion resistant (Hultquist *et al*. 2009 & 2011). On the other hand, few researchers (Simpson & Schenk, 1987; Hedin *et al*., 2018) have expressed the disagreement on the corrosiveness of copper in pure water.

However, corrosion of copper in sea water is accepted by all the mariners as well as researchers due to aggressiveness of ingredients like dissolved oxygen, chloride, sulphate, dissolved solids, suspended solids etc.

present in the sea water (Abdallah *et al*., 2009; Farro *et al*., 2009; Francis, 2010; Gudas & Hack, 1979; Nunez *et al*., 2005; Orozco-Cruz et *al*., 2017; Pehkonen *et al*., 2002; Rahmanto *et al*., 2002; Schumacher, 1979; Zakowski *et al*., 2014). Beside the aggressive ingredients, few dynamic parameters such as velocity, pressure, temperature, conductivity, pH value, etc. are playing some role in the corrosion behavior of metal in contact with sea water (Gerasimov & Rozenfeld, 1958; Kong *et al*., 2017; Kristiansen, 1977; Lee *et al*., 2016; Mor & Beccaria, 1979; Poulson, 1993; Roy *et al*., 2018; Sabri *et al*., 2012; Utanohara & Murase, 2019; Wan *et al*., 2012; Yatsenko *et al*., 1999). Moreover, various types of corrosion attacks can occur to the marine equipment made up of copper materials exposed to sea water. In view of above, the corrosion behaviors of metals including copper coming in contact with sea water especially during operations at elevated temperature along with significant flow velocity need to be characterized at specific water and environment conditions to assess the performance of marine machinery (Pehkonen *et al*., 2002).

Bangladesh being a maritime nation with long glory of shipbuilding heritage must have development in marine sector (Rahman, 2017). At the same time, a good number of vessels are plying in the inland water ways and at the coast of Bangladesh, which use river/sea water in heat exchangers to cool fresh water and lubricating oil of marine engines for propulsion and power generation. This requirement pushes the stake holders to look for reference data to have design allowances and life span assessment of marine equipment especially the heat exchanger on the issue of corrosion. But, unfortunately, necessary data for making decisions based on experimental results on corrosion are neither available to mariners nor even to local shipbuilding industries. One of such cases is the reliability problem due to absence of data of locally manufactured shell and tube type heat exchanger having copper tube stack.

At this juncture, it is very important to carry out the study on characterization of corrosion behavior of materials commonly used on board ships, which are especially coming in contact of sea water so that the shipbuilding can be enhanced as the real 'thrust sector' of national economic progress with the implementation plan of sustainable development goals (SDGs). To this effect, the present work is an attempt to investigate the corrosion behavior of locally made copper heat exchanger tubes to be used in the inland river water as well as coastal sea water environment of Bangladesh region.

2. MATERIALS AND EXPERIMENTAL DETAILS

To investigate the corrosion behavior of copper-based tube stack of shell and tube type heat exchanger for onboard ships with marine propulsion and power generation engines, two bundles of copper tubes manufactured in a local shipyard of Bangladesh for coastal vessels were collected. Each tube was of 400 mm length, 9.525 mm outer diameter and 1.245 mm (18 BWG) wall thickness. Before the corrosion testing experiments, the chemical composition of the tube material was tested using XRF machine (model: Olympus DPO-2000-CC having silicon drift detector for element identification) and microstructures were observed using computer interfaced Optical Electronic Microscope (model: Nikon BW-S500 having 4.19 Mpixel camera). The chemical composition of tube is found to be of 99.934% Cu, 0.019% Si, 0.016% P, 0.018% Fe, and 0.013% Ni.

The heat exchangers for ships are supposed to cool the engine lubricating oil and jacket water through an engine driven pump that supplies water from river or sea according to the plying location of the ship. The designated ship is designed to be operated from Khulna to Chittagong, and thus the heat exchangers would use inland water near Khulna area for river cruise as well as sea water during crossing the Bay of Bengal up to Chittagong. Considering the operational requirements of the ship, two identical experimental set-up arrangements were prepared, i.e., one for river water and another for sea water. Accordingly, 5000-liter water from each location, i.e., Rupsha River and the Bay of Bengal was collected for the experimental purpose. The laboratory test result of the collected water is presented in Table 1.

Table I
Contents and properties of water used for investigation

Parameter	River Water	Sea Water
pH	7.08	7.14
Total Dissolved Solids (mg/liter)	250	28000
Total Suspended Solids (mg/liter)	15	48
Chloride (mg/liter)	4500	21000
Sulphate (mg/liter)	--	1320
Dissolved Oxygen (mg/liter)	6.55	7.29
Electric Conductivity (μS/cm)	450	48000

The components for each experimental set-up include pumps, tanks, flexible pipes, fittings, manifold, heat exchanger tubes, flow meter, thermometers, thermostat, relay, electric heater, etc. The straight tubes were placed with the removable headers and manifolds in the experimental set-up to observe their corrosion behavior using gravimetric method. The operating temperature of the heat exchanger of a marine engine remains normally from 45℃ to 75℃ on shell side for the temperature of lubricating oil and jacket water due to variation of engine load, and in the tube side, the cooling water temperature is from 18℃ to 30℃ due to seasonal variation. Therefore, experiments were carried out for the shell side temperatures of 20℃, 40℃, 60℃ and 80℃ so that corrosion behavior against these temperatures can be obtained. For the experiment at 20℃, normal fresh water was passed through the shell side, and for 40℃, 60℃, and 80℃, hot water was circulated using electric heaters to maintain the temperature during each experiment. The cooling water was stored in the open type tank for natural air cooling and an arrangement was made on the return line of tube side cooling water to spray in the atmosphere for maintaining the normal temperature. Both hot water and cooling water were reused with closed circuit arrangements as shown in Figure 1.

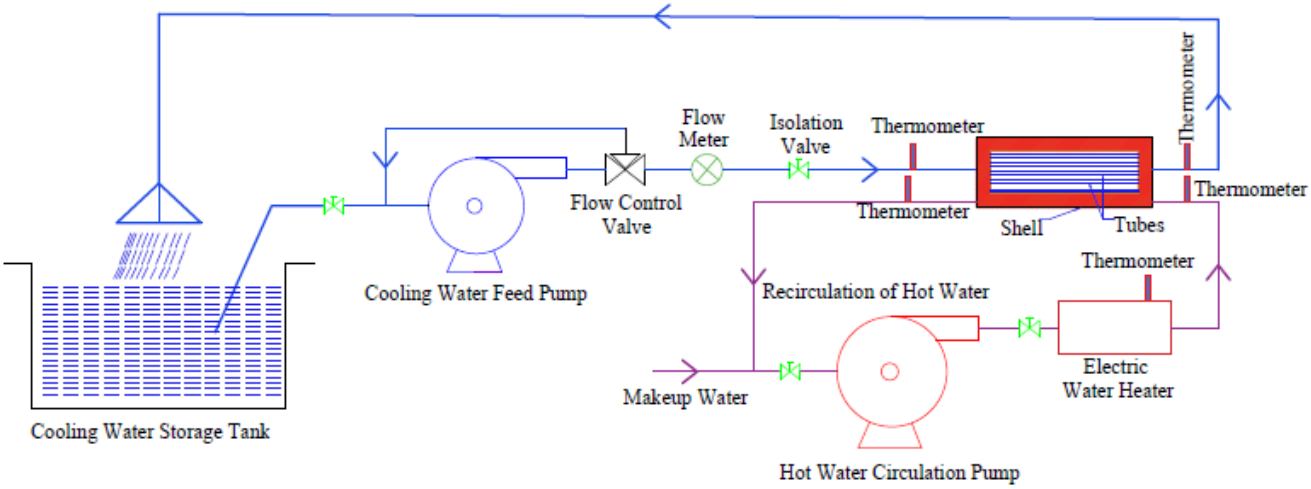

Figure 1: Layout of Experimental Setup Arrangement

After every designated period, the pump was stopped for a very short time; tubes were removed from the system and cleaned in distilled water to investigate weight, thickness and microstructures and fitted back. The weighing machine (model: Sartorius Entris 224-1S having pan diameter of 90 mm with the maximum weighing capacity of $220g$) of $0.1mg$ precision and ultrasonic thickness gauge (model: CG100 ABDL having measurement resolution of $0.01mm$) were used for the experimental purposes. The test readings were taken after one day, three days, six days, twelve days, eighteen days, twenty-four days and finally thirty days. On completion of thirty days operation, the changes in weight and dimensions were found to be very nearer to the immediately previous readings and thus it was considered as one complete cycle of the experiment. The same experiment was repeated for different operating temperatures and flow velocities. Likewise, three cycles of experiments were conducted to get the mean corrosion so that life span of heat exchanger tube could be calculated. The mathematical expressions used for calculating weight loss and corrosion rate are following the ASTM manual as given below (Baboian, 2005).

Amount (weight) loss of metal:

$$\Delta W = \frac{(W_o - W_f)}{A} \quad (1)$$

Corrosion rate:

$$R_{corr} = \frac{(K \, x \, \Delta W)}{(\rho \, x \, T)} \quad (2)$$

Where,

W_o = *Initial weight* (g)

W_f = *Weight after designated period* (g)

ΔW = *Weight loss per exposed surface area* (g/cm^2)

A = *Exposed surface area* (cm^2)

R_{corr} = *Corrosion Rate (mm per year, i.e., mmpy)*

K = *Unit conversion factor*

ρ = *Density of metal* (g/cm^3)

T = *Exposed time* (day)

3. RESULTS AND DISCUSSION

A. *Trend Analysis of Corrosion for River Water Environment*

In chemical terms, copper is demarcated in the noble metal family and considered as highly resistant to corrosion and oxidation. Copper's resistance to corrosion is attributed mainly to a thin oxide film called patina that forms on the surface of copper when exposed to a medium. This patina firmly adheres to the outer surface of the copper material and can protect the underlying copper layers from further corrosion (Graedel *et al.*, 1987; Leygraf *et al.*, 2019). However, the water chemistry and other factors cause the medium increasingly aggressive towards copper breaking up the patina to some extent. This phenomenon is comprehensive in the gravimetric analysis of the present experiment. Here, the loss of specimen weight per unit surface area (g/cm^2) exposed to the corrosive media is calculated using Equation (1) for four temperatures that are important to the operations of marine engines. Figure 2 presents the copper leaching in contact of river water against the period of operations while flowing through the copper tubes of heat exchanger at a velocity of 1.0 m/s for the external shell temperatures of 20℃, 40℃, 60℃, and 80℃. It is observed that the weight loss is increased with the increase of operating period, and all the curves are steeper at the initial tenure of attack with gradual flattening over further period. After 30 days operations, the weight loss curves have no incremental gradient and thus the slopes reach towards almost zero. At the same time, weight loss is found to be higher for higher temperature over the whole operating period. On completion of one day's operation, weight loss per unit exposed surface for the operating temperatures of 20℃, 40℃, 60℃, and 80℃ are found to be $229 \times 10^{-6}\ g/cm^2$, $314 \times 10^{-6} g/cm^2$, $399 \times 10^{-6}\ g/cm^2$, and $492 \times 10^{-6}\ g/cm^2$, respectively, and after 30 days operations, the copper tubes have lost $1978 \times 10^{-6}\ g/cm^2$, $2139 \times 10^{-6}\ g/cm^2$, $2249 \times 10^{-6}\ g/cm^2$, and $2343 \times 10^{-6}\ g/cm^2$, respectively. Therefore, after 30 days' operation, weight loss on average is increased by 8.63, 6.81, 5.64, and 4.76 times from the weight loss of the first day. For the change in operating temperature from 20℃ to 80℃, the weight loss is

increased on average by 18.45%. In other words, the average weight loss is increased by $6.98 \times 10^{-6}\ g/cm^2/$ ℃. The average value of change in weight loss has been taken for the change in operating temperature from 20℃ to 40℃, from 40℃ to 60℃, and from 60℃ to 80℃. It is because the effect of change in thermal condition on corrosion is not linear, rather in many cases it is complex phenomenon and the corrosion does not have stable correlation with respect to temperature (Kong *et al*., 2017; Kuźnicka, 2009; Lee *et al*., 2016; Melchers, 2001; Mor & Beccaria, 1979; Wan *et al*., 2012).

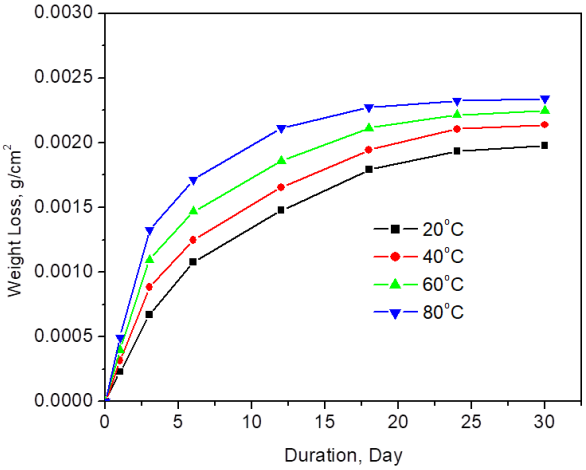

Figure 2: Weight loss per unit exposed surface against operating period for operating temperatures of 20℃, 40℃, 60℃, and 80℃ with the river water flow velocity of 1.0 m/s

Basically, the river water contains certain amount of dissolved oxygen, total dissolved solids (TDS), total suspended solids (TSS) and chlorides as observed through laboratory tests, and thus the environment is aggressive enough to make the copper tube susceptible to corrosion. Further notable issues are general (uniform or galvanic) corrosion over the exposed surface area because of electro-chemical phenomenon, erosion corrosion due to flow velocity of water through the tube and thermal effect due to variation in operating temperatures. There is a close relation between solution conductivity and corrosion reactions also. Again, the electrolyte conductivity increases with the increase in temperature due to enhanced mobility of ions (Gerasimov 1958; Wang *et al*., 2016). The conductivity of most natural water increases with the increase in temperature by 2 to 3 percent per degree Celsius (Miller, 1988). Due to higher conductivity at higher temperature, copper particles are released from the patina, and some copper atoms move away with the flow of water; but some atoms stay at the vicinity if the flow of water is not too turbulent. It results in the formation of copper hydroxychloride due to presence of chloride in the water (Abdallah *et al*., 2009). As a result, significant increase in weight loss is observed for the operating temperature of 60℃ and 80℃.

Based on the loss of weight, corrosion rates have been calculated using Equation (2) at the operating temperatures of 20℃, 40℃, 60℃, and 80℃ for different time intervals up to 30 days. Figure 3 depicts that the corrosion rate is the highest at the initial attack period, and then, it is reduced gradually but nonlinearly for all operating temperatures with the flow velocity of 1.0 m/s.

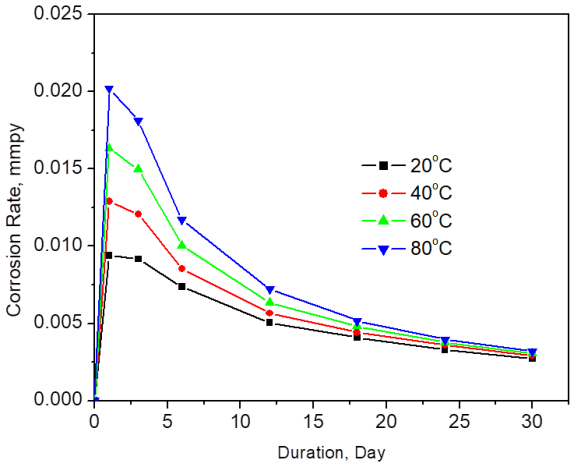

Figure 3: Corrosion rate against corrosion period for the variation of operating temperature with the river water flow velocity of 1.0 m/s

After 30 days of operations, corrosion rates are found to be almost steady showing minimum values. Copper reacts with dissolved oxygen and forms at first cuprous oxide which reacts with oxygen to procedure cupric oxide. These copper oxides react with the available anions in the vicinity to form compounds further (Imai *et al*., 2009; Lee *et al*., 2016; Zakowski *et al*., 2014). The time delay in the formation of copper oxides and development period of the patina in stable state might be the reason for the highest corrosion rate to be occurred at the initial attack period. The thermal effect on corrosion rate is as like that of weight loss, i.e., higher corrosion rate is witnessed for higher operating temperature.

It is observed that the corrosion rate gets affected by the velocity of fluid flow inside the tube also (Kuźnicka, 2009; Utanohara & Murase, 2019). Figure 4 illustrates the effect of changing flow velocity of 1.0 m/s, 1.5 m/s, and 2.0 m/s on the rate of corrosion at the operating temperature of 80℃. Since the cooling water flow velocity for marine engines are normally maintained within 2.0 m/s to ensure the proper suction of the pump from the sea under the conditions of all six degrees of ship motion, the effect of velocity on corrosion rate is not that significant. However, for the initial attack, the corrosion rates for the flow velocity of 1.0 m/s, 1.5 m/s, and 2.0 m/s are found to be $20.2 \times 10^{-3}\ mmpy$, $20.9 \times 10^{-3}\ mmpy$, and $21.6 \times 10^{-3}\ mmpy$ respectively, i.e., the corrosion rate has been increased by 6.8% for the change of flow velocity from 1.0 m/s to 2.0 m/s.

B. Trend Analysis of Corrosion for Sea Water Environment

Like the river water environment, the loss of specimen weight per unit surface area exposed to the corrosive environment of sea water is calculated using Equation (1) for four operating temperatures and the result of 30 days operation is presented in Figure 5. Here also, the weight loss (g/cm^2) is taken as the copper leached due to overall corrosion effect in contact of sea water for the external shell temperatures of 20℃, 40℃, 60℃, and 80℃, while the sea water is flowing through the copper tube of heat exchanger at a velocity of 1.0 m/s. It is observed that the

weight loss is increased with the increase of operating period, and all the curves have very high slope at the initial attack period with gradual flattening over the long operating period as like that of river water. After 30 days operations, the weight loss curves have no incremental gradient and thus the slopes tend to almost zero. At the same time, weight loss is found to be higher for higher operating temperature over the whole operating period. As such, on completion of one day's operation, weight loss for the operating temperatures of 20℃, 40℃, 60℃, and 80℃ are found to be $1078 \times 10^{-6}\ g/cm^2$, $1247 \times 10^{-6}\ g/cm^2$, $1468 \times 10^{-6} g/cm^2$, and $1519 \times 10^{-6}\ g/cm^2$, respectively, and after 30 days operations, the sample samples have lost $2218 \times 10^{-6}\ g/cm^2$, $2385 \times 10^{-6}\ g/cm^2$, $2580 \times 10^{-6}\ g/cm^2$, and $2835 \times 10^{-6}\ g/cm^2$, respectively. After 30 days' operations, the weight loss values in sea water have been increased by 2.02, 1.91, 1.76, and 1.87 times than those of the first day's operation against the operating temperatures of 20℃, 40℃, 60℃, and 80℃, respectively. For the change in operating temperature from 20℃ to 80℃, weight loss is increased on average by 29.96%. In other words, the average weight loss in sea water is increased by $10.35 \times 10^{-6} g/cm^2/℃$.

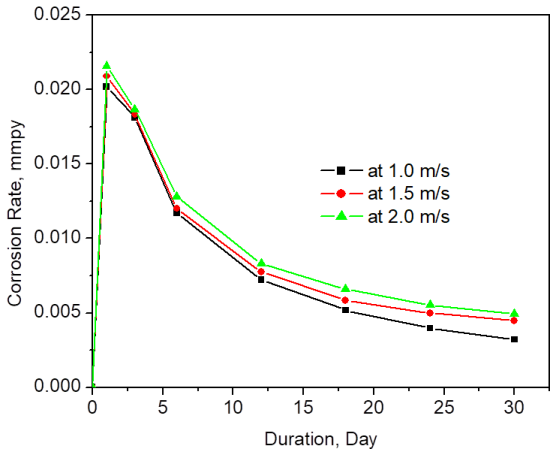

Figure 4: Corrosion rate against corrosion period for the variation of river water flow velocity at the operating temperature of 80℃

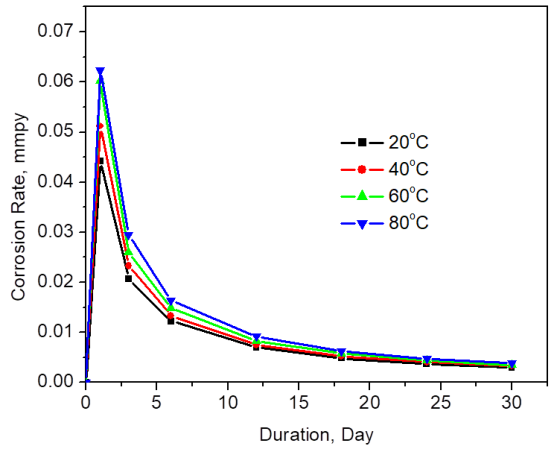

Figure 5: Weight loss per unit exposed surface against operating period for operating temperatures of 20℃, 40℃, 60℃ and 80℃ with the sea water flow velocity of 1.0 m/s

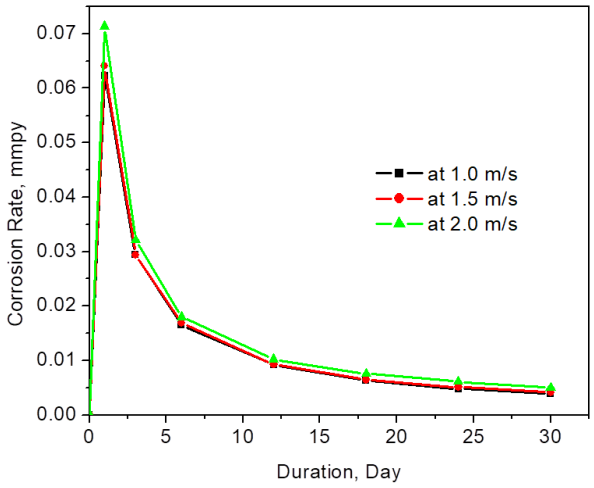

Figure 6: Corrosion rate against corrosion period for the variation of operating temperature with the sea water flow velocity of 1.0 m/s

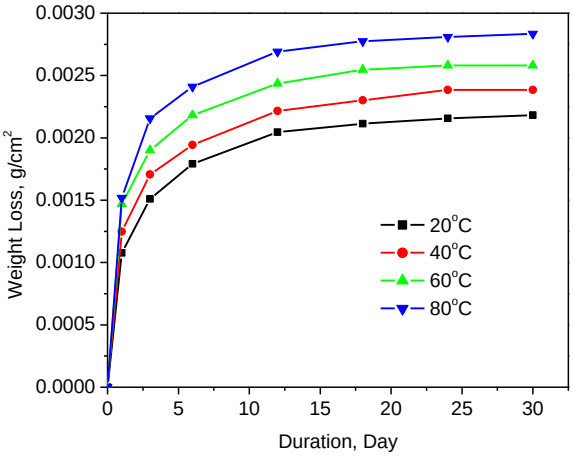

Figure 7: Corrosion rate against corrosion period for the variation of sea water flow velocity at the operating temperature of 80℃

The sea water contains dissolved oxygen of 7.29 $mg/liter$, TDS of 28000 $mg/liter$, TSS of 48 $mg/liter$, and chlorides of 21000 $mg/liter$, and it has conductivity of 48000$\mu S/cm$ as perceived through laboratory tests. Thus, the sea water environment is highly aggressive to make copper susceptible to corrosion with no doubt once some level of corrosion has been observed in river water. In addition, the velocity of sea water through the heat exchanger tube and the temperature of the shell side water are important factors contributing on corrosion as to that of river water. As a result, significant level of weight loss is observed in sea water environment as shown in Figure 5.

Like that of river water, corrosion rates in sea water have been calculated using Equation (2) at the four operating temperatures for different time intervals up to 30 days. Figure 6 elucidates that the corrosion rate is found to be the highest at the initial attack period and then reduced gradually but nonlinearly with the increase of operating period as happened for river water in all operating temperatures. After 30 days of operations, corrosion rates are found to be almost steady showing minimum values. Here, the magnitude of maximum values of corrosion rates

obtained for four operating temperatures are $44.2 \times 10^{-3}\ mmpy$, $51.2 \times 10^{-3}\ mmpy$, $60.2 \times 10^{-3} mmpy$, and $62.3 \times 10^{-3}\ mmpy$, respectively. It indicates that the life span of a copper tube stack in heat exchanger is affected for a considerable period based on corrosion rate.

In the present experiment, the variation of the sea water flow velocity, i.e., $1.0\ m/s$, $1.5\ m/s$, and $2.0\ m/s$, results in change in corrosion rates as shown in Figure 7. The rate of corrosion has been found to be increased in sea water environment with the increase of flow velocity over the whole period of investigation. For the initial attack period, the corrosion rates at sea water for flow velocity of $1.0\ m/s$, $1.5\ m/s$, and $2.0\ m/s$ are found to be $62.3 \times 10^{-3}\ mmpy$, $64.1 \times 10^{-3}\ mmpy$, and $71.4 \times 10^{-3}\ mmpy$, respectively. Therefore, the corrosion rate for the change of flow velocity from $1.0 m/s$ to $2.0 m/s$ is increased by 14.5%, which is significant and has bearing on the operational life of the heat exchanger. Corrosion rate has been affected by velocity variation at sea water condition due to mainly high values of TDS and TSS which cause the erosion corrosion also (Kuźnicka, 2009).

C. Comparative Corrosion in River and Sea Water

The cooling water properties as presented in Table 1 indicate that the pH values and dissolved oxygen are very closer for both river water and sea water, so their contribution would have been nearer on corrosion behavior of copper tube. But the sea water has significantly higher values of TDS ($28000\ mg/liter$), chloride ($21000\ mg/liter$), sulfate ($1320\ mg/liter$) and conductivity ($48000\ \mu S/cm$) than those of the river water, and thus the sea water is more corrosive than the river water.

Figure 8 illustrates the maximum values of corrosion rates in sea water side by side that in river water at the operating temperatures of 20℃, 40℃, 60℃, and 80℃ for flow velocity of $1.0\ m/s$, which indicates that the temperature has considerable effects on the corrosion in both the waters. The corrosion rate is increased with the increase in operating temperature from 20℃ to 40℃, from 40℃ to 60℃, and from 60℃ to 80℃ by 37.02%, 27.02%, and 23.41% respectively for river water. On the other hand, the corrosion rate is increased with the increase in operating temperature from 20℃ to 40℃, from 40℃ to 60℃ and from 60℃ to 80℃ by 15.74%, 17.69%, and 3.47% respectively for sea water. It is noticed that corrosion rates are increasing in both the environment, but there is a big gap in the incremental values in two corresponding environments. Moreover, no linearity in the increment of corrosion rate against temperature is observed. Another point to note that the corrosion rates in sea water are found to be 4.70, 3.97, 3.68, and 3.09, times higher than that of river water for the corresponding operating temperatures of 20℃, 40℃, 60℃, and 80℃, respectively.

Figure 9 demonstrates the maximum values of corrosion rates in sea water side by side that in river water for the flow velocities of $1.0\ m/s$, $1.5\ m/s$, and $2.0\ m/s$ at the operating temperature of 80℃. The corrosion rates in sea water are found to be almost three times higher than that of river water for all three flow velocities, i.e., $1.0\ m/s$, $1.5\ m/s$ and $2.0\ m/s$. However, the corrosion rate is increased with the increase in flow velocity in both the environments. For river water, the corrosion rate is increased for the change of velocity from $1.0\ m/s$ to $1.5\ m/s$ and from $1.5\ m/s$ to $2.0\ m/s$ by 3.5%, and 3.3%, respectively. For sea water environment, the corresponding increments in corrosion rate are 2.8% and 11.4%. Therefore, no linear relation has been observed for velocity variation also.

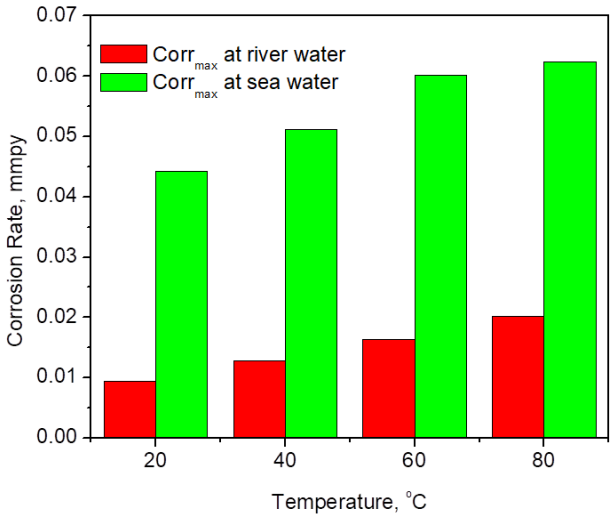

Figure 8: The maximum values of corrosion rate against operating temperatures for river water and sea water with the flow velocity of $1.0\ m/s$

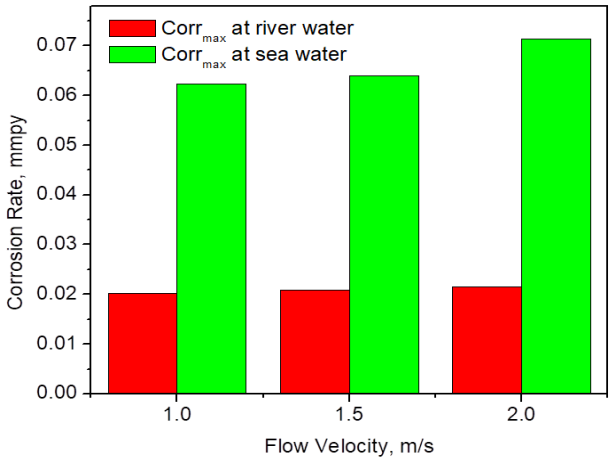

Figure 9: The maximum values of corrosion rate against flow velocity for river water and sea water for the operating temperature of 80℃

D. Microstructural Observation

The microstructures observed through OEM before carrying out the corrosion test without etching, after corrosion test for 30 days in river water and after corrosion test for 30 days in sea water are presented as Figure 10 (a), (b), and (c) respectively. Micrograph shown as Figure 10(a) configures smooth and regular microstructure of copper material. Figure 10(b) depicts sign spots of combined uniform, pitting and erosion corrosion occurred by the river water for the duration of 30 days with the flow velocity of $1.0\ m/s$. On the copper surface, water is bonded to a first layer copper atom by the oxygen electrons. This surface offers easy interaction between the hydrogen atoms of water and the topmost copper atoms

and results in this microstructure. Similarly, Figure 10(c) elucidates huge number of spots indicating different kinds of corrosion that occurred by the sea water for the duration of 30 days with the flow velocity of 1.0 m/s. The chloride ions present in the sea water environment have resulted in breakage of the patina surface layer and aggravated the corrosion (Srivastava & Balasubramaniam, 2005). For the variation of operating temperature and flow velocity, no significant differences have been observed in the microstructures and as such those micrographs have not been shown here.

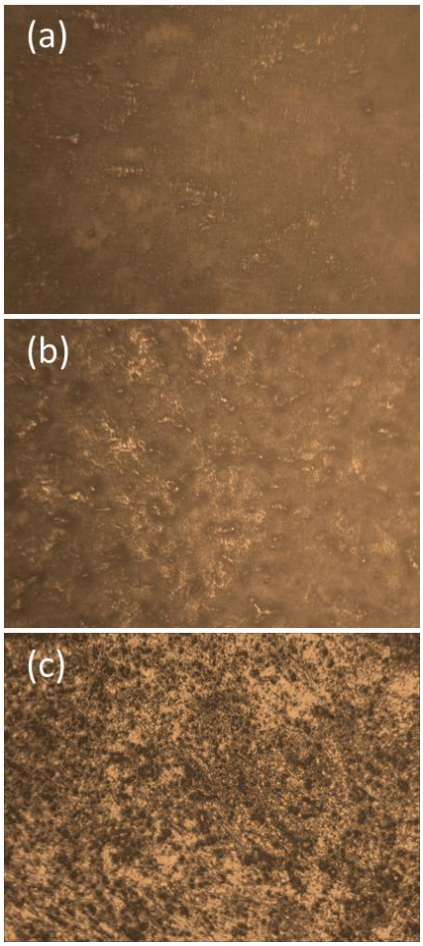

Figure 10: Micrographs with the magnification factor of $320x$: (a) before carrying out the corrosion test without etching, (b) after corrosion test for 30 days in river water, and (c) after corrosion test for 30 days in sea water

E. Life Span Assessment of Heat Exchanger

The life span estimation of a copper tube stack can provide the schedule for major overhauling or renewal requirements of a heat exchanger in line with the overall refit/renovation plan of the vessel based on corrosion rate. In the present study, it is observed that the curves for weight losses as well as corrosion rates become flat after 30 days of operation both in river and sea water. Here, two postulates may be taken into consideration, such as: (i) the flat rate of corrosion obtained after 30 days may continue throughout the lifetime of the heat exchanger, or (ii) the ship's crew may carry out chemical cleaning every after 30 days to avoid bio-fouling or marine growth for maintaining heat transfer coefficient intact or at least within the cooling requirement level. The second option is always preferable to marine engineers, because the engine life is more important than that of heat exchanger based on cost and service values. Accordingly, on completion of the first cycle of the corrosion test, i.e., after 30 days operations, the tubes are cleaned as a part of routine maintenance using standard chemical agents and the corrosion tests are carried out for the second cycle of 30 days. Similarly, another series of tests have been done for the third cycle of 30 days operations.

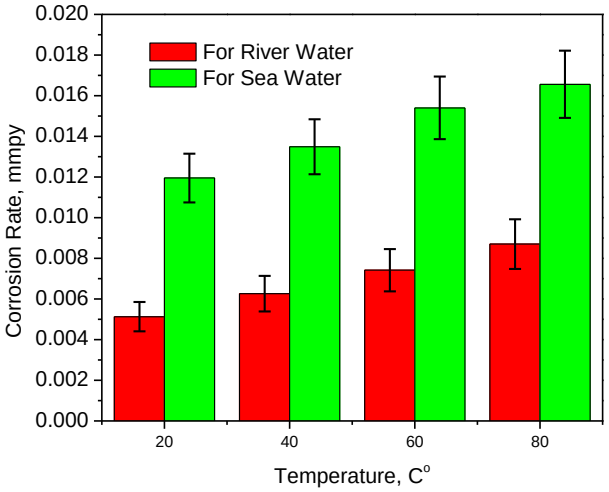

Figure 11: Mean corrosion rates of three operating cycles along with error level against operating temperatures for river and sea water with the flow velocity of 2.0 m/s

The life span of tube stack is then assessed with the combined experimental results of three corrosion cycles. The mean corrosion rates of the three cycles for four operating temperatures are presented in Figure 11. Out of mean corrosion rates for four operating temperatures, the highest mean value is obtained for 80℃, i.e., 8.7×10^{-3} $mmpy$ with an error level of 6% for river water and 16.6×10^{-3} $mmpy$ with an error level of 5% for sea water. Since the vessel needs to travel nearly one-fourth in the river and three-fourth at sea route, the life span is calculated taking corrosion rates of river and sea water with the weightage values $1:3$ and incorporating the allowance for error level. By this way, the life span is found to be 24 years considering the uniform loss of thickness, but practically it does not happen, because the failure of heat exchanger tube normally originates at the pitting location. Therefore, considering the pitting susceptibility allowance of $> 15\%$, the estimated life span comes down to 20 years which is reasonable with the designed life of the ship.

4. CONCLUSIONS

This work presents a comprehensive experimental analysis of locally manufactured marine engineering item such as, shell and tube type heat exchanger for its life span assessment based on corrosion behavior. Based on the results obtained in the present work, the notable findings can be summarized as follows:

i. Copper tube of heat exchanger corroded both in river water and sea water environments. The rate of corrosion was higher at the beginning of heat exchanger operation for both the environments.

ii. Corrosion on copper tube in sea water environment was about three times higher than that of river water environment due to water chemistry including dissolved oxygen, TDS, TSS, chloride, conductivity, etc.

iii. Corrosion increased with the increase of operating temperature, but no linear relation was obtained. However, the average weight loss gradient was found to be $6.98 \times 10^{-6}\ g/cm^2/℃$ in river water while in sea water it was $10.35 \times 10^{-6}\ g/cm^2/℃$.

iv. The effect of velocity was observed for both environments, and the corrosion rates were found to be increased by 6.8% in river water and 14.5% in sea water with the change of velocity from $1.0\ m/s$ to $2\ m/s$.

v. The life span of copper tube (18 BWG) of heat exchanger was estimated to be 20 years with the three-fourth period of operations at sea and the one-fourth at river water, which was proportionate to the designed life of ship.

ACKNOWLEDGEMENTS

Authors profoundly acknowledge the financial support of MIST, material and equipment support of KSY Ltd and laboratory support of BUET as well as MIST to conduct this research.

REFERENCES

Abdallah, M. M. A., Maayta, A.K., Qudah, M.A. A. & Rawashdeh, N.A.F. A. (2009). Corrosion Behavior of Copper in Chloride Media, *The Open Corrosion Journal*, 2, 71-76. doi:10.1016/j.matdes.2008.10.015

Baboian, R. (2005). Corrosion Tests and Standards - Application and Interpretation. *ASTM International*, Philadelphia, USA

Collini, L. (2012). Copper Alloys – Early Applications and Current Performance – Enhancing Processes. *InTech Janeza Trdine 9*, 51000 Rijeka, Croatia.

Cramer, S.D. & Covino, B.S. (2005). *Corrosion: Materials. ASM Handbook*, Volume 13B, ASM International. Materials Park, Ohio 44073-0002 USA.

Davis, J. R. (2001). *Copper and Copper Alloys. ASM Specialty Handbook*, ASM International, Materials Park, Ohio 44073-0002, USA.

Farro, N. W., Veleva, L. and Aguilar, P. (2009). Copper Marine Corrosion: I. *Corrosion Rates in Atmospheric and Seawater Environments of Peruvian Port, The Open Corrosion Journal*, 2, 114-122.

Francis, R. (2010). *Corrosion of Copper and its Alloys - A Practical Guide for Engineers*. NACE International, 1440 South Creek Drive, Houston, Texas, USA.

Gerasimov, V. V., & Rozenfeld, I. L. (1958). Effect of temperature on the rate of corrosion of metals. *Bulletin of the Academy of Sciences of the USSR Division of Chemical Science*, 6(10), 1192–1197. doi:10.1007/bf01167386

Graedel, T. E., Nassau, K. & Franey, J. P. (1987). Copper patinas formed in the atmosphere—I. *Introduction, Corrosion Science*, 27(7), 639–657. doi:10.1016/0010-938x(87) 90047-3

Gudas, J. P., & Hack, H. P. (1979). Parametric Evaluation of Susceptibility of Cu-Ni Alloys to Sulfide Induced Corrosion in Sea Water. *Corrosion*, 35(6), 259–264. doi:10.5006/0010-9312-35.6.259

Hedin, A., Johansson, A. J., Lilja, C., Boman, M., Berastegui, P., Berger, R., & Ottosson, M. (2018). Corrosion of copper in pure O 2 -free water? *Corrosion Science*, 137, 1–12. doi:10.1016/j.corsci.2018.02.008

Hultquist, G., Szakálos, P., Graham, M. J., Belonoshko, A. B., Sproule, G. I., Gråsjö, L., … Rosengren, A. (2009). Water Corrodes Copper. Springer, *Catalysis Letters*, 132(3-4), 311–316. doi:10.1007/s10562-009-0113-x

Hultquist, G., Graham, M. J., Szakalos, P., Sproule, G. I., Rosengren, A., & Gråsjö, L. (2011). Hydrogen gas production during corrosion of copper by water. *Elsevier, Corrosion Science*, 53(1), 310–319. doi:10.1016/j.corsci. 2010.09.037

Hultquist, G. (2015). Why copper may be able to corrode in pure water. *Corrosion Science*, 93, 327–329. doi:10.1016/ j.corsci.2015.01.002

Hultquist, G., Graham, M. J., Kodra, O., Moisa, S., Liu, R., Bexell, U., & Smialek, J. L. (2015). Corrosion of copper in distilled water without O_2 and the detection of produced hydrogen. *Corrosion Science*, 95, 162–167. doi:10.1016/j.corsci. 2015.03.009

Imai, M., Yamashita, Y., Futatsuki, T., Shiohara, M., Kondo, S., & Saito, S. (2009). Effect of Dissolved Oxygen on Cu Corrosion in Single Wafer Cleaning Process. *Japanese Journal of Applied Physics*, 48(4), 04C023. doi:10.1143/jjap. 48.04c023

Kong, D., Dong, C., Xiao, K., & Li, X. (2017). Effect of temperature on copper corrosion in high-level nuclear waste environment. *Transactions of Nonferrous Metals Society of China*, 27(6), 1431–1438. doi:10.1016/s1003-6326(17) 60165-1

Kristiansen, H. (1977). Corrosion of Copper by Water of Various Temperatures and carbon dioxide contents. *Materials and Corrosion/Werkstoffe Und Korrosion*, 28(11), 743–748. doi:10.1002/maco.19770281102

Kuźnicka, B. (2009). Erosion–corrosion of heat exchanger tubes. *Engineering Failure Analysis*, 16(7), 2382–2387. doi:10.1016/j.engfailanal.2009.03.026

Lee, S. K., Hsu, H. C., & Tuan, W. H. (2016). Oxidation Behavior of Copper at a Temperature below 300 °C and the Methodology for Passivation. *Materials Research*, 19(1), 51–56. doi:10.1590/1980-5373-mr-2015-0139

Leygraf, C., Chang, T., Herting, G., & Odnevall Wallinder, I. (2019). The Origin and Evolution of Copper Patina Colou. *Corrosion Science*. doi:10.1016/j.corsci.2019.05.025

Melchers, R. E. (2001). Temperature Effect on Seawater Immersion Corrosion of 90:10 Copper-Nickel Alloy. *CORROSION*, 57(5), 440–451. doi:10.5006/1.3290368

Miller, R. L., Bradford, W. L., & Peters, N. E. (1988). Specific Conductance: Theoretical Considerations and Application to Analytical Quality Control. In U.S. Geological Survey Water-Supply Paper. Retrieved from http://pubs.usgs.gov/ wsp/2311/report.pdf

Mor, E. D., & Beccaria, A. M. (1979). Effects of temperature on the corrosion of copper in sea water at different hydrostatic pressures. *Congresso Nazionale della Societi, Werkstoffe und Korrosion*, 30, 551-558.

Nunez, L., Reguera, E., Corvo, F., Gonzalez, E. and Vazquez, C. (2005). Corrosion of copper in sea water and its aerosols in a tropical island. *Elsevier, Corrosion Science*, 47, 461–484. doi:10.1016/j.corsci.2004.05.015

Orozco-Cruz, R., Ávila, E., Mejía, E., Pérez, T., Contreras, A. and Martínez, R. G. (2017). In situ Corrosion Study of Copper and Copper-Alloys Exposed to Natural Seawater of the Veracruz Port (Gulf of Mexico). *Int. J. of Electrochemical Science*, 12, 3133 – 3152.

Pehkonen, S. O., Palit, A., & Zhang, X. (2002). Effect of Specific Water Quality Parameters on Copper Corrosion. *CORROSION*, 58(2), 156–165. doi:10.5006/1.3277316

Poulson, B. (1993). Advances in understanding hydrodynamic effects on corrosion. *Corrosion Science*, 35(1-4), 655–

665. doi:10.1016/0010-938x(93)90201-q

Rahman, M. M. (2017). An Appraisal of Shipbuilding Prospects in Bangladesh. Elsevier, *Procedia Engineering*, 194, 224 – 231. doi: 10.1016/j.proeng.2017.08.139

Rahmanto, W. H., Gunawan and Nuryanto, R. (2002). Corrosion rate of copper and iron in seawater based on resistance measurement. *Journal of Coastal Development*, 5(2), 67-74.

Roy, S., Coyne, J. M., Novak, J. A., and Edwards, M. A. (2018). Flow-induced failure mechanisms of copper pipe in potable water systems. *Corrosion Reviews*, 36(5), 449–481. DOI: https://doi.org/10.1515/corrrev-2017-0120

Sabri, M. A. M., Sulong, A. B., Chin, F. K. & Sahari, J. (2012). Effect of Corrosion on the Electrical Conductivity of Metals and Polymer Composite, *Jurnal Teknologi (Sciences & Engineering)* 59, Suppl 2, 81–85.

Schumacher, M. (1979). *Seawater corrosion handbook*. Noyes Data Corp., Park Ridge, N. J., USA

Simpson, J. P., & Schenk, R. (1987). Hydrogen evolution from corrosion of pure copper. *Corrosion Science*, 27(12), 1365–1370. doi:10.1016/0010-938x(87)90131-4

Srivastava, A., & Balasubramaniam, R. (2005). Microstructural characterization of copper corrosion in aqueous and soil environments. *Materials Characterization*, 55(2), 127–135. doi:10.1016/j.matchar.2005.04.004

Szakálos, P., Hultquist, G., & Wikmark, G. (2007). Corrosion of Copper by Water. *Electrochemical and Solid-State Letters*, 10(11), C63. doi:10.1149/1.2772085

Utanohara, Y., & Murase, M. (2019). Influence of flow velocity and temperature on flow accelerated corrosion rate at an elbow pipe. *Nuclear Engineering and Design*, 342, 20–28. doi:10.1016/j.nucengdes.2018.11.022

Wan, Y., Wang, X., Sun, H., Li, Y., Zhang, K. and Wu, Y. (2012). Corrosion Behavior of Copper at Elevated Temperature, *Int. J. Electrochem. Sci*., 7, 7902 – 7914.

Yatsenko, E. A., Zubekhin, A. P., & Nepomnyashchev, A. A. (1999). Protection of copper against high-temperature corrosion. *Glass and Ceramics*, 56(9-10), 295–297. doi:10.1007/bf02681380

Zakowski, K., Narozny, M., Szocinski, M., & Darowicki, K. (2014). Influence of water salinity on corrosion risk—the case of the southern Baltic Sea coast. *Environmental Monitoring and Assessment*, 186(8), 4871–4879. doi:10.1007/s10661-014-3744-3

MIJST
MIST International Journal of Science and Technology

Mathematical Modelling of Vehicle Drifting

Reza N. Jazar[1*], Firoz Alam[2], Sina Milani[3], Hormoz Marzbani[4], and Harun Chowdhury[5]

School of Engineering, RMIT University, Melbourne, Australia

emails: *[1]reza.nakahiejazar@rmit.edu.au; [2]firoz.alam@rmit.edu.au; [3]sina.alamdarimilani@rmit.edu.au; [4]hormoz.marzbani@rmit.edu.au, and [5]harun.chowdhury@rmit.edu.au

ARTICLE INFO

Article History:

Received: 15th April 2020
Revised: 13th June 2020
Accepted: 21st August 2020
Published: 16th December 2020

Keywords:

Vehicle Dynamics
Vehicle Drifting
Vehicle Stability

ABSTRACT

A mathematical model and condition for drifting of vehicles are presented in this paper. Employing the condition for possible steady-state drifting, the mathematical model of a vehicle with lateral weight lift during turning and drifting as well as adopting a combined tyre force model enables to reduce the number of equations of motion to a set of nonlinear coupled algebraic equations. The solution of the equations are the longitudinal and lateral components of the velocity vector of the vehicle at its mass centre and the vehicle's yaw rate. The numerical values of the variables are associated with an equilibrium at which the vehicle drifts steadily. The equilibrium point should be analysed for stability by examining for any small disturbance should disappear. The procedure applied to a nominal vehicle indicates that an equilibrium point exists for every given value of the steering angle as the input. Also, it is shown that the equilibrium point is unstable. Hence, to keep the vehicle at the associated steady-state drifting, the value of the yaw rate must be kept constant.

1. INTRODUCTION

Race-car drivers wish to keep the speed as high as possible in corners. Such a manoeuvre may go into drift when the vehicle slides laterally on the road. Drift may also be controlled intentionally when the inwards and outwards motion of the vehicle are balanced while the vehicle is moving the desired path. Generally, race cars are made to be rear-wheel-drive to improve their acceleration performance. Considering tyre force dynamics, increased longitudinal slip at rear tyres will cause a drop of lateral force and makes a larger side-slip angle at the rear wheels (Jazar, 2019). Therefore, the driver needs to adjust the steering and torque input to the vehicle to keep the vehicle on track. To prevent the vehicle from spinning, steering the vehicle opposite to turning direction may also be needed to keep the vehicle on track. The sensitivity of motion of such vehicles to inputs is high (Milani *et al*., 2019, Voser *et al*., 2010).

Steady-state drifting is an unstable manoeuvre and hard to explain mathematically. The topic has been under investigation by several researchers, (Bobier-Tiu *et al*., 2019). Edelmann and Plöchl (2009) showed that the equilibrium point corresponding to the drifting of a four-wheel vehicle is unstable by linearizing the equations around the equilibrium point. Velenis, Frazzoli, and Tsiotras (2010) analysed a vehicle bicycle model by considering longitudinal load transfer and employing the magic formula tyre model. They applied a control scheme to stabilize the equilibrium point by adjusting steering and torque inputs. Velenis *et al*. (2011) proposed an LQR control to adjust the steering angle and rear wheels' angular velocity to keep their vehicle model drifting. An iterative method has also been used by Chaichaowarat and Wannasuphoprasit to derive steady-state drifting of a bicycle model (Chaichaowarat & Wannasuphoprasit, 2013). There are also several attempts to apply different control strategies to keep steady-state drifting on bicycle models (Hindiyeh & Gerdes, 2009, Voser, Hindiyeh, & Gerdes, 2010, Hindiyeh & Gerdes, 2014). Figure 1 illustrates a bicycle vehicle model at steady state drifting.

In this paper, a mathematical model for identifying drifting manoeuvres in steady-state condition and controlling the vehicle at those conditions are presented. Several criteria have been developed to evaluate drifting manoeuvres (Abdulrahim, 2006). Quantitative methods have also been introduced by measuring vehicle body side-slip angle at its mass centre (Abdulrahim 2006, Hindiyeh & Gerdes, 2014). Defining drifting has also been done as a large sideslip manoeuvres in steady state (Edelmann & Plöchl, 2009, Velenis, Frazzoli, & Tsiotras, 2010). Manoeuvres with large sideslip, counter-steering, and saturation of lateral tyre forces at the rear are also identified as drifting (Hindiyeh & Gerdes, 2009). Drifting may also happen

unfavourably at high speeds when a driver expects to negotiate the vehicle turning in a certain direction, but the vehicle will not follow the driver's command when tyres are at large slips. Drifting is usually manoeuvring with side-slip angles over the limit and opposite steering, (Tavernini *et al*., 2013, Shi *et al*., 2017). This study develops a kinematic condition for feasible counter steering as a mathematical expression to include kinematic vehicle variables. A general definition that is not only applied to a specific instant of driving but also accounts for all principal forces and moments during the manoeuvre. The vehicle will turn about the centre of rotation with a smaller radius during drifting generating large centripetal acceleration. The resultant difference in the longitudinal force of left and right driving wheels generates a yaw moment about the mass centre of the vehicle that will be turning the vehicle, (Hindiyeh & Gerdes, 2009, Voser, Hindiyeh, & Gerdes, 2010, Hindiyeh & Gerdes, 2014).

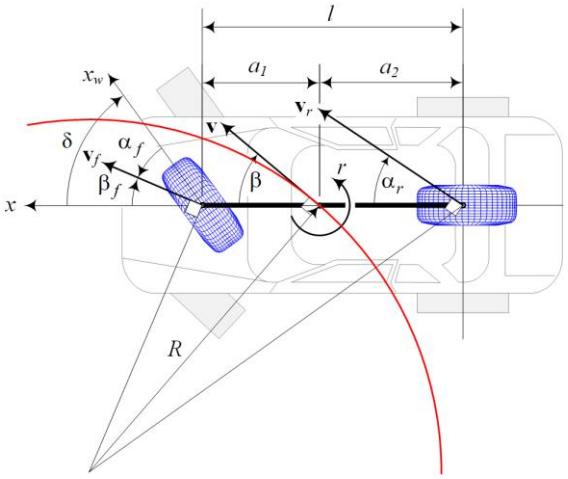

Figure 1: A two-wheel vehicle model at steady state drifting

To analyse drifting manoeuvres, the suitability of the vehicle model is of importance while the level of simplifications must be kept reasonable such that the model captures the key dynamic behaviours of the vehicle during drifting. We use a rear-wheel-drive vehicle and assume no positive or negative longitudinal force is present at the front tyres. Therefore, we may integrate front wheels into a single wheel without losing accuracy. However, we keep the rear wheels separate to include weight transfer during turning. Figure 2 illustrates such a mathematical model.

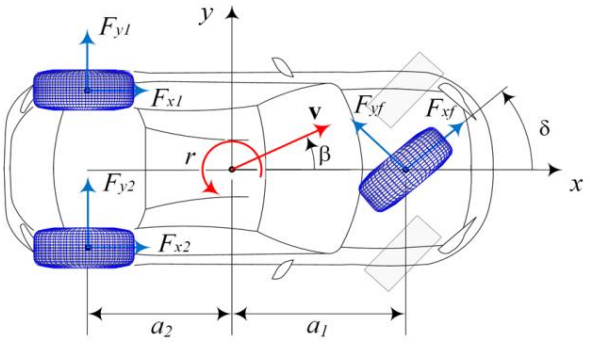

Figure 2: Three-Wheel Vehicle Model

2. MATHEMATICAL VEHICLE MODEL

The general forms of equations of motion for a rigid body in planar motion in body coordinate are (Jazar, 2019):

$$\Sigma F_x = m\dot{v}_x - mrv_y \tag{1}$$

$$\Sigma F_y = m\dot{v}_y + mrv_x \tag{2}$$

$$\Sigma M_z = I_z\dot{r} \tag{3}$$

where, v_x, v_y, and r are longitudinal, lateral, and yaw velocities of the mass centre, respectively. As shown in Figure 2, the total longitudinal and lateral forces may be summarized as:

$$\Sigma F_x = F_{x1} + F_{x2} + F_{xf}\cos\delta - F_{yf}\sin\delta$$
$$= F_{xr} + F_{xf}\cos\delta - F_{yf}\sin\delta \tag{4}$$

$$\Sigma F_y = F_{y1} + F_{y2} + F_{yf}\cos\delta + F_{xf}\sin\delta$$
$$= F_{yr} + F_{yf}\cos\delta + F_{xf}\sin\delta \tag{5}$$

$$\Sigma M_z = \begin{matrix}(F_{yf}\cos\delta + F_{xf}\sin\delta)a_1 - (F_{y1} + F_{y2})a_2 \\ +(F_{x2} - F_{x1})\frac{w}{2}\end{matrix}$$

$$= (F_{yf}\cos\delta + F_{xf}\sin\delta)a_1 - F_{yr}a_2 + \Delta F_{xr}\frac{w}{2} \tag{6}$$

Steer angle δ and side-slip angle β are indicated in the figure, dimensions a_1 and a_2 are distances of the front and rear axles from vehicle mass centre, respectively, and w shows the rear track width. We adopt the combined elliptical tyre forces (Jazar, 2019). The longitudinal and lateral tyre forces are:

$$F_x = F_z C_s S(s - s_s)\sqrt{1 - C_{s\alpha}\left(\frac{S(\alpha-\alpha_s)}{\alpha_s}\right)^2} \tag{7}$$

$$F_y = -F_z C_\alpha S(\alpha - \alpha_s)\sqrt{1 - C_{\alpha s}\left(\frac{S(s-s_s)}{s_s}\right)^2} \tag{8}$$

Parameters C_s and C_α are the longitudinal and lateral tyre stiffnesses, while $C_{s\alpha}$ and $C_{\alpha s}$ are longitudinal and lateral drop factors, and function S is the saturation function which limits the magnitude of the input variable to a maximum. Parameters s_s and α_s are the saturation slip values at which the tyre forces are assumed to be saturated when the slip value reaches these certain limits. The combined tyre force indicates that the introduction of a secondary slip causes a drop in the current tyre force until both slips are saturated.

The lateral load transfer at the rear of the car is estimated as follows (Jazar, 2019):

$$\Delta F_{zr} = F_{z2} - F_{z1} = F_{zr}\frac{2h(\dot{v}_y + v_x r)}{wg}$$
$$= m\left(\frac{a_1 g}{a_1+a_2} + \frac{h(\dot{v}_x - rv_y)}{a_1+a_2}\right).\frac{2h(\dot{v}_y + v_x r)}{wg} \tag{9}$$

While vertical loads under the front and rear axles are being estimated by the following equations (Jazar, 2019):

$$F_{zf} = m\left(\frac{a_2 g}{a_1+a_2} - \frac{h(\dot{v}_x - rv_y)}{a_1+a_2}\right) \tag{10}$$

$$F_{zr} = m\left(\frac{a_2 g}{a_1+a_2} + \frac{h(\dot{v}_x - rv_y)}{a_1+a_2}\right) \tag{11}$$

where h is the mass centre height of the vehicle from the ground.

3. MATHEMATICAL DEFINITION OF DRIFTING

We begin by assuming a steady-state drifting manoeuvre to come up with a kinematic condition for the drifting vehicle. At the assumed steady-state turning condition, the equation of motion in yaw for the three-wheel planar vehicle in steady-state must be:

$$\Sigma M_z = 0 \tag{12}$$

A large torque at rear wheels reduces lateral tyre force at the rear and creates a combined-slip condition. The rear tyres will spin at this condition as the longitudinal slip saturates while large tyre side-slip angles happen, and tyres will be side-slip saturate. Hence, it is assumed both rear tyres are laterally and longitudinally saturated. The total lateral tyre force at the rear will then be:

$$F_{yr} = \sqrt{1 - C_{\alpha s}}\,\mu_y F_{zr} \tag{13}$$

Combining (13) and (12) and ignoring derivative terms at steady state makes the yaw moment equation become:

$$\Sigma M_z = F_{yf} a_1 - \sqrt{1 - C_{\alpha s}}\,\mu_y F_{zr} a_2 + \frac{h\mu_x v_x r}{g} F_{zr} = 0 \tag{14}$$

The equation is solved for F_{yf} and substitute a nominal range of vehicle's parameters, to conclude that the total lateral force at the front must be positive to satisfy the yaw motion in equilibrium:

$$F_{yf} = F_{zr}\frac{\sqrt{1-C_{\alpha s}}\mu_y a_2 - h\mu_x v_x r/g}{a_1} \tag{15}$$

$$g = 9.81\text{m/s}^2, \quad C_{\alpha s} \approx 0.5, \quad \mu_x \approx \mu_y \approx 0.75,$$

$$a_2 > 1m, \quad h < 1m, \quad v_x r < 0.5g$$

$$F_{yf} > 0.15\frac{F_{zr}}{a_1} > 0 \tag{16}$$

Having a positive lateral force at the front tyre makes the tyre side-slip angle in a left-hand turn to be negative. The side-slip angle of the vehicle body at centre of the front wheel is shown by β_f, tyre side-slip angle by α_f, and the steering angle by δ and they are related by (Jazar, 2019):

$$\alpha_f = \beta_f - \delta = arctan\frac{v_{yf}}{v_{xf}} - \delta \tag{17}$$

$$\beta_f - \delta < 0 \rightarrow \beta_f < \delta \tag{18}$$

In case of a negative steer angle to cause left-hand turning of the vehicle:

$$\beta_f < \delta < 0 \tag{19}$$

$$r > 0 \tag{20}$$

Employing (19) and (20), the kinematic condition for drifting may now be defined as:

$$r\beta_f < 0 \tag{21}$$

Therefore, it is proposed that whenever the yaw velocity and body side-slip angle at the front wheel have opposite signs, the vehicle is drifting. The condition also provides us with an equation to associate a value to the instantaneous drifting at any time. Such value suggests that a drift meter can be introduced, and the future vehicle can be equipped with a warning system to inform the driver when the vehicle is approaching a drifting condition. To evaluate a manoeuvre in terms of drifting, we integrate the expression over time of the manoeuvre.

4. PHASE PLANE ANALYSIS AND DRIFTING EQUILIBRIUM POINT

As assumed, the steady-state condition for drifting must be associated with an equilibrium condition and it might be shown geometrically in suitable state space. To investigate this phenomenon, the time derivative terms are removed as the state of the system should not change at the equilibrium point. Therefore, the equations of motion in equilibrium will be:

$$\Sigma F_x = -mrv_y \tag{22}$$

$$\Sigma F_y = mrv_x \tag{23}$$

$$\Sigma M_z = 0 \tag{24}$$

Substituting the tyre force model (7) and (8), total longitudinal and lateral forces will be written as:

$$\Sigma F_x = \sqrt{1 - C_{s\alpha}}\ \mu_x m\left(\frac{a_1 g}{a_1+a_2} - \frac{hrv_y}{a_1+a_2}\right)$$
$$+m\left(\frac{a_2 g}{a_1+a_2} + \frac{hrv_y}{a_1+a_2}\right)C_{\alpha f}\left[arctan\left(\frac{a_1 r+v_y}{v_x}\right) - \delta\right]sin\,\delta \tag{25}$$

$$\Sigma F_y = \sqrt{1 - C_{\alpha s}}\ \mu_y m\left(\frac{a_1 g}{a_1+a_2} - \frac{hrv_y}{a_1+a_2}\right)$$
$$-m\left(\frac{a_2 g}{a_1+a_2} + \frac{hrv_y}{a_1+a_2}\right)C_{\alpha f}\left[arctan\left(\frac{ra_1+v_y}{v_x}\right) - \delta\right]cos\,\delta \tag{26}$$

$$\Sigma M_z = \frac{hm\ \mu_x v_x r\left(\frac{a_1 g}{a_1+a_2} - \frac{hrv_y}{a_1+a_2}\right)}{g}$$
$$-\sqrt{1 - C_{\alpha s}}\ \mu_y m\left(\frac{a_1 g}{a_1+a_2} - \frac{hrv_y}{a_1+a_2}\right)a_2$$
$$-m\left(\frac{a_2 g}{a_1+a_2} + \frac{hrv_y}{a_1+a_2}\right)C_{\alpha f}\left[arctan\left(\frac{ra_1+v_y}{v_x}\right) - \delta\right]cos\,\delta\,a_1 \tag{27}$$

Substituting these force systems in equations of motion leads us to a set of algebraic equations to be solved for the vehicle velocity components v_x, v_y and r for a given value of steer angle as input. There is no closed-form solution for the set of equations and hence, they must be solved numerically for given nominal vehicle parameters to determine the expected equilibrium points. The nominal values are shown in Table 1 (Milani *et al.*, 2019).

Solving Equations (25)-(27) for the velocities the values of v_x, v_y and r is found when the vehicle is drifting steadily for given values of steer angle. The values shown in Table 2 are the solutions of the equations.

Table 1
Nominal values of vehicle parameters

m	h	$a1$	$a2$
1600 kg	0.9 m	1.35 m	1.5 m
Cs	$C\alpha$	$Cs\alpha$	$C\alpha s$
7.5	8.5	0.5	0.5
w	Iz	Rw	Iw
1.58 m	2000 $kg.m2$	0.35 m	1 $kg.m2$
ss	αs	μx	μy
0.1	0.09 $[rad]$	0.75	0.75

Table 2
Values of v_x, v_y, r and δ when the vehicle is drifted steadily for given values of steer angle

$r\ (rad/s)$	$vx\ (m/s)$	$vy\ (m/s)$	$\delta\ (rad)$
0.844756776	6.080326946	−5.027221269	−0.5
1.023066746	4.960105873	−3.860670023	−0.4
1.152547811	4.353764384	−3.192852462	−0.3
1.254922383	3.956398895	−2.73254504	−0.2
1.340414747	3.666314032	−2.380578459	−0.1
1.414736369	3.438840107	−2.092329884	0

To examine the stability of the equilibrium points, the set of equations of motion around each equilibrium point may be linearized and the associated eigenvalues are calculated as

$$\dot{v}_x = \frac{\partial f_1(v_x,v_y,r)}{\partial v_x} v_x + \frac{\partial f_1(v_x,v_y,r)}{\partial v_y} v_y + \frac{\partial f_1(v_x,v_y,r)}{\partial r} r + g_1(\delta) \quad (28)$$

$$\dot{v}_y = \frac{\partial f_2(v_x,v_y,r)}{\partial v_x} v_x + \frac{\partial f_2(v_x,v_y,r)}{\partial v_y} v_y + \frac{\partial f_2(v_x,v_y,r)}{\partial r} r + g_2(\delta) \quad (29)$$

$$\dot{r} = \frac{\partial f_3(v_x,v_y,r)}{\partial v_x} v_x + \frac{\partial f_3(v_x,v_y,r)}{\partial v_y} v_y + \frac{\partial f_3(v_x,v_y,r)}{\partial r} r + g_3(\delta) \quad (30)$$

The linearized equations for $\delta = -0.5\ rad$, and their associated eigenvalues will be:

$$\begin{bmatrix}\dot{v}_x\\ \dot{v}_y\\ \dot{r}\end{bmatrix} = [A]_{3\times3}\begin{bmatrix}v_x\\ v_y\\ r\end{bmatrix} + \begin{bmatrix}g_1(\delta)\\ g_2(\delta)\\ g_3(\delta)\end{bmatrix} = \begin{bmatrix}-1859.94 & -1664.73 & -11336.35\\ -4756.21 & -5333.39 & -16874.67\\ -2.02 & -2.02 & -4.29\end{bmatrix}\begin{bmatrix}v_x\\ v_y\\ r\end{bmatrix} + \begin{bmatrix}g_1(\delta)\\ g_2(\delta)\\ g_3(\delta)\end{bmatrix} \quad (31)$$

$$\text{eig}([A]) = \begin{bmatrix}-6911.51\\ -291.71\\ 5.59\end{bmatrix} \quad (32)$$

In this case, two of the three eigenvalues have negative real parts indicating stability with respect to two of the system variables. However, one eigenvalue has a positive real part indicating instability of the linear system with respect to one of the variables. Figure 3 shows the phase portrait of the system variables. The phase portraits show that the equilibrium point is stable in the large for v_x, v_y when r is kept constant, but unstable when r varies. Therefore, keeping yaw velocity constant by means of a feedback control, the equilibrium drifting point is stable, and it can be expected a steady-state drifting motion as is shown in Figures 4 and 5.

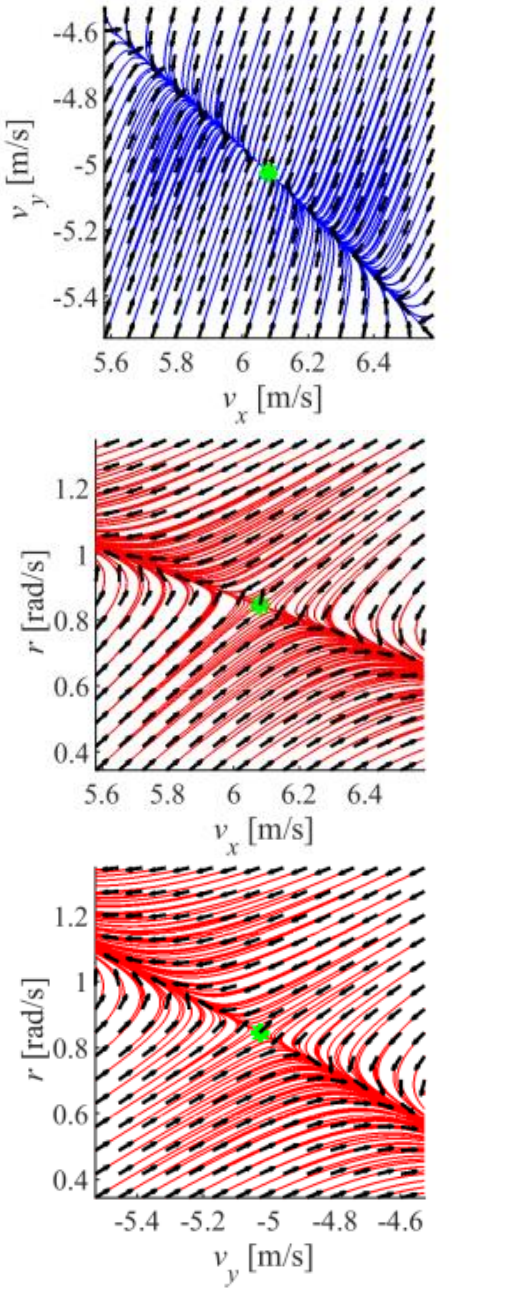

Figure 3: Phase Portraits of the Three-Wheel Model at Equilibrium Point

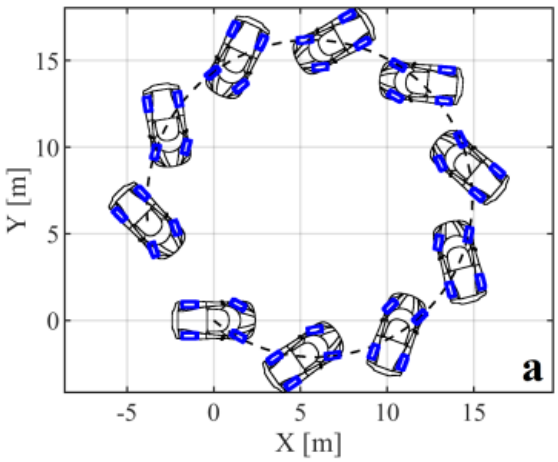

Figure 4: Steady-state drifting condition of a nominated vehicle

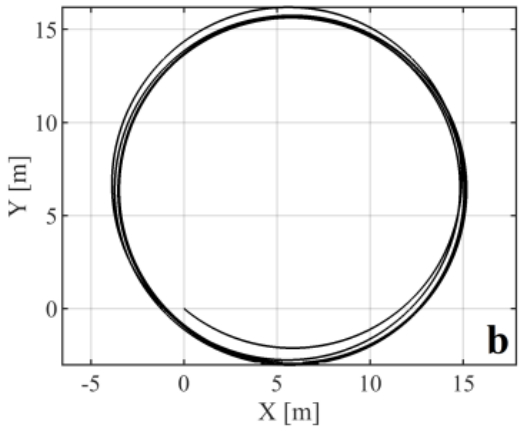

Figure 5: Nominated vehicle's path in the global coordinate frame

5. CONCLUSIONS

This paper introduces a condition for steady-state drifting condition of the vehicle by investigating equilibrium points of the equations of motion of vehicles. The lateral and longitudinal load transfer has been included. The tyre model also was capable to consider the combined slips as well as combined saturation of tyre forces. The equations of motion at steady state condition have been reduced to a set of nonlinear coupled algebraic equations with longitudinal and lateral velocities, and yaw rate as unknown. The equations may be loaded by parameters of any given vehicle to be solved for the unknowns at a given steer angle input. If there is any solution for the variables, then they will indicate equilibrium points of drifting. The stability analysis by employing the eigenvalue method of the linearized equations around the equilibrium point determines the stability of the equilibrium point. A sample example for a set of nominated numerical values as a fixed steer angle indicated the existence of an equilibrium point suggesting the existence of steady-state drifting. Stability analysis of the equilibrium point suggest that it is possible to keep the vehicle at a steady-state drifting condition when keeping the value of the yaw rate constant by means of a control system.

ACKNOWLEDGEMENTS

Authors would like to express their gratitude to the School of Engineering, RMIT University, Melbourne, Australia. They also would like to present their appreciation to the Editors and anonymous reviewers of MIJST for the insightful inputs to improve the manuscript.

REFERENCES

Abdulrahim, M. (2006). On the dynamics of automobile drifting. *Technical Paper 2006-01-1019, SAE 2006 World Congress & Exhibition*, https://doi.org/10.4271/2006-01-1019

Bobier-Tiu, C. G., Beal, C. E., Kegelman, J. C., Hindiyeh, R. Y., & Gerdes, J. C. (2019). Vehicle control synthesis using phase portraits of planar dynamics, *Vehicle System Dynamics*, 57(9), 1318-1337

Edelmann, J., & Plöchl, M. (2009). Handling characteristics and stability of the steady-state powerslide motion of an automobile. *Regular and Chaotic Dynamics*, 14(6), 682, https://doi.org/10.1134/S1560354709060069

Hindiyeh, R. Y., & Gerdes, J. C. (2009). Equilibrium analysis of drifting vehicles for control design. *ASME 2009 Dynamic Systems and Control Conference*. DSCC2009-2626: 181-188, https://doi.org/10.1115/DSCC2009-2626

Hindiyeh, R. Y., & Gerdes, J. C. (2014). A controller framework for autonomous drifting: Design, stability, and experimental validation. *Journal of Dynamic Systems, Measurement, and Control*, 136(5), DS-12-1023: 051015. https://doi.org/10.1115/1.4027471

Jazar, R. N. (2019). *Advanced vehicle dynamics*, Springer, New York

Milani, S., Marzbani, H., & Jazar, R. N. (2019). *Vehicle Drifting: Mathematical Theory and Dynamic Analysis*, *5th Recent Advances in Automotive Engineering* (ReCAR 2019), Mechanical Engineering Multi-Conference 2019, Universiti Kebangsaan Malaysia, Selangor, 20-22 August 2019

Shi, S., Li, L., Wang, X., Liu, H., Wang, Y. (2017). Analysis of the vehicle driving stability region based on the bifurcation of the driving torque and the steering angle. *Proc. Inst. Mech. Eng. Part D J. Automob. Eng.* 231, 984–998

Tavernini, D., Massaro, M., Velenis, E., Katzourakis, D. I., & Lot, R. (2013). Minimum time cornering: the effect of road surface and car transmission layout. *Vehicle System Dynamics*, 51(10), 1533-1547

Velenis, E., Frazzoli, E., & Tsiotras, P. (2010). Steady-state cornering equilibria and stabilisation for a vehicle during extreme operating conditions. *International Journal of Vehicle Autonomous Systems*, 8 (2-4), 217-241

Velenis, E., Katzourakis, D., Frazzoli, E., Tsiotras, P., & Happee, R. (2011). Steady-state drifting stabilization of RWD vehicles. *Control Engineering Practice*, 19(11), 1363-1376

Voser, C., Hindiyeh, R. Y., & Gerdes, J. C. (2010). Analysis and control of high sideslip manoeuvres. *Vehicle System Dynamics*, 48(S1), 317-336

MIJST
MIST International Journal of Science and Technology

Modeling and Control Simulation of a Robotic Chair-Arm: Protection against COVID-19 in Rehabilitation Exercise

M. Akhtaruzzaman[1*], Amir A. Shafie[2], Md Raisuddin Khan[3], and Md Mozasser Rahman[4]

[1] Dept. of Computer Science and Engineering, Military Institute of Science and Technology (MIST), Dhaka, Bangladesh
[2,3] Dept. of Mechatronics Engineering, International Islamic University Malaysia (IIUM), 53100 Kuala Lumpur, Malaysia
[4] Dept. of Mechanical Engineering Technology, Universiti Tun Hussein Onn Malaysia (UTHM), 84600 Pagoh, Johor, Malaysia
[1] R&D (Robotics) Section, DREAM Robotics Ltd., Dhaka, Bangladesh

emails: *[1]akhter900@cse.mist.ac.bd; [2]aashafie@iium.edu.my; [3]raisuddin@iium.edu.my; and [4]mozasser@uthm.edu.my*

ARTICLE INFO

Article History:

Received: 18th July 2020
Revised: 10th September 2020
Accepted: 11th October 2020
Published: 16th December 2020

Keywords:

1-DoF robotic arm
Robotic chair-arm
Robot-assisted rehabilitation
Lower-limbs therapeutic exercise
Robot-assisted system
COVID-19

ABSTRACT

In the field of rehabilitation, lower-limbs therapeutic exercise has become a challenging job for medical professionals in COVID-19 pandemic. Providing manual therapy to lower limbs is not an easy task and, in most cases, it involves multiple persons. Moreover, it is a monotonous job, and the service providers need to be in close contact with the patient thereby creating the risk of infection. In this circumstance, robot-assisted rehabilitation exercise for lower limbs offers a risk-free solution. This paper presents dynamic modeling and control simulation of One Degree of Freedom robotic chair-arm (robotic arm attached with a special chair). The control structure is designed with two compensators for position and velocity control. The simulation results show that the proposed system has a good potential in providing automatic rehabilitation therapy for lower limbs, especially for knee joint range of motion exercise. The results also indicate faster responses with settling time less than 0.04 *second* and steady-state error below 0.05. The findings show that a robotic chair arm can be used for providing automatic therapy to patients in situations like COVID-19 pandemic.

1. INTRODUCTION

The COVID-19 has become an epidemic throughout the world which has been forcing humanity to be demobilized by creating intangible obstacles and threats to fulfill our five basic needs, foods, clothing, shelter, healthcare, and education. Healthcare and education sectors are dangerously affected by the invasion of Corona Virus. COVID-19 is highly contagious which makes medical services difficult to provide. Clinical care service is one of the broad areas where robotics can contribute to change the sector to reach its highest level (Yang et al., 2020; Zeng, Chen, & Lew, 2020).

Global demand for rehabilitation services is increasing because of growing non-communicable diseases like stroke and heart attacks. Moreover, the current situation of the global pandemic raises greater demand for robot-assisted rehabilitation systems in minimizing the risk of contamination both for healthcare service providers and patients (Zeng, Chen, & Lew, 2020; Kimmig *et al.*, 2020). To increase Range of Motion (RoM) flexibility of knee joint and motor neuron dysfunction, continuous passive RoM exercise is a monotonous and arduous job in terms of physical labor and time. Repeated manual exercise also unable to comply with natural motion patterns during the whole exercise session. Furthermore, transporting the patient for each session increases time overheads, cost, and discomfort to the patients. Thus, to decrease the burden, design and control simulation of a 1-DoF robotic arm for knee RoM exercise is presented in this manuscript. The arm is attached with a special chair so that a disabled patient can be seated on to receive knee joint RoM therapeutic exercise.

Robot-assisted rehabilitation exercise for functional adaptation of knee joint RoM widens a great opportunity for post-stroke patients (Akhtaruzzaman *et al.*, 2019). Robot-assisted system also could be a great tool to measure functional improvements of muscles and joint motions (Huang *et al.*, 2019). The instrumentation system of a robotic arm can perform precise measurement of positions and forces and able to co-operate with human (Shi *et al.*, 2019). More importantly, electro-mechanical actuators of the system can perform a task repeatedly within the desired

workspace of a joint (Hussain, Xie, & Jamwal, 2013; Lee *et al.*, 2016; Shi *et al.*, 2019).

NeXOS was introduced by Bradley *et al.* (2009) as a 2-DoF automated system to perform active assistive as well as passive and resistive therapeutic exercises. Pre-trained visual trajectory and position information were implemented to make the system reliable for hip and knee extension-flexion exercise. Targeted users of the system were the stroke patients for post-stroke rehabilitation exercise. A robot-assisted system, Multi-Iso, was designed for knee extension-flexion exercise by Moughamir *et al.* (2002) that can provide assistive rehabilitation along with passive and resistive therapeutic exercises. A fuzzy intelligent control strategy was introduced in the system where sequence control mechanisms of position, velocity, and force were considered. For the treatment of Crouch gait, a powered exoskeleton system was designed to comply with the kinematic structure of knee, ankle, and foot (Lerner *et al.*, 2016). The robotic exoskeleton system was able to aid with knee-extension during gait training for adults and children.

Though the position-velocity control is not sufficient, it is the initial step for designing a robot assistive system. This paper describes the initial stage of a robot-assisted system for knee joint RoM rehabilitation exercise, thus presents dynamic modeling and position-velocity control simulation of the system. Newtonian dynamic analysis is adopted to determine the necessary equations. The control architecture is designed with two compensators based on Proportional-Derivative-Integral (PID) tuning method. Simulation results have confirmed the suitability of the proposed mechatronics system for its potential applications and improvements.

2. SYSTEM DESIGN AND MODELING

A. Mechanical Design and Component Selection

The system is designed so that a patient can be seated on the seat-mount while adjusting knee joint axes to be co-centric with the primary and secondary shaft rotational axis. Figure 1 presents the left view of the robot-assisted system as designed for knee joint RoM rehabilitation exercise.

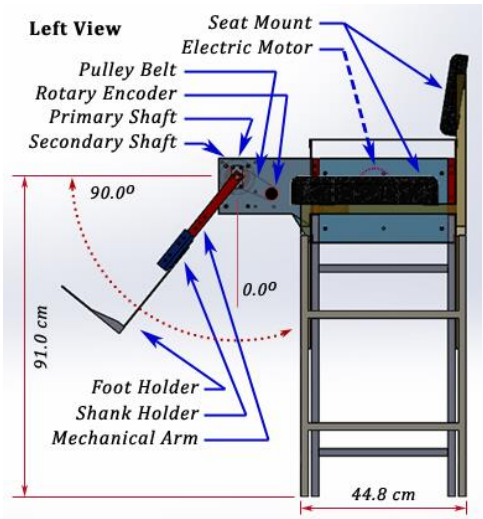

Figure 1: A Robotic Arm with a mechanical chair (Left View)

The robotic arm (mechanical arm) will be attached with the shank of the patient leg at the shank holder position and the foot will be attached with the foot holder of the system. The height of the knee joint axis is 91.0 cm enabling enough space for knee RoM exercise within the motion range from flexion to extension (Akhtaruzzaman *et al.*, 2019). For modeling and simulation, presented in this paper, 90.0° flexion of the knee is considered as a start (0.0°) and 0.0° extension of the knee is considered as end (90.0°) positions of robotic arm motion range. For prototype development, aluminum sheet-metal can be chosen (Abdezadeh *et al.*, 2016) to develop the extended structure of the chair.

The design focuses only on the right knee for experimental purposes and can be upgraded by applying the same mechanism at the left side of the chair to provide therapeutic exercise to the left knee. The mechanical and electro-mechanical components attached to the system prototype are DC Motor (SPG S8D40-24A with gearhead S8KA10B1), position sensor (M249 100Ω-K), pulleys, pulley belts, primary shaft, secondary shaft, rotary encoder (3806-500B-5-24F), and coupling. Electronics and control circuit of the rehabilitation system consists of a custom-designed latch module, relay module, motor driver (L298N H-Bridge), two μ-controllers (Arduino-Mega, master & slave), switch & connection module, ethernet module, and custom-designed multiport power-supply unit. A designed control algorithm is implemented in Arduino-Mega.

B. Determining System Torque

The free-body diagram of the proposed mechatronics system is presented in Figure 2. Based on the general equation of torque ($\tau = I\alpha$), formula of the system actuator torque (τ_M) is presented in Equation (1). Here, I is the rotational inertia and α is the angular acceleration. To determine the value of the Primary and Secondary Shafts angular acceleration (α_S), the time of one revolution is chosen as 24 seconds. So, revolution per minute (RPM) can be calculated as ($RPM = (1 * 60)/24 = 2.5\, rev/min$). Thus, angular acceleration (α_S) can be calculated as, $\alpha_S = \omega_S/t_S = 0.13\, rad/\sec^2$. Here, angular velocity, $\omega_S = (2.5 * 2\pi)/60\, rad/sec$, and time for 30° rotation, $t_S = 2\, sec$.

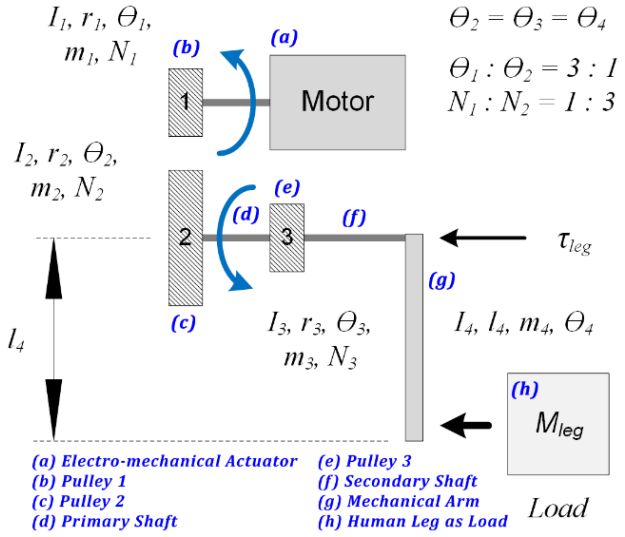

Figure 2: Free-body diagram of the mechatronics system

$$\tau_M = \begin{matrix} \frac{1}{2} m_1 r_1^2 \alpha_1 + \\ \left(\frac{N_1}{N_2}\right)^2 \left\{ \alpha_S \left(\frac{1}{2}(m_2 r_2^2 + m_3 r_3^2) + \frac{1}{3} m_4 l_4^2 \right) + \tau_{leg} \right\} \end{matrix} \quad (1)$$

Here, m is mass, r is pulley radius, θ is angular deflection, N is pulley teeth, and l is the length of the mechanical arm.

By considering the relations, $\alpha_1 = \alpha_S(N_2/N_1)$ and $(N_1/N_2) = N_S$, the actuator torque equation can be modified as shown in Equation (2). Here, $N_1 : N_2 = 1:3$. The necessary values of the parameters are presented in Table 1. Required torques at the knee joint, while the patient is in a sitting position, are identified from the study conducted by Akhtaruzzaman *et al.* (2019).

$$\tau_M = \begin{matrix} \frac{\alpha_S}{2} \left\{ \frac{1}{N_S}(m_1 r_1^2) + N_S^2 \left(m_2 r_2^2 + m_3 r_3^2 + \frac{2}{3} m_4 l_4^2 \right) \right\} \\ + N_S^2 \tau_{leg} \end{matrix} \quad (2)$$

Table 1
Parameters to Calculate Required Torque of the System Actuator

Parameter Symbols	Values
m_1	030.0 g
m_2	751.0 g
m_3	215.0 g
m_4	350.0 g
r_1	01.50 cm
r_2	04.50 cm
r_3	03.25 cm
l_4	30.00 cm
α_S	$0.1300 * (180/\pi)\ ^{deg}/_{sec^2}$
N_1	20.0 teeth
N_2	60.0 teeth
τ_{leg}	$\begin{cases} 895.1\ N.cm & for\ \theta_1 = 0° \\ 300.0\ N.cm & for\ \theta_1 = 65° \end{cases}$

Required torque of the system actuator is calculated as $100.4\ N.cm$ for knee joint torque as $895.1\ N.cm$ at full extension of the knee. For the 25° position of knee joint (knee joint torque is $300.0\ N.cm$), the required torque of the system actuator is determined as $034.3\ N.cm$. By considering the safety factor as $S_f = 1.5$, calculated required torques are presented in Equation (3).

$$\tau_m = \begin{cases} (\tau_M \times s_f) \approx 150.0\ N.cm & for\ \theta_1 = 90° \\ (\tau_M \times s_f) \approx 050.0\ N.cm & for\ \theta_1 = 25° \end{cases} \quad (3)$$

C. System Dynamics

The conceptual Electro-mechanical model of the system actuator is presented in Figure 3. Here τ_m is rotor torque produced by the applied current $(i(t))$ from V DC source. The τ_m is proportional to its magnitude. Effective inertia of armature is presented by I_m. Angular deflection $(\theta(t))$ of the rotor produces back Electromotive Force (EMF) $(E_b(t))$ which is proportional to rotor angular velocity $(d\theta(t)/d(t) = \dot{\theta}(t))$. Input-output ratio of gearhead is presented as, $(N_m : N_L = 1:10)$. The friction force of the gearhead module is zero $(\tau_{f_m} = 0)$. The actuator module is connected with a switching module which is controlled by the control signals through Pulse Width Modulation (PWM) module.

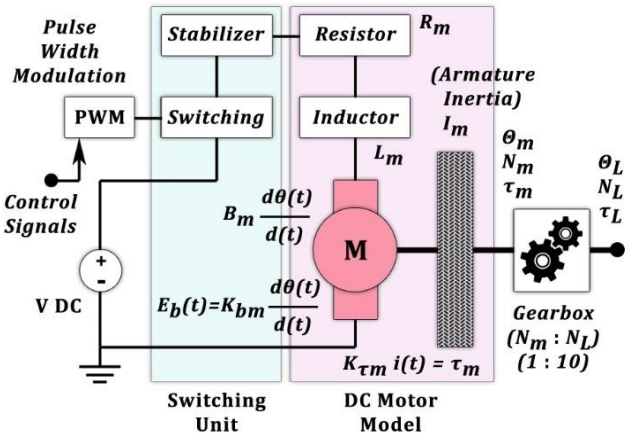

Figure 3: Conceptual Electro-mechanical model of DC Motor

Based on the characteristics of this electro-mechanical module, two differential equations can be presented as shown in Equation (4). In the equation, the constant parameters are, coil resistance (R_m), inductance (L_m), torque constant (K_{τ_m}), and back EMF (K_{b_m}). Armature inertia, viscous friction, armature load, and external load are presented by I_m, B_m, τ_m and τ_L, respectively.

$$\left.\begin{aligned} L_m \frac{di(t)}{dt} + K_{b_m} \frac{d\theta_m(t)}{dt} + R_m i(t) - v_m(t) = 0 \\ I_m \frac{d^2\theta_m(t)}{dt^2} + B_m \frac{d\theta_m(t)}{dt} + \frac{N_m}{N_L}(\tau_L) - K_{\tau_m} i(t) = 0 \end{aligned}\right\} \quad (4)$$

Now, from the free-body diagram in Figure 2, the external load (τ_L) can be formulated, as shown in Equation (5).

$$\tau_L = \left(I_1 + \left(\frac{N_1}{N_2}\right)^2 (I_2 + I_3 + I_4 + I_{leg})\right) \frac{d^2\theta_1(t)}{dt^2} \quad (5)$$

Now by replacing τ_L in the second part of Equation (4), Equation (6) can be formulated which is the necessary differential equation of the proposed system. Here, $\theta_L = \theta_1$, $N_L = N_1$, and $^{N_m}/_{N_L} = {}^{\theta_1}/_{\theta_m}$ are applied to establish a relation with control parameter θ_1. Necessary parameter definitions are presented in Equation (7). Table 2 presents the necessary parameter values of the system dynamic model.

$$\left.\begin{aligned} L_m \frac{di(t)}{dt} + K_{b_m} N_{R_m} \frac{d\theta_1(t)}{dt} + R_m i(t) - v_m(t) = 0 \\ I_{EQ} \frac{d^2\theta_1(t)}{dt^2} + B_{EQ} \frac{d\theta_1(t)}{dt} - K_{\tau_m} i(t) = 0 \end{aligned}\right\} \quad (6)$$

$$\left.\begin{aligned} I_{EQ} &= N_{R_m} I_m + \frac{1}{N_{R_m}} \left(I_1 + N_R{}^2 (I_2 + I_3 + I_4 + I_{leg})\right) \\ B_{EQ} &= N_{R_m} B_m \\ N_R &= \frac{N_1}{N_2} \\ N_{R_m} &= \frac{N_L}{N_m} \\ I_1 &= \frac{1}{2} m_1 r_1^2 \\ I_2 &= \frac{1}{2} m_2 r_2^2 \\ I_3 &= \frac{1}{2} m_3 r_3^2 \\ I_4 &= \frac{1}{3} m_4 l_4^2 \\ I_{leg} &= m_{leg} l_{com_{leg}}^2 \end{aligned}\right\} \quad (7)$$

Table 2
Necessary Parameters of the System

Parameter Symbols	Values
K_{τ_m}	$1500\,{}^{N.cm}/_{amp}$
K_{b_m}	$0.125\,{}^{v}/_{rad.sec}$
R_m	$5\ \Omega$
L_m	$0.055\ H$
B_m	$034.8\,{}^{N.cm}/_{rad.sec}$
I_m	$0.0068\,{}^{g}/_{cm^2}$
m_{leg}	$4030.0\ g$
$l_{com_{leg}}$	$12.92\ cm$
N_m	10
N_L	100

D. System Transfer Functions (TF)

The first part of Equation (6) is the electrical circuit dynamics, and the second part is the mechanical dynamics. Now by applying Laplace Transform (LT), the differential equation (in time domain) can be transformed into an algebraic equation (in frequency domain) to find out the solutions and present as output-over-input (transfer function of the system). After applying LT, the new form of Equation (6) is presented in Equation (8) where the mechanical dynamic equation is rewritten into two separate formats, one is based on angular position (θ_1 for position control) and the other one is based on angular velocity ($\dot{\theta}_1$ for velocity control).

$$\left.\begin{aligned} &sL_mI(s) + sK_{b_m}N_{R_m}\theta_1(s) + R_mI(s) - v_m(s) = 0 \\ &s^2I_{EQ}\theta_1(s) + sB_{EQ}\theta_1(s) - K_{\tau_m}I(s) = 0 \\ &sI_{EQ}\dot{\theta}_1(s) + B_{EQ}\dot{\theta}_1(s) - K_{\tau_m}I(s) = 0 \end{aligned}\right\} \quad (8)$$

From the above equation, necessary sub equations can be determined for $\left(V_m(s) - sK_{b_m}\theta(s)\right)$ from electrical dynamics and $I(s)$ from two equations of mechanical dynamics. Now replacing $I(s)$ in the electrical dynamic equation, two TFs can be determined as presented in Equation (9) and (10). The TF in Equation (9) is for position control and the TF in Equation (10) is for velocity control.

$$\frac{\theta_1(s)}{V_m(s)} = \frac{K_{\tau_m}}{s^3I_{EQ}L_m + s^2(I_{EQ}R_m + B_{EQ}L_m) + s(B_{EQ}R_m + K_{b_m}K_{\tau_m}N_{R_m})} \quad (9)$$

$$\frac{\dot{\theta}_1(s)}{V_m(s)} = \frac{K_{\tau_m}}{s^2I_{EQ}L_m + s(I_{EQ}R_m + B_{EQ}L_m) + (B_{EQ}R_m + K_{b_m}K_{\tau_m}N_{R_m})} \quad (10)$$

3. CONTROL ENGINEERING

The motion of the system arm is operated by an input voltage V_m. To control the arm position and motion velocity, two PID compensators (C_θ and $C_{\dot{\theta}}$) need to be designed. In the manual PID tuning, K_P is increased to minimize rise time while $K_I = K_D = 0$. Then, for minimizing any steady-state error (SSE), K_I is increased. Finally, for ensuring faster settling time, K_D is increased (reduce overshoot). In this paper, MATLAB SIMULINK based tuning is considered.

To design a robot-assisted rehabilitation system, it is necessary to define the limits of performance control parameters (PCP) values which are determined from the literatures presented in this paper. Table 3 presents the various results identified from the literatures. To design a robust rehabilitation robotic device, Percent of Overshoot (%OS), Rise time (RT), Settling time (ST), and Steady-state error (SSE) must be as minimum as possible. Thus, the average values of the identified PCP parameters, presented in Table 3, are considered in designing the position-PID compensator. The PCP limits are chosen as, $(0.00 < \%OS < 12.00)$, $(0.00 < RT < 01.20\ sec.)$, $(0.00 < ST < 3.00\ sec.)$, and $(0.00 < SSE < 0.11)$.

Table 3
Selection of Performance Control Parameters (PCP) to design position-PID

Ref.	Control Types	PCP			
		%OS	RT (sec.)	ST (sec.)	SSE
Joyo *et al.* (2019) *[joint-1]*	PSO-PID	17.225	00.095	00.924	--
	ABC-PID	01.836	00.275	00.413	--
	ZN-PID	51.417	00.282	04.537	--
Yoyo *et al.* (2019) *[joint-2]*	PSO-PID	00.000	00.421	00.652	--
	ABC-PID	05.101	00.022	00.095	--
	ZN-PID	10.284	00.028	01.400	--
Ali *et al.* (2018)	PID	07.400	00.400	02.380	--
	Fuzzy-PID	07.000	00.510	03.500	--
Faizura *et al.* (2020)	PID	38.000	02.130	08.250	00.380
	Fuzzy	02.000	02.800	07.250	00.020
	Fuzzy-PID	00.000	04.980	06.500	00.000
	PID-PSO	04.000	02.070	05.300	00.040
Average values		**12.022**	**01.168**	**03.433**	**00.110**

PSO: Particle Swarm Optimization; ABC: Artificial Bee Colony; ZN: Zeigler-Nichols; PID: Proportional-Integral-Derivative

A. Compensator for Position Control (C_θ)

MATLAB Simulink block-diagram for position control (C_θ) PID compensator is presented in Figure 4. Position error is calculated by subtracting the position feedback from desired position and feed to the position-PID. The PID compensator generates a necessary control signal and passes it into the system plant. Within the range of PCP limits, in the first tuning the values of K_P, K_I, and K_D are selected as 0.562, 0.009, and 0.304, respectively. The resultant system responses are presented in Figure 5 where the position responses of the system are $\%OS \approx 9.90$, $RT \approx 1.00\ sec.$, $ST \approx 3.00\ sec.$, and $SSE \approx 0.06$. Though PCP values of the system are in the selected range, the velocity response is in under-damp condition. Thus, the PID of C_θ needs to be tuned more to get a robust response of the system. Table 4 presents the PCP values of system responses for four different tunings of C_θ. Among the various responses, the best performance is observed for $K_P = 04.530$, $K_I = 00.567$, and $K_D = 04.033$. Under this condition, the simulated response is presented in Figure 6.

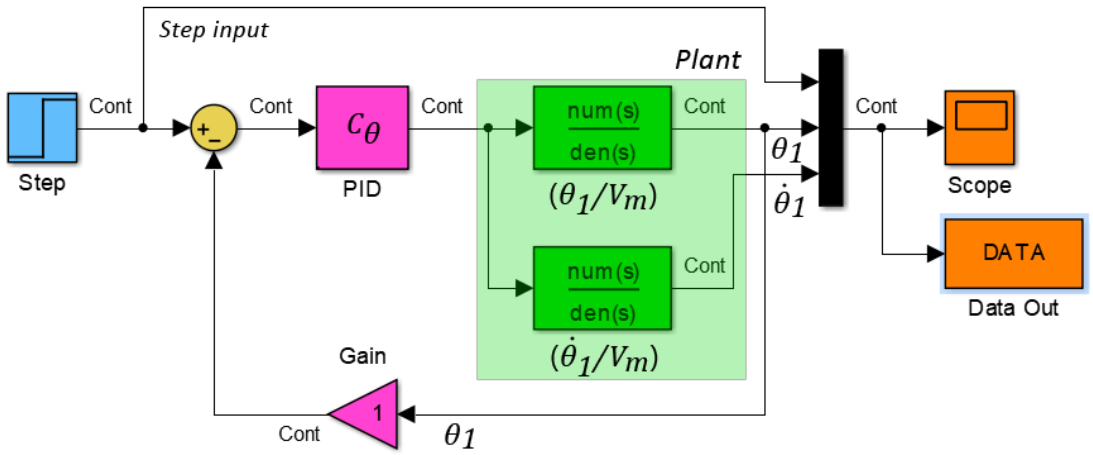

Figure 4: Control architecture (MATLAB Simulink diagram) in designing C_θ PID Compensator

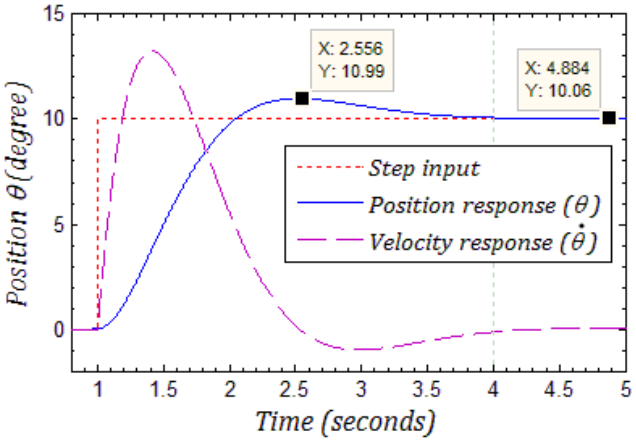

Figure 5: System response for PID compensator C_θ where $K_P = 0.562$, $K_I = 0.009$, and $K_D = 0.304$

According to the graph (Figure 6), no overshoot is observed for the position response ($\%OS = 00.00$), the steady-state error is observed as a minimum ($ESS = 0.050$). The system also shows the faster rise time and faster settling time ($RT = 00.240\ sec.$ and $ST = 00.300\ sec.$).

Table 4

Various PCP values for different tuning of position-PID (C_θ)

Tune	PID Values	PCP			
		%OS	RT (sec.)	ST (sec.)	SSE
1st	$K_P = 00.562$ $K_I = 00.009$ $K_D = 00.304$	09.900	01.000	03.000	00.060
2nd	$K_P = 01.099$ $K_I = 00.049$ $K_D = 01.109$	00.000	00.859	01.040	00.080
3rd	**$K_P = 04.530$** **$K_I = 00.567$** **$K_D = 04.033$**	**00.000**	**00.240**	**00.300**	**00.050**
4th	$K_P = 52.979$ $K_I = 29.090$ $K_D = 21.437$	01.300	00.054	0.277	00.060

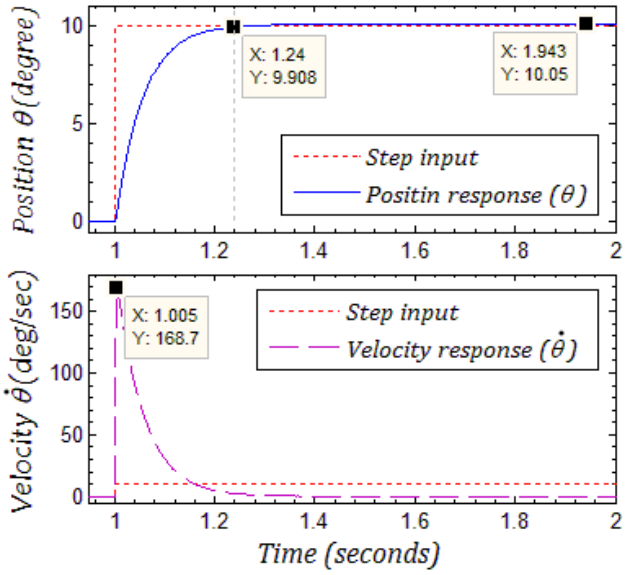

Figure 6: System response (3rd tuning) for PID compensator C_θ where $K_P = 4.530$, $K_I = 0.567$, and $K_D = 4.033$

B. Compensator for Velocity Control ($C_{\dot{\theta}}$)

A robot-assisted rehabilitation system must have the capability to follow a trajectory with the desired velocity. The sudden change of velocity may cause the system to unstable creating secondary injury to the targeted limbs. In Figure 6, the velocity response shows high deflection, thus it is necessary to design 2nd compensator ($C_{\dot{\theta}}$) for velocity control. The control architecture is presented in Figure 7. Considering the chosen PCP limits, the values of K_P, K_I, and K_D are tuned as 140.00, 18416.00, and 00.10, respectively. Table 5 presents the various responses of four different trials from where the results of the 3rd trial are considered, thus selected the velocity-PID parameter values. To design the control architecture, the switching mechanism is adopted. The philosophy behind this technique is that the velocity-PID will dominate to maintain the desired constant velocity during motion and the control responsibility will switch to the position-PID at the moment of the system arm reaches the desired position and maintain the desired angular state.

Table 5

Various PCP values for different tuning of velocity-PID ($C_{\dot{\theta}}$)

Tune	PID Values	PCP			
		%OS	RT (sec.)	ST (sec.)	SSE
1st	$K_P = 45.00$ $K_I = 8516.00$ $K_D = 00.80$	25.600	00.021	00.356	−0.120
2nd	$K_P = 80.00$ $K_I = 18516.00$ $K_D = 00.20$	34.700	00.009	00.069	−0.018
3rd	**$K_P = 140.00$** **$K_I = 18416.00$** **$K_D = 00.10$**	**29.500**	**00.006**	**00.028**	**−0.019**
4th	$K_P = 180.00$ $K_I = 29323.00$ $K_D = 00.10$	41.500	***Unstable***		

The system plant (system dynamic model) is basically a Single-Input Multi-Output (SIMO) system as both position and velocity outputs depend on the input of electric voltage (V_m) to the system plant. The design of the control architecture reflects the parallel configuration of two compensators. Here the position and velocity errors are feed to position-PID (C_θ) and velocity-PID ($C_{\dot{\theta}}$) compensators separately. The output of both PIDs is then summed up and feed as a single input to the system plant. To observe the system performance, the designed architecture is simulated for a constant velocity input as 10 $deg./sec.$ while a step input is applied for position change from 0.0° to 20.00°. At this condition, the arm must rise to its desired angle within two seconds while maintaining the desired velocity complying with the selected PCP characteristics. Figure 8 shows the simulated responses of the system and corresponding error characteristics for such input conditions.

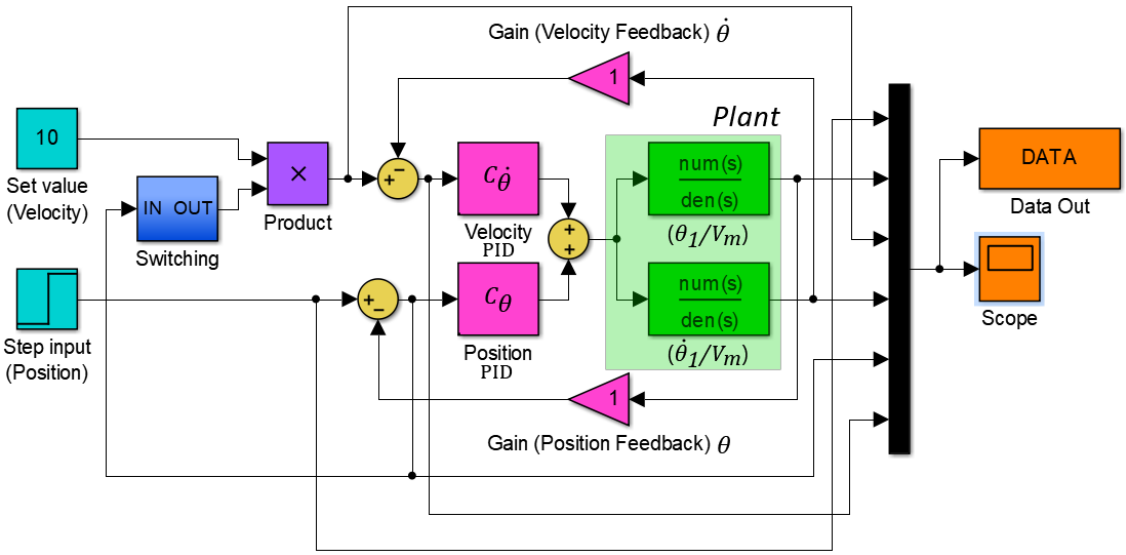

Figure 7: Control architecture (MATLAB Simulink diagram) in designing C_θ and $C_{\dot{\theta}}$ PID Compensators

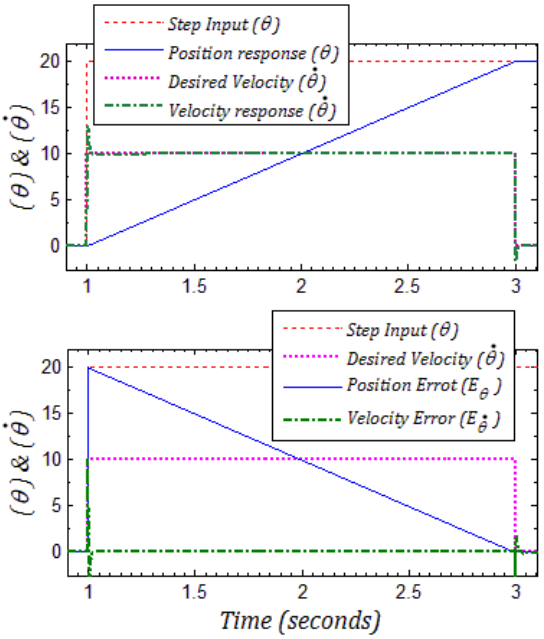

Figure 8: System responses (3rd tuning) of velocity-PID ($C_{\dot{\theta}}$)

4. RESULTS AND DISCUSSION

Results of the designed architecture show a stable system response both in position and velocity control. The desired position and velocity of the robot arm are achieved within the desired PCP value ranges. The system is simulated for various input conditions to confirm the suitability of the designed control architecture. Figure 8 has presented the simulated results of the system for the input parameters as 0.0° to 20.0° motion range with a constant velocity of 10.0 $deg./sec.$ Angle rise time satisfies the desired time for about two seconds with a smooth motion trajectory. Though some deflections are observed for velocity response at the initiation and termination of motion, the results of position control satisfy selected PCP ranges.

Figure 9 presents clear observations of velocity response and the corresponding error characteristics at the initiation of motion. The graph shows that the rise time is about 0.006 $sec.$ with the percent of overshoot is about 29.50. The settling time of the velocity response is around 0.028 $sec.$ and steady-state error is almost 0.019. The results comply with the PCP value ranges for position

response, thus ensure the suitability of the designed control architecture.

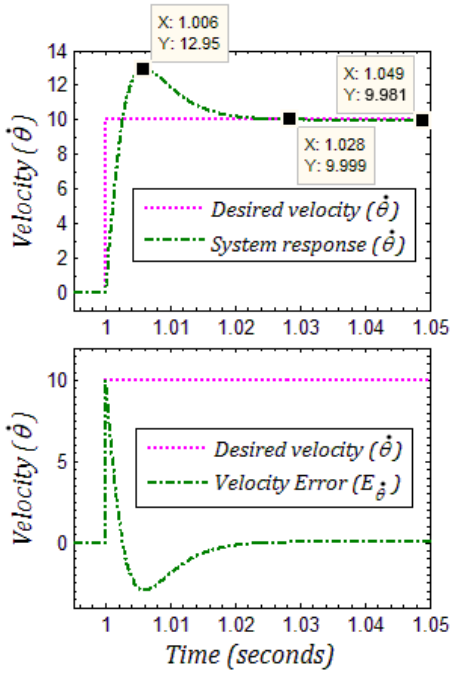

Figure 9: Velocity response and corresponding errors of the system at the initiation of motion

Motion termination occurs when the system reaches the desired angular position. At this moment, the switching is activated, and the control is switched back to the position-PID compensator to hold the arm at the desired angle. At the same time, the velocity reaches zero. Figure 10 shows the velocity response of the system at the termination of motion. The graph shows that the rise time is around 0.006 *sec*., settling time is about 0.027 *sec*., and steady-state error is 0.0037. The percent of overshoot is detected as 16.20. For a rising motion of the system arm, two switching conditions have occurred, one is position-PID to velocity-PID at the initiation of motion (hold at 0.0° to swing) and the other is velocity-PID to position-PID at the termination of motion (swing to hold at 20.0°). A comparison of the velocity responses in between these two switching conditions reflects that all the PCP values at motion-termination are lower than motion-initiation. This behavior explains that the system needs less energy to settle down the velocity to zero at hold condition. Opposingly, the system needs high energy at the motion-initiation state to maintain the desired velocity. A similar test with different input conditions is simulated resulting in the same behavior of the system response. The system is also tested with an external disturbance input. The disturbance is applied at the position response of the system to observe the effects on system stability in terms of position and velocity responses. Figure 11 shows the system control architecture with an Impulse Generator (IG) as an external disturbance to the position output (θ) of the plant.

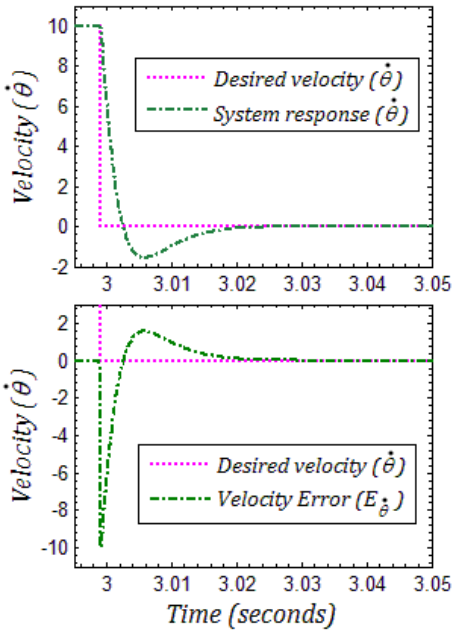

Figure 10: Velocity response and corresponding errors of the system at the termination of motion

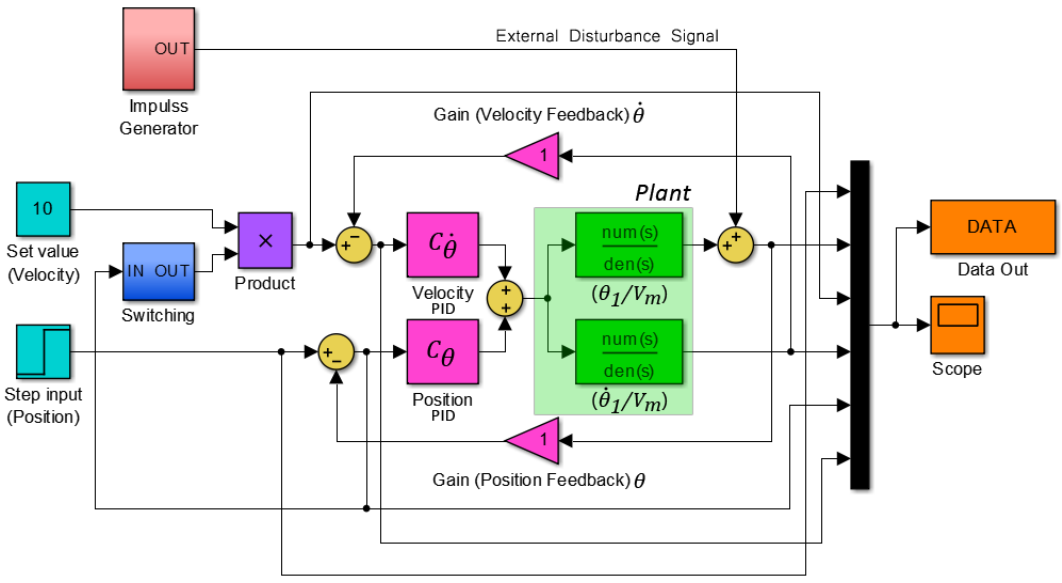

Figure 11: System control architecture with an external disturbance at the position output just before the position feedback

The IG generates a single pulse of 0.001 $sec.$ pulse width and 10.00° amplitude. The impulse signal is added with the θoutput response of the system; thus, position response reflects a sharp rise and falls at a specific time of the system operation. For the test simulation, two impulse signals are applied, i) a positive impulse during motion at 4.70 $sec.$, and ii) a negative impulse during 45.00°hold condition at 6.00 sec. Figure 12 shows the system response for the input parameters as 10.00 $deg./sec.$ velocity and step function from 0.0° to 45.00°.

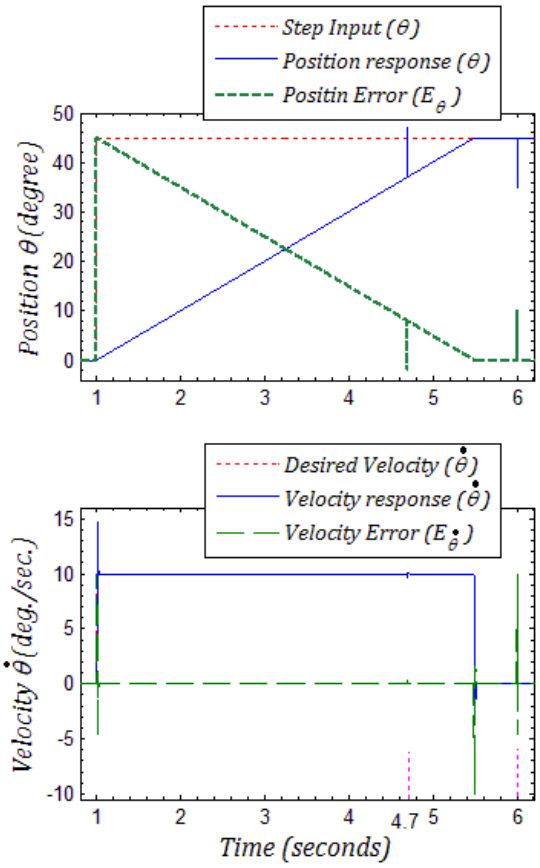

Figure 12: System position and velocity responses for Position set-point at 45.0° and Velocity set-point at 10.0 $deg./sec.$ while external disturbances are at 4.70 $sec.$ (positive disturbance) and at 6.00 $sec.$ (negative disturbance)

According to the above figure, the position response of the system shows a smooth transition at the initiation and termination of motion. Velocity response shows some deflections at the initiation at time 1.00 $sec.$ and termination of the motion at 5.50 sec. The behavior is clearly presented in Figure 13 where (a) reflects velocity response with error behavior at the initiation and (b) shows velocity response with corresponding error behavior at the termination of motion. From the response graphs, the PCP values are extracted as $\%OS = 47.30$, $RT = 0.006\ sec.$, $ST = 0.033\ sec.$ and $SSE = -0.044$ at the initiation of motion and $\%OS = 15.34$., $RT = 0.006\ sec.$, $ST = 0.031\ sec.$, and $SSE = 0.0041$ at the termination of motion. The response of the system for positive impulse disturbance at 4.70 $sec.$ during motion and negative impulse disturbance at 6.00 $sec.$ during the 45.00° hold position are presented in Figure 14 and Figure 15, respectively. For the positive impulse during rising motion, velocity goes down to about 9.713 $deg./sec.$ and reaches to the desired velocity ($\approx$ 10.00 $deg./sec.$) at 4.728 $sec.$, reflecting $ST = 0.028\ sec.$, $\%OS = 2.787$, $RT = 0.008\ sec.$ and $SSE = 0.0030$. For the negative impulse, the desired velocity rises to its set point and falls to zero reflecting the impulse disturbance to the velocity input (Figure 15). Velocity response rises to 4.603 $deg./sec.$ and settles down to zero by 0.022 $sec.$ with $\%OS = 5.110$, as presented in Figure 15.

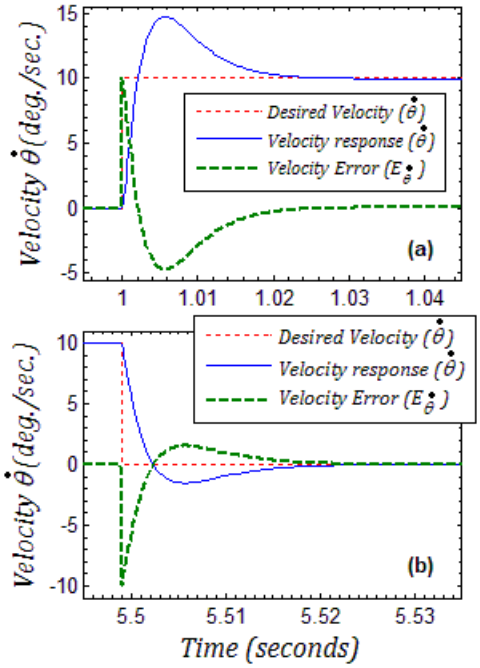

Figure 13: Velocity responses and error behaviors; (a) at motion initiation, and (b) at motion termination

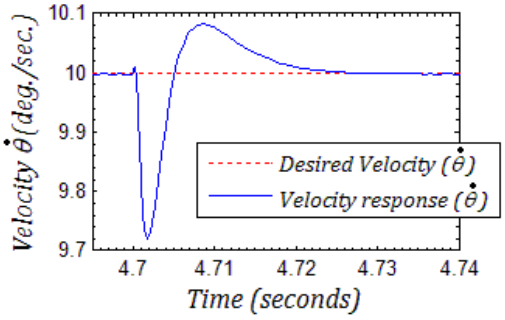

Figure 14: Velocity responses of the system for positive disturbance (position) input at 4.7 $sec.$

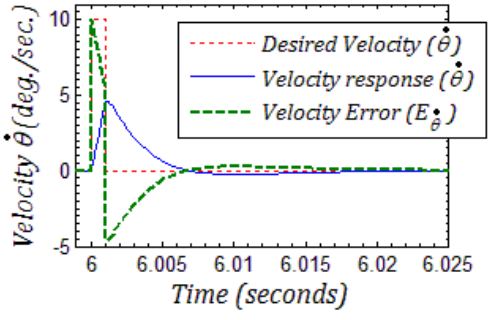

Figure 15: Velocity responses for negative disturbance (position) at 6.00 $sec.$ while robot-arm is holding at 45°

For the impulse disturbance, system output shows a very little impact on the position (θ) response. Figure 16 presents the position response for $-10°$ impulse at 6.00 $sec.$ while the robot arm is in holding a position at 45.00° angles. From various simulation results, it is observed that the system shows good performances while the velocity range is $0.00 < \dot{\theta} < 14.00\ deg./sec.$ At 0.00 $deg./sec.$ there is no angular motion observed at the robot arm. Conversely, the velocity greater than 14.00 $deg./sec.$ makes the system unstable. Table 6 presents the PCP values of position and velocity responses for various input conditions.

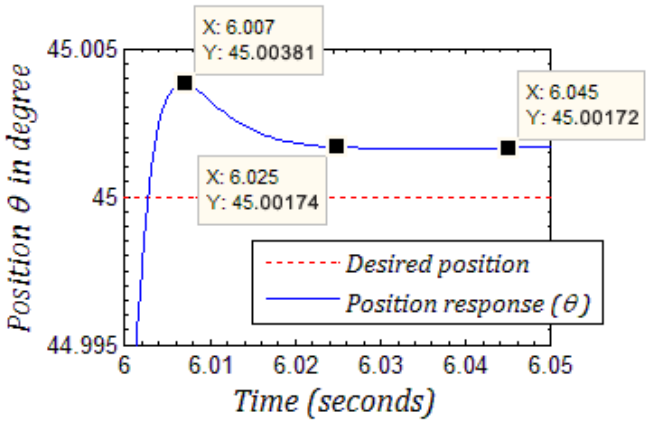

Figure 16: Position (θ) response of the system for $-10°$ impulse disturbance at 6.00 $sec.$ while the robot arm is holding at 45.0° angle

Table 6
System PCP values of position and velocity responses for various input conditions

Input Conditions	Outputs	PCP Values			
		%OS	RT (sec.)	ST (sec.)	SSE
Step: 0° to 20° ***$\dot{\theta}$: 10 $deg./sec.$***	$\dot{\theta}$ *@ start of motion*	29.50	0.006	0.028	0.0190
	$\dot{\theta}$ *@ end of motion*	16.20	0.006	0.027	0.0037
	$\dot{\theta}$ *for* $+10°$ *impulse @ motion*	19.66	0.009	0.031	0.0030
	$\dot{\theta}$ *for* $+10°$ *impulse @* 20° *hold*	5.405	0.010	0.022	0.0030
	θ *for* $+10°$ *impulse @* 20° *hold*	0.036	0.007	0.025	0.0016
Step: 0° to 45° ***$\dot{\theta}$: 10 $deg./sec.$***	$\dot{\theta}$ *@ start of motion*	47.30	0.006	0.033	0.0440
	$\dot{\theta}$ *@ end of motion*	15.34	0.006	0.031	0.0041
	$\dot{\theta}$ *for* $+10°$ *impulse @ motion*	2.787	0.008	0.028	0.0030
	$\dot{\theta}$ *for* $-10°$ *impulse @* 45° *hold*	5.110	0.010	0.022	0.0017
	θ *for* $-10°$ *impulse @* 45° *hold*	0.038	0.007	0.025	0.0017

5. CONCLUSIONS

This paper presents dynamic modeling and simulation of a robot-assisted rehabilitation system for knee joint RoM exercise. The paper describes a control architecture for position and velocity control of a 1-DoF robotic arm attached with a mechanical chair. The viability of the proposed control architecture is verified by performing simulations for various input parameter sets. The main goal is to provide robot-assisted motion exercise to the knee joint ensuring a smooth and continuous motion pattern.

The designed model basically reflects a SIMO system as it has one input and two output channels. From the dynamic model of the system, transfer functions are derived to design the Plant model. The control architecture is designed with two PIDs as parallel compensators, position-PID (C_θ) for position control and velocity-PID ($C_{\dot{\theta}}$) for velocity control. A switching mechanism is adopted to transfer the control from one PID to another at the transition moments, hold to swing transition (motion initiation) and swing to hold transition (motion termination). The position-PID is designed by determining some PCP parameter values based on the literatures studied and presented in this paper. Then velocity-PID is designed through iterative technique. In this case, MATLAB based tuning method is followed and PID parameter values are selected after some comparative analysis among the results of several iterations. Finally, several simulation tests were conducted to observe the PCP responses of the system in terms of position (θ) and velocity ($\dot{\theta}$) responses of the system.

Responses of the system show impressive results as the PCP values are in the selected ranges for position response. The results show, for the position response, the $\%OS < 12.00$, $RT < 1.00\ sec.$, $ST < 3.00\ sec.$, and $SSE < 0.100$. Velocity responses also present very low rise-time, settling-time, and steady-state error with the $\%OS$ in between 0.036 and 47.50. Although, experiments show that the velocity range for the smooth operation of the system is 1.00 $deg./sec.$ to 13.00 $deg./sec.$, highest recommended velocity is 10.00 $deg./sec.$ Velocity higher than this limit will cause the system unstable.

Experimental results have ensured the viability of the system for implementation and practical use. Though only position and velocity control are not enough for a Man-Machine cooperative robot, this experiment presents the initial step in designing such a machine. In this COVID-19 situation, this kind of automatic rehabilitation system is in high demand for clinical therapeutic exercise to ensure the social distance during providing the services to the patients. Automated robot-assisted therapy also could be beneficial for military rehabilitation. The system can be improved by using PID improving techniques and applying several control mechanisms like Passivity based control (PBC), Linear quadratic regulator (LQR), Linear quadratic Gaussian (LQG), Force control, Impedance control, Reinforcement learning, Fuzzy intelligent control, Artificial Neural Network (ANN), and so on (Akhtaruzzaman *et al.*, 2009; Akhtaruzzaman & Shafie, 2010; Akdogan & Adli. 2011).

ACKNOWLEDGEMENTS

The authors would like to express their gratitude to the Ministry of Education, Bangladesh, Ministry of Higher Education (MOHE), Malaysia; the department of Computer Science and Engineering, Military Institute of Science and Technology (MIST), Bangladesh; and the department of Mechatronics Engineering, Kulliyyah of Engineering, International Islamic University Malaysia (IIUM), Malaysia. The authors also express their appreciation to the R&D (Robotics) Section, DREAM Robotics Ltd., Dhaka, Bangladesh, and thankful to the editors and anonymous reviewers for providing insightful suggestions and comments to improve the manuscript.

REFERENCES

Abdezadeh, S., Saadi, D., Tohidirad, Y., Rashidy, R., & Aliabadi, Z. S. (2016). Hardware Board Design and Simulation of Lower Limb Rehabilitation Robot. *Majlesi Journal of Mechatronic Systems (MJMS)*, 5(3), 1-10.

Akdogan E. and Adli M. A. (2011). The design and control of a therapeutic exercise robot for lower limb rehabilitation: Physiotherabot. *Mechatronics*, Elsevier Ltd., 21, 509-522.

Akhtaruzzaman, M., & Shafie, A. A. (2010, August 4-7). Modeling and Control of a Rotary Inverted Pendulum Using Various Methods, Comparative Assessment and Result Analysis. Proceedings of the 2010 IEEE International Conference on Mechatronics and Automation, Xi'an, China, 1342-1347.

Akhtaruzzaman, M., Akmeliawati, R., & Yee, T. W. (2009, December 28 – 30). Modeling and Control of a Multi degree of Freedom Flexible Joint Manipulator. Second International Conference on Computer and Electrical Engineering, Dubai, UAE. (pp. 249-254).

Akhtaruzzaman, M., Shafie, A. A., Khan, M. R., & Rahman, M. M. (2019, December 20-22). Knee Joint Kinesiology: A Study on Human Knee Joint Mechanics. 4th International Conference on Electrical Information and Communication Technology (EICT). Khulna, Bangladesh.

Ali, A., Ahmed, S. F., Kadir, K. A., Joyo, M. K., & Yarooq, R. N. S. (2018, May 11-12). Fuzzy PID controller for upper limb rehabilitation robotic system. 2018 IEEE International Conference on Innovative Research and Development (ICIRD), Bangkok, Thailand, (pp. 1-5), doi: 10.1109/ICIRD.2018.8376291.

Bradley, D., Marquez, C., Hawley, M., Brownsell, S., Enderby, P., & Mawson, S. (2009). NeXOS - the design, development, and evaluation of a rehabilitation system for the lower limbs. *Mechatronics*, 19, 247-257.

Faizura, W. T. W., Luqman, M. Z. M., Hafiz, O. M., Naim, M. S., Armin, S. A., & Irraivan, E. (2020). Control Techniques of Multi-Fingered Hand for Rehabilitation. *Journal of Physics: Conference Series*, 1532, 012026. doi:10.1088/1742-6596/1532/1/012026

Huang, Y., Nam, C., Li, W., Rong, W., Xie, Y., Liu, Y., Qian, Q., & Hu, X. (2019). A comparison of the rehabilitation effectiveness of neuromuscular electrical stimulation robotic hand training and pure robotic hand training after stroke: A randomized controlled trial. *Biomedical Signal Processing and Control*, Elsevier Ltd., 56, 1-10.

Hussain, S., Xie, S. Q., & Jamwal, P. K. (2013). Control of a robotic orthosis for gait rehabilitation. *Robotics and Autonomous Systems*, Elsevier B.V., 61, 911-919.

Joyo, M. K., Raza, Y., Ahmed, S. F., Billah, M. M., Kadir, K., Naidu, K., … Mohd Yusof, Z. (2019). Optimized Proportional-Integral-Derivative Controller for Upper Limb Rehabilitation Robot. *Electronics*, 8(8), 826. doi:10.3390/electronics8080826

Kimmig, R., Verheijen, R. H. M., Rudnicki, M., & SERGS Council. (2020). Robot assisted surgery during the COVID-19 pandemic, especially for gynecological cancer: a statement of the Society of European Robotic Gynaecological Surgery (SERGS). *J Gynecol Oncol*, 31(3). doi: 10.3802/jgo.2020.31.e59

Lee, M., Sung, D. J., Lee, J., Oh, I., Kim, S., Kim, S., & Kim, J. (2016). Enhanced knee joint function due to accelerated rehabilitation exercise after anterior cruciate ligament reconstruction surgery in Korean male high school soccer players. *Journal of Exercise Rehabilitation*, 12(1), 29-36.

Lerner, Z. F., Damiano, D. L., Park, H. S., Gravunder, A. J., & Bulea, T. C. (2016). A Robotic Exoskeleton for Treatment of Crouch Gait in Children with Cerebral Palsy: Design and Initial Application. *IEEE Transactions on Neural System & Rehabilitation Engineering*. 99, 1-10. doi: 10.1109/TNSRE.2016.2595501.

Moughamir, S., Zaytoon, J., Manamanni, N., & Afilal, L. (2002). A system approach for control development of lower limbs training machines. *Control Eng. Pract.*, 10, 287-299.

Shi, D., Zhang, W., Zhang, W., & Ding, X. (2019). A Review on Lower Limb Rehabilitation Exoskeleton Robots. *Chin. J. Mech. Eng*. 32(74), 1-11, https://doi.org/10.1186/s10033-019-0389-8

Yang, G. Z., Nelson, B. J., Murphy, R. R., Choset, H., Christensen, H., Collins, S. H., Dario, P., Goldberg, K., Ikuta, K., Jacobstein, N., Kragic, D., Taylor, R. H., & McNutt, M. (2020). Combating COVID-19—The role of robotics in managing public health and infectious diseases, *Science Robotics*, 5(40), eabb5589, 1-2.

Zeng, Z., Chen, P. J., & Lew, A. A. (2020). From hightouch to high-tech: COVID-19 drives robotics adoption. *Tourism Geographies*. 22(3), 724-734, doi: 10.1080/14616688.2020.1762118

CALL FOR PAPERS

MIJST invites to submit Unpublished, Original, and Innovative research works from any branch of Engineering, applied sciences, and related areas.

Submitted manuscripts will undergo a double-blind peer-review process. For submission of Manuscript template and authors' instructions, please visit journal website at: ***https://mijst.mist.ac.bd/mijst/index.php/mijst/***

MIJST offers a faster peer-review process. There will be no charges for Registration, Online submission, Publication of manuscripts, and access to the published articles. Best selected papers will also be awarded by MIJST.

ABOUT MIJST

MIST International Journal of Science and Technology (MIJST), published biannually (June and December), is a peer-reviewed open-access journal of the Military Institute of Science and Technology (MIST). This journal is a continuation of the 'MIST Journal of Science and Technology', published by MIST, under ISSN 1999-2009 from 2009 to 2011, ISSN 2224-2007 from 2012 to 2019, & E-ISSN 2707-7365 since 2020.

MIJST publishes original research findings as regular papers, review papers (by invitation). The Journal provides a platform for Engineers, Researchers, Academicians, and Practitioners who are highly motivated in contributing to the Engineering, Science, and Technology and Applied Sciences disciplines. MIJST welcomes contributions that address solutions to the specific challenges of the developing world.

The Journal will be indexed under the "Bangladesh Journal Online", "Creative Common" and "Open Journal System" databases and will be accessible through Google Scholar. The journal is also planned to be registered under the Asian Citation Indexing, Directory of Open Access Journals (DOAJ), SCOPUS, and Emerging Source Citation Indexing (ESCI) in course of time. The Journal aims to be one of the leading journals of the Country and the Region for its contributions in the advancement of Science and Technology. Unpublished innovative world-class research papers under the following subject areas are invited. Contributions from other areas of Engineering and Applied Sciences are also welcome.

SUBJECT AREAS:

- **AEROSPACE AND AVIONICS ENGINEERING**
- **APPLIED PHYSICS & SCIENCE**
- **ARCHITECTURE**
- **BIOMEDICAL ENGINEERING**
- **CHEMISTRY**
- **CIVIL ENGINEERING**
- **COMPUTER SCIENCE AND ENGINEERING**
- **ELECTRICAL, ELECTRONIC AND COMMUNICATION ENGINEERING**
- **ENVIRONMENTAL, WATER RESOURCES, AND COASTAL ENGINEERING**
- **INDUSTRIAL AND PRODUCTION ENGINEERING**
- **MATERIALS SCIENCE & ENGINEERING**
- **MECHANICAL ENGINEERING**
- **NAVAL ARCHITECTURE AND MARINE ENGINEERING**
- **NUCLEAR SCIENCE & ENGINEERING**
- **PETROLEUM AND MINING ENGINEERING**

E-ISSN: 2707-7365